

ABSTRACT

Title of Dissertation: ABNORMAL GRAIN GROWTH IN
MAGNETOSTRICTIVE GALFENOL
ROLLED SHEET

Hyunsuk Chun, Doctor of Philosophy, 2011

Directed By: Professor Alison B. Flatau
Department of Aerospace Engineering and
Professor Manfred Wuttig
Department of Materials Science and
Engineering

Highly textured Fe-Ga (Galfenol) rolled sheet with Cube (100)<100> or Goss (110)<100> preferred orientation is under investigation to provide easy magnetization, enhanced magnetostrictive performance and a cost-effective option for production of these alloys for use in applications as sensors and actuators.

In this study, 1-2.5% NbC added Galfenol rolled sheet was used because NbC particles enhance the rollability of and abnormal grain growth (AGG) in polycrystalline Galfenol rolled sheet. Driving forces, due to grain boundary energy, surface energy, deformation energy and magnetic fields are generally considered to explain grain growth phenomena. In this dissertation, the effect on grain boundary energy for influencing AGG was studied for the case of high temperature annealing at 1200°C. Both Coincident Site Lattice (CSL) and High Energy Grain Boundary (HEGB) models were investigated as possible mechanisms to explain the contribution of grain boundary energy to Goss-textured AGG. Results support the HEGB model as a suitable model for the observed development of Goss-textured AGG in Galfenol rolled sheet. Next, the effect of deformation energy on AGG was studied by using tension annealing and strain

annealing methods in the temperature range of 900°C to 1100°C. This study was built on results from studies of grain boundary energy on other alloys. For the tension annealing investigation, Galfenol rolled sheet was simultaneously subjected to tensile loading during high temperature annealing. No AGG was observed from the tension annealing method. For the strain-annealing investigation, homogeneously recrystallized Galfenol rolled sheet with a taper was subjected to tensile loading under different strain rates and post-strain high temperature anneal conditions to investigate the resultant grain growth phenomena. Different grain growth modes, including Cube- and Goss-textured AGG, were observed in this study. Assessment of the extent of AGG resulting from these was conducted using Electron Backscattering Diffraction (EBSD) patterns that were captured and analyzed using Orientation Imaging Microscope (OIM) software to obtain Inverse Pole Figures (IPF) and Orientation Distribution Function (ODF). Additionally, Ga loss, which lowers the magnetostrictive properties, under different conditions was investigated by Electron Probe Micro Analyzer (EPMA). No significant Ga loss was observed during the annealing process at 1000°C, however, about 2% Ga loss was observed during the annealing process at 1100°C and 1200°C in the areas with a high density of grain boundaries.

ABNORMAL GRAIN GROWTH IN MAGNETOSTRICTIVE GALFENOL ROLLED SHEET

By

Hyunsuk Chun

Dissertation submitted to the Faculty of the Graduate School of the
University of Maryland, College Park, in partial fulfillment
Of the requirements for the degree of
Doctor of Philosophy
2011

Advisory Committee:

Professor Alison B. Flatau, Chair/Advisor

Professor Manfred Wuttig

Professor Ichiro Takeuchi

Professor Lourdes Salamanca-Riba

Professor Norman m. Wereley (Dean's Representative)

© Copyright by

Hyunsuk Chun

2011

Dedication

To my parents and Sarang

Acknowledgments

I would like to express my sincere gratitude to my advisor, Prof. Alison B. Flatau for giving me the opportunity to work on exciting Galfenol projects. I would especially like to thank her for her guidance and support throughout my Ph.D research at the university of Maryland. I benefited from her guidance in every aspect during my Ph.D study, including the discussions we held and intelligent suggestions she made regarding my research. I deeply appreciate all the time and effort she spent discussing my projects and advising me. I also appreciate all corrections to my papers and thesis, attentive consideration and encouragement she gave me. Most important of all, I would like to thank her for being such a nice human being and teaching me how to remain calm and keep a smile on my face no matter how difficult a situation I am in. It would not have been possible to accomplish my scientific goals without her guidance.

Also, I would like to express my very gratefulness to my co-advisor Prof. Manfred Wuttig, for his insightful guidance and encouragement throughout the discussion of my doctoral work. He always encouraged me to go forward to achieve my goal. I have great respect for his knowledge and passion for research.

I would like to thank Prof. Riba, Ichiro and Wereley for taking time out of their busy schedule to serve on my committee and evaluate my work. I would like to acknowledge the financial support of the US office of Naval Research through MURI grant #N000140610530.

I especially appreciate my parents and parents-in-law in Korea for their devotional care and support from a distance. Also, I appreciate my brother, Bumseok in Ohio and sister-in-law, Danbi in Korea. Finally, I want to thank my lovely wife, Sarang and my precious daughter, Hamin. I would never achieve anything without their dedicated love.

Thank God...

List of Tables

Table 1	List of common smart materials	1
Table 2	Driving forces for grain boundary migration	21
Table 3	Crystallography of slip in cubic metals	29
Table 4	Rotation axes and angles for coincident site lattices of $\Sigma<31$	38
Table 5	Details from OIM and GBCD of 1mol.% NbC added Galfenol rolled sheet samples A, B and C which were annealed for 2, 3, and 4 hours under Ar atmosphere, respectively	48
Table 6	Summary of samples for tension annealing.....	59
Table 7	Summary of samples for strain annealing.....	75
Table 8	Different grain growth mode at different Engineering strain	85

List of Figures

Figure 1	Schematic indicating solid state transformation of polycrystalline Fe-Ga alloy as an inexpensive alternative to single crystal growth of Fe-Ga alloy.....	3
Figure 2	Joule magnetostriction. (a) Changes in shape in response to the magnetic field H. (b) Relationship between H and $\lambda=\Delta L/L$	7
Figure 3	(a) Schematic of a strain gauge from reference 6 (b) photo of a strain gauge on a rolled sheet sample.....	8
Figure 4	Magnetostriction as a function of Ga content in single crystal Galfenol subjected to the different processing protocols indicated.....	10
Figure 5	Magnetization curves for the $\langle 100 \rangle$, $\langle 110 \rangle$ and $\langle 111 \rangle$ directions of an iron cubic single crystal	11
Figure 6	Schematic diagram of well aligned Goss and Cube textures in a polycrystalline rolled sheet.....	12
Figure 7	Schematic diagram of a typical annealing process (a) Deformed state; (b) Recovered meta-stable state; (c) Partially recrystallized; (d) Fully recrystallized; e) Grain growth; (f) Abnormal grain growth.....	13

Figure 8	Typical recrystallization kinetics during isothermal annealing.....	16
Figure 9	Schematic representation of the change in grain size distribution during (a) NGG and (b) AGG.....	24
Figure 10	Schematic diagrams explaining a theoretical model of SIBM. (a) Undeformed boundary state with different dislocation density ρ_1 and ρ_2 . (b) The stored energy difference between two adjacent deformed grains of high stored energy, E_1 , and low stored energy, E_2 forms the dragging of the dislocation structure behind the migrating boundary. (c) The migration boundary is free from the dislocation structure.....	26
Figure 11	(a) An optical micrograph showing SIBM in Al (Bellier and Doherty 1977), (b) TEM image of SIBM in Cu deformed 14% in tension and annealed 5 minutes at 234°C.....	27
Figure 12	A symmetrical tilt boundary.....	31
Figure 13	Energy of tilt boundary and the energy per dislocation as a function of the crystal misorientation.....	33
Figure 14	The measured (symbols) and calculated (Solid line) energy of low angle tilt boundaries as a function of misorientation, for different metals.....	34

Figure 15	The measured (symbols) and calculated (Dotted line) grain boundary energy as a function of misorientation. Theoretical curve has $A=0.231$	35
Figure 16	A coincident site lattice ($\Sigma 5$) formed from two simple cubic lattices rotated by 36.87° for an $\langle 001 \rangle$ axis.....	37
Figure 17	$\Sigma(3-9)$ CSL boundary distribution before and after Goss-textured AGG in Fe-3%Si alloy.....	41
Figure 18	The relative grain boundary energy as a function of misorientation angle for $\langle 100 \rangle$, $\langle 110 \rangle$ and $\langle 111 \rangle$ tilt boundaries in Fe-3% Si steel.	42
Figure 19	Magnetostriction of 1.0 mol.% NbC added Galfenol rolled sheet as a function of annealing time at 1200°C under Ar atmosphere.....	45
Figure 20	IPF image along normal direction of 1.0 mol.% NbC added Galfenol rolled sheet samples A, B, and C, which were annealed for 2, 3, and 4hours under Ar atmosphere, respectively.....	46
Figure 21	CSL boundary distribution of sample A, B and C, which were annealed for 2, 3, and 4hours under Ar atmosphere, respectively.....	49
Figure 22	CSL boundary distribution of sample A, B and C, which were annealed for 2, 3, and 4hours under Ar atmosphere, respectively. (without OIM clean up process).....	51
Figure 23	Different misorientation distribution around Goss-textured AGG (a) low grain boundary energy with low angle misorientation ($<20^\circ$), (b) high grain boundary	

	energy with middle angle misorientation ($20^\circ < \theta < 45^\circ$), and (c) low grain boundary energy with high angle misorientation ($>45^\circ$).....	52
Figure 24	Normalization of grain boundary misorientation angle distribution from each grain.....	53
Figure 25	Misorientation angle distribution around each (110), (111) and (100) grain (top to bottom) in Galfenol rolled sheet samples A, B and C (left to right) that annealed 2, 3 and 4 hours under Ar atmosphere, respectively.....	54
Figure 26	Schematic diagram for tension annealing system (a) Terfenol-D actuator for strain rate control, (b) titanium sample holder for high temperature annealing and (c) load cell for monitoring the stress variation.....	60
Figure 27	Monitoring the (a) strain rate and (b) stress variation of tension annealed Galfenol rolled sheet during tension annealing at 1000°C under Ar atmosphere.....	61
Figure 28	IPF and ODF plots of as-rolled Galfenol rolled sheet sample.....	62
Figure 29	IPF images of tension annealed Galfenol rolled sheet samples along normal direction and ODF plots at different conditions: (a) annealed at 1000°C for 3 hours with no tension, (b) annealed at 1000°C for 3 hours with tension and strain rate control ($2 \times 10^{-4}/\text{s}$), and (c) annealed at 1000°C without strain rate control but with a constant tensile load.....	63

Figure 30	Schematic representation of variation of final grain size with strain.....	67
Figure 31	IPF and ODF plot of pre-annealed Galfenol sample at 700°C for 10 hours.....	68
Figure 32	Experimental true stress & true strain curve and optical images of Galfenol rolled sheet samples: before (left) and after (right) tension at 300°C.....	70
Figure 33	IPF image of a Galfenol sample annealed at 1000°C for 1 hour after imposing a 5 x 10 ⁻⁴ /s displacement rate controlled tension force. Grain growth occurred near the pin hole region and the abnormally grown Goss grains were tilted about 7° along the rolling direction.....	71
Figure 34	Tapered dog-bone Galfenol sample with 5% tapering and 3.3 inch long.....	72
Figure 35	Overall experimental procedure of strain annealing process. step1) Initial tapered dog bone sample by cold rolling, step 2) Pre-annealing at 850°C for 15hr under Ar for stress release and homogeneous recrystallization, step3) Tension at 200°C and 500°C with different displacement rate control to obtain critical strain for grain growth, step4) Annealing at 900°C, 1000°C and 1100°C up to 3hr. under Ar to observe strain-induced grain growth.....	73
Figure 36	Photograph of MTS machine for tension which is designed to elevate tensioning temperature up to around 900°C.....	74
Figure 37	IPF and ODF plots of pre-annealed sample at 850°C for 15 hr. showing primary	

	recrystallization with a randomly oriented distribution. Average grain size is ~67 μm	76
Figure 38	The effect of the initial grain size on the value of the critical strain.....	77
Figure 39	Stress and strain curve of brittle (sample 1) and ductile (sample 4) fractured Galfenol rolled sheet samples at different conditions. Sample 1) tensioning at 200°C with 5x10 ⁻⁴ /s displacement rate, Sample 4) tensioning at 500°C with 1x10 ⁻⁴ /s displacement rate).....	79
Figure 40	Optical and partial IPF images of brittle fractures Galfenol rolled sheet samples (a) annealing at 1000°C for 3hours, and (b) annealing at 1050°C for 15 hours.....	80
Figure 41	IPF images of strain annealed ductile fractured Galfenol rolled sheet samples (a) annealing at 900°C for 3hours, (b) annealing at 1000°C for 3hours, and (c) annealing at 1100°C for 3hours under Ar atmosphere. (*P.R. : Primary Recrystallization).....	82
Figure 42	IPF images of different annealing time at 1000°C (a) as-tensioned Galfenol rolled sheet sample, (b) annealing for 15 minutes, (c) annealing for 30 minutes, and (d) annealing for 3 hours.....	86
Figure 43	High magnified IPF images of region B in Figure 42 and different area fraction of small island grains with the size of under 200 μm diameter. (a) area fraction of island grains is 26.28%, (b) area fraction of island grains is 8.61% and (c) area fraction of island grains is 2.79%.....	87
Figure 44	High magnified IPF images of as-tensioned Galfenol rolled sheet sample.	

	From region (a) to (g): grain size decreases gradually, (g-1): many sub-grain boundaries inside each grain.....	88
Figure 45	IPF images, ODF plots, and misorientation distribution at different regions of as-tensioned Galfenol rolled sheet sample.....	91
Figure 46	Schematic diagram on the effect of SIBM on different grain growth modes of regions B and C in Figure 42.....	92
Figure 47	Schematic diagram of nucleation through SIBM mechanism during tension test at 500°C	94
Figure 48	Summary of tapered strain annealed samples with (a) brittle and (b) ductile fracture modes. (a) Small fraction of NGG was occurred from the brittle fractured dog bone samples that annealed at 1000°C and 1050°C, (b) primary recrystallization was occurred from the ductile fractured sample that annealed at 900°C and tilted-Cube and Goss-textured AGG were occurred from ductile fractured samples that annealed at 1000°C and 1100°C, respectively.....	95
Figure 49	Deformation energy and strain effects for grain growth (a) Occurrence of primary recrystallization after annealing at 1000°C under Ar without tension, (b) Tilted cube-textured AGG and NGG after annealing at 1000°C under Ar with tension, and (c) Goss-textured AGG and NGG after annealing at 1100°C under Ar with tension.....	97
Figure 50	Optical images of as tensioned Galfenol rolled sheet sample with a constant displacement rate of 1×10^{-4} /s.....	99

Figure 51	IPF images of Galfenol rolled sheet sample that annealed at 1000°C for 1 hour. (a) 1.7% engineering strain and primary recrystallization, (b) 3.2% engineering Strain and NGG.....	100
Figure 52	Optical images of as tensioned Galfenol rolled sheet sample with a constant displacement rate of 1×10^{-5} /s showing dimensions before and after tensioning of the sample.....	100
Figure 53	IPF image of uniformed Galfenol rolled sheet sample with 2.7% engineering strain that annealed at 1000°C for 3 hours.....	101
Figure 54	EPMA point analysis on Ga losses from Galfenol rolled sheet samples as a function of annealing time for 2, 3 and 4 hours at 1200°C under Ar atmosphere.....	105
Figure 55	The rate of Ga loss in Galfenol rolled sheet samples as a function of annealing time at 1200°C under Ar atmosphere.....	106
Figure 56	Variation of Ga content in Galfenol rolled sheet samples depends on annealing time and temperature.....	107
Figure 57	Schematic diagram of a typical EBSD setup.....	111
Figure 58	(100) pole figures for sheet material (a) random orientation and (b) preferred orientation. R.D. (rolling direction) and T.D. (transverse direction) are reference directions in the plane of the sheet.....	113
Figure 59	An inverse pole figure for the cubic class where the crystal axes are fixed	114

Figure 60	Schematic of three dimensional graphical representations of projections of ODFs in Euler space.....	115
Figure 61	Schematic representation of the main texture component in the $\phi_2=45^\circ$ section of ODF in bcc metals.....	116

Table of Contents

Abstract	
List of Tables	
List of Figures	
Table of Contents	

Chapter 1.	Introduction.....	1
1.1	Motivation.....	1
1.2	Synopsis of dissertation chapters	4
Chapter 2.	Literature Review.....	6
2.1	Magnetostriction	
2.1.1	Basic Concept of Magnetostriction.....	6
2.1.2	Application.....	7
2.1.3	Measurement of Magnetostriction.....	8
2.2	Galfenol	
2.2.1	General Information.....	9
2.2.2	Magnetostriction in Galfenol.....	9
2.3	Metallurgical Factors affecting the Magnetic Properties	
2.3.1	Crystallographic Texture.....	11
2.3.2	Grain Boundary.....	12
2.4	The Annealing of a Deformed Material	
2.4.1	Primary Recrystallization	15
2.4.1.1	The Laws of Primary Recrystallization.....	16
2.4.1.2	Nucleation for Recrystallization.....	18
2.4.2	Dynamic Recrystallization.....	19
2.4.3	Grain Growth.....	19
2.4.3.1	Factors Influencing Grain Growth.....	19
2.4.3.2	Driving Forces for Boundary Migration.....	20
2.4.4	Abnormal Grain Growth (Secondary Recrystallization).....	23
2.4.5	The Effect of Deformation for Grain Growth.....	25
2.4.5.1	Strain Induced Boundary Migration (SIBM).....	25
2.5	Deformation Energy and Mobility	
2.5.1	Stored Energy.....	29
2.5.2	Microstructure of Deformed Metal.....	30
2.6	Geometrical Characterization for Grain Boundary Energy	

2.6.1 Low Angle Grain Boundaries (Misorientation).....	31
2.6.2 High Angle Grain Boundaries (Coincident Site Lattice (CSL)).....	36
Chapter 3. Grain Boundary Energy for Goss-textured AGG in Galfenol Rolled-Sheet	
3.1 Introduction.....	39
3.2 Two candidate models for Goss-textured AGG	
3.2.1 The Role of Coincident Site Lattice (CSL)	
for Goss-Textured AGG in Fe-Si.....	40
3.2.2 The Role of High Energy Grain Boundary (HEGB)	
for Goss-Textured AGG in Fe-Si.....	42
3.3 Detailed Experimental Procedure.....	43
3.4 Results	
3.4.1 Magnetostriction vs Texture Variation.....	45
3.4.2 The Role of CSL Boundaries in Galfenol Rolled Sheet.....	49
3.4.3 The Role of Misorientation in Galfenol.....	52
3.5 Conclusion.....	56
Chapter 4. Deformation Energy Effect on AGG I	
- By Tension Annealing -	
4.1 Introduction.....	57
4.2 Experimental Procedure.....	58
4.3 Results and Discussion.....	61
4.4 Conclusion.....	65
Chapter 5. Deformation Energy Effect on AGG II	
- By Strain Annealing -	
5.1 Introduction.....	66
5.2 Strain Annealing with Preliminary Samples	
5.2.1 Experimental Procedure.....	67
5.2.2 Results.....	69
5.3 Strain Annealing with Tapered Sample	
5.3.1 Sample Preparation and Experimental Procedure.....	72
5.3.2 Results	
5.3.2.1 Pre-annealed Sample before Tension.....	76

5.3.2.2 Tension at Different Conditions.....	78
5.3.2.3 Texture Analysis.....	80
5.3.2.3.1 Brittle Fractured Sample.....	80
5.3.2.3.2 Ductile Fractured Sample.....	81
5.3.3 Mechanism for AGG by Strain Annealing with Tapered Samples.....	92
5.3.4 Summary on Tapered Strain Annealed Samples with Brittle and Ductile Fracture Mode.....	95
5.4 Strain Annealing with Uniform Sample.....	98
5.5 Conclusion.....	101
Chapter 6. Ga loss during High Temperature Annealing Process	
6.1 Introduction.....	103
6.2 Result	
6.2.1 Ga loss during High Temperature Annealing at 1200°C.....	103
6.2.2 Ga loss during Strain Annealing at 1000°C & 1100°C.....	106
6.3 Conclusion.....	107
Chapter 7. Summary and Future Work.....	108
Appendix A Characterization Technology	
- Electron Back Scatter Diffraction (EBSD) -	
A-1 Overview.....	110
A-2 Formation of Diffraction Patterns.....	112
A-3 Texture Analysis.....	112
Bibliography.....	117

Chapter 1. Introduction

1.1 Motivation

There are various smart materials for similar application such as actuator and/or sensor. Each material has different driving force to change its shape and they show different mechanical properties. Table 1 shows a list of common smart materials with their free strain, modulus, tensile strength and actuation requirement.¹⁻³

Table 1. List of common smart materials
(Table from reference 1-3)

Material Type	Free Strain (ppm)	Modulus (GPa)	Tensile Strength (MPa)	Actuation requirement	Linearity
Piezoelectric – PZT-5H	1000	~68	27.6 (Brittle)	5 kV/cm (Electric Field)	First-order linear (small hysteresis)
SMA - Nitinol	60,000	~20 (martinsite) ~50 (austenite)	High (Ductile)	Heating through ~60° C	Highly non-linear (large hysteresis)
Magnetostrictive - Terfenol-D	1600-2400	25-35	28 (Brittle)	~1000 Oe (Magnetic Field)	Non-linear (moderate hysteresis)
Magnetostrictive - Single Crystal Galfenol	300-400	~60	500 (Ductile-like)	~100 Oe (Magnetic Field)	Non-linear (low hysteresis)

The driving force to change the shape of Piezoelectric materials, like PZT, is electric field and it shows about 1000ppm free strain. Its modulus is about 68GPa and a tensile strength is nearly 28MPa. This material has been used for actuator with different shape. However, due to its low tensile strength it has some restriction under vibration atmosphere. Another smart material in this

table is Shape Memory Alloy (SMA) such as Nitinol. Its driving force is thermal energy and it shows significantly higher free strain than other smart materials as 60,000ppm. It has been used for military, medical, safety, and robotics applications with its very high free strain. However, there are still some difficulties that must be overcome before they can live up to their full potential. These alloys are still relatively expensive to manufacture and machine compared to other materials such as steel and aluminum. Most SMAs have poor fatigue properties; this means that while under the same loading conditions (i.e. twisting, bending, compressing) a steel component may survive for more than one hundred times more cycles than an SMA element. Magnetostrictive material like Terfenol-D or single crystal Galfenol is another type of smart material. These materials work due to magnetic field. As shown in this table 1, the free strain of Terfenol-D is almost 6 times higher than the one of single crystal Galfenol. However, in this study, single crystal Galfenol was focused upon due to its better mechanical properties. Unlike Terfenol-D, Galfenol is tough (500MPa tensile strength), thus it can be machined and used in devices in which Terfenol-D may fracture.

Single crystal Galfenol with Cube texture (100)<001> or Goss texture (110)<001> exhibits magnetostriction on the order of 400ppm or 300ppm at low applied magnetic field (100Oe), respectively as shown in Table 1. Making single crystal Galfenol with a traditional crystal growth method is expensive for industrial application. On the other hand, making polycrystal Galfenol is relatively inexpensive, however, it shows much lower magnetostrictive performance than the one of single crystal Galfenol. In 2009, Na published on the abnormal grain growth with Goss texture and magnetostriction in recrystallized Galfenol. The results in that publication present that Goss-textured abnormal grain growth (AGG) grew to several millimeter, and an increase of magnetostriction of from 28 to 163ppm after annealing at

1200°C.⁴ ETREMA Products, Inc. develops and manufactures magnetostrictive materials such as Terfenol-D and Galfenol, but much of their work involves growth of polycrystalline material. They are also investigating methods for rolling Galfenol and achieving highly textured material. Researchers from ETREMA served on the advisory board for the research program that supported this research.

Thus motivated by these results on AGG of Goss texture, the understanding and making a single crystal-like Galfenol rolled sheet through AGG phenomena using an inexpensive method caused by solid state transformation of polycrystalline Galfenol rolled sheet was studied in this dissertation. The schematic diagram shown in Figure 1 illustrates the alternative path to Galfenol single crystal growth to be studied.

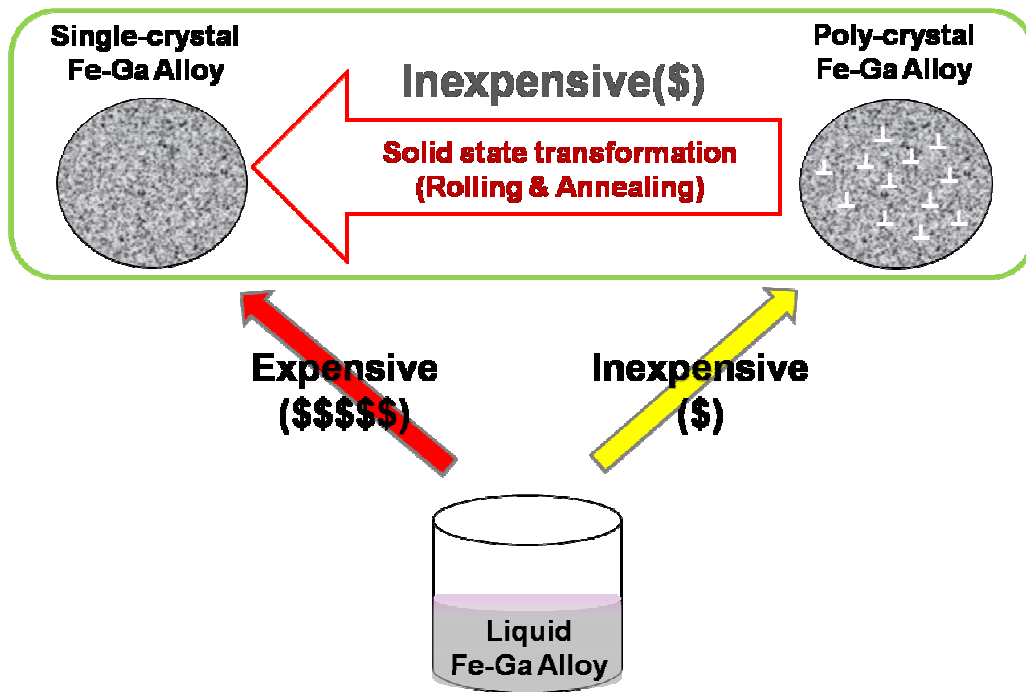


Figure 1 Schematic indicating solid state transformation of polycrystalline Fe-Ga alloy as an inexpensive alternative to single crystal growth of Fe-Ga alloy.

1.2 Synopsis of Dissertation Chapters

Chapter 2

This chapter provides an overview of magnetostriction, Galfenol, metallurgical factors affecting the magnetic properties of materials, various phenomena result from high temperature annealing with a deformed material, stored energy for grain boundary mobility, and the geometrical characterization for grain boundary energy.

Chapter 3

The geometrical characterization of grain size and orientation as it relates to the role of misorientation angle and coincident site lattice (CSL) boundaries in promoting AGG in Galfenol rolled sheet will be explained. The high percentage of high energy, middle angle misorientation ($20^\circ - 45^\circ$) boundaries around abnormally grown Goss grains supports the high energy grain boundary (HEGB) model for Goss-textured AGG in 1.0% NbC added Galfenol rolled sheet.

Chapter 4

The tension annealing method will be described to investigate the use of tension to promote dynamic recrystallization for AGG in 1.0% NbC added Galfenol rolled sheet as an approach for altering grain boundary energy that will be described in chapter 3. Tension annealing produces an increase in the area fraction of cube texture and $\{111\}$ grains relative to what was observed with no tension annealing, however, no dynamic recrystallization (DRX) with AGG is observed from this process.

Chapter 5

The strain annealing method will be described to identify the deformation energy and strain effects as alternative approach to tension annealing for introducing on AGG in 1.0% NbC added Galfenol rolled sheet. Tapered dog bone samples will be used for this study to investigate the different strain and deformation effect from one sample. Tilted Cube- and Goss-textured strain-induced AGG was observed in ductile fractured samples that were tensioned at 500°C with 1×10^{-4} /s displacement rate.

Chapter 6

The Ga loss through the grain boundaries during high temperature annealing process will be investigated. For a 4-hour long, high temperature anneal at 1200°C and an initial composition of 18.7% Ga, rate of Ga loss varied with density of grain boundaries. Strain anneal at 1000°C did not exhibit Ga loss, while anneals at 1100°C and above exhibited Ga loss at rates that depended on density of grain boundaries and temperature.

Thus, various effects including particle (NbC) effect, grain boundary energy effect, deformation energy effect and strain effect on AGG in Galfenol rolled sheet will be illustrated in this dissertation. Also, this dissertation will suggest the possibility to decrease the annealing temperature and form Goss and Cube-textured AGG by controlling the driving forces for grain growth.

Chapter 2: Literature Review

2.1 Magnetostriction

2.1.1 Basic Concept of Magnetostriction

Magnetostriction, λ , is defined as the phenomenon in which a magnetic body shrinks or expands in the direction of the magnetization as a function of the magnitude an applied magnetic field. Nearly all ferromagnetic materials exhibit some measurable magnetostriction. Magnetostriction, λ , is the % strain, $\lambda = \Delta L/L$, where L is the initial length of the material in its un-magnetized state, and ΔL is the resultant strain as change in length under magnetization (H), along a given direction. Examples of common magnetostrictive ferromagnetic materials are Fe, Ni and Co, which have maximum magnetostrictive strain on the order of 10×10^{-6} .⁵ Additionally, Terfenol-D ($Tb_{0.3}Dy_{0.7}Fe_2$) has been developed which generates giant magnetostrictive strain on the order of 1000×10^{-6} .⁶ Figure 2(a) illustrates that along with an increase in length in the direction of the field, there is also a decrease in length in the perpendicular directions, and as a result of this, the total volume of the rod remains nearly constant. When an external magnetic field is applied, the domains which are aligned most closely with the external field will grow while all other domains will be reduced in size. Depending on the orientation of the crystal, there will be some cases where electron orbitals cannot become aligned with the direction of the external magnetic field without an increase in distance between the atoms or ions. These changes in distance may cause the crystal structure to become elongated in the same direction as the magnetic field. Figure 2(b) shows two important properties of magnetostriction. First, for high values of H , λ eventually reaches a constant value λ_{sat} , indicating saturation; secondly the

magnetostriction λ changes with the magnitude of H and that the response to positive and negative values of H of a given magnitude are the same.^{7,8,9,10,11}

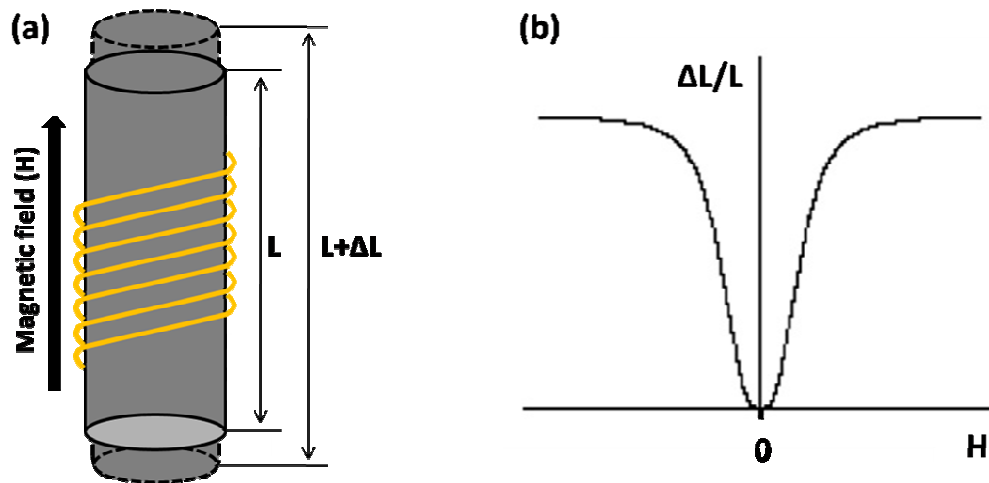


Figure 2 Joule magnetostriction. (a) Changes in shape in response to the magnetic field H .
(b) Relationship between H and $\lambda = \Delta L/L$.

2.1.2 Application

In general, magnetostrictive materials are used in actuation and sensing applications in variety of mechanical circumstances. The main applications in actuation are sonar transducers,^{12,13,14,15} linear motors,^{16,17} and rotational motors.^{18,19,20} Also, the most common applications in sensors are torque sensors,^{21,22} and force sensors.⁷

2.1.3 Measurement of Magnetostriction

For crystalline materials, use of a strain gauge is the most common method to measure magnetostriction. The advantage of this method is that it can be used over a wide temperature range and is less expensive than other methods, although they are not suitable for wires or thin films.²³ A schematic of a typical strain gauge is illustrated in Figure 3(a) and an actual attached strain gauge image is shown in Figure 3(b). It consists of a thin film with a wire attached to it, which meanders over an area of film. The electrical resistance of the wire alters in proportion to the amount of strain it experiences. As the gauge is strained, its resistance increases. However, the variation in resistance is very small, thus a Wheatstone bridge²⁴ is necessary to achieve a useful signal to noise ratio. This method is convenient for studying large or moderate magnetostriction above 10^{-6} .

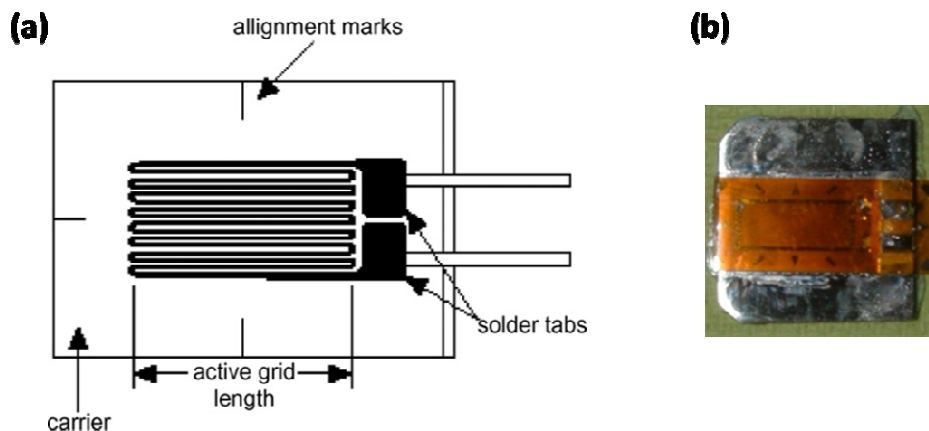


Figure 3(a) Schematic of a strain gauge from reference 6 (b) photo of a strain gauge on a rolled sheet sample.

2.2 Galfenol

2.2.1 General Information

In materials science, Galfenol is the general term for an alloy of iron and gallium. The name was first given to iron-gallium alloys by United States Navy researchers in 1998 when they discovered that adding gallium to iron could amplify iron's magnetostrictive effect up to tenfold.²⁵ Over the past decades, Fe-Ga alloys have attracted considerable interest due to their large saturation magnetostrictive potential (400ppm) in low applied magnetic fields (100Oe), very low hysteresis, while demonstrating high tensile strength (500MPa), and limited dependence of magneto mechanical properties on temperatures between -20°C and 80°C.^{26,27,28} Furthermore, the ability of this alloy to withstand shock loads and harsh operating environments and to operate in tension is likely to extensively expand the design space for use of magnetostrictive materials in the field of smart structures.

2.2.2 Magnetostriction in Galfenol

Clark et al. investigated the effect of Ga addition in single crystal iron and found an increase of magnetostriction (λ_{100}).²⁹ Figure 4 illustrates magnetostriction as a function of Ga content in single crystal Galfenol.³⁰ These data were obtained by measuring the saturation magnetostriction of single crystal Galfenol samples that had been exposed to homogenizing thermal treatments followed by exposure to various cooling conditions, i.e. furnace cooled or water quenched. One data point for magnetostriction of a directionally solidified Galfenol

sample without annealing is also shown. As shown in Figure 4, a maximum magnetostriction of 400ppm occurred from a water quenched sample that had a composition of 19% Ga.

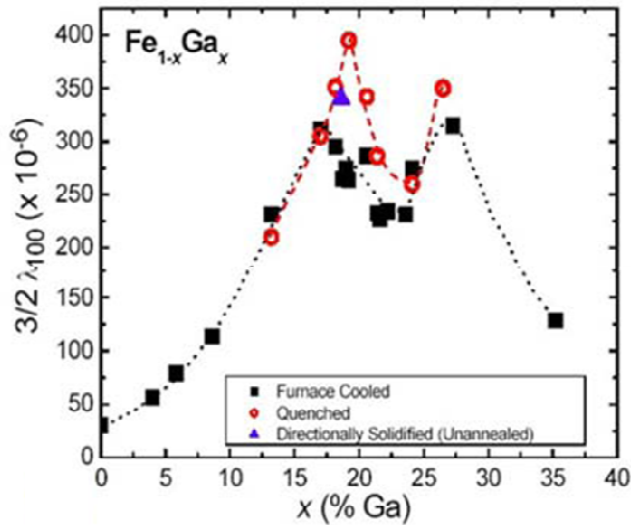


Figure 4 Magnetostriction as a function of Ga content in single crystal Galfenol subjected to the different processing protocols indicated. (image from clark et al. (30))

Studies on structural transformations in Galfenol were explored by Lograsso et al. specifically focusing on single crystal 19at% Ga samples that were subjected to various thermal treatments and then analyzed using powder X-ray diffraction.³¹ They confirmed that the formation of DO₃ and/or B2 phase can be prevented by rapid cooling. Many extensive studies on the effect of thermal history and Ga composition have shown that Galfenol with DO₃ phase has a long range ordering of Ga atoms which lowers the magnetostriction.^{32,33,34,35} Based on these backgrounds, 19at% Galfenol was used in this study and all the samples were water quenched to prevent the formation of DO₃ and/or B2 phase.

2.3 Metallurgical Factors affecting the Magnetic Properties

2.3.1 Crystallographic Texture

The magnetic properties are dependent on crystallographic orientation. In bcc iron (cubic structure), the easy magnetic direction, i.e. the direction along which the magnetization process occurs most readily, is the $\langle 100 \rangle$ direction. The saturation magnetization value M_s is the same for all directions of magnetization, but to reach saturation along different directions requires different levels of applied field H . A low H is required in the $\langle 100 \rangle$ direction, which is sketched from Honda and Kaya in reference 36 to illustrate this phenomena as shown in Figure 5.

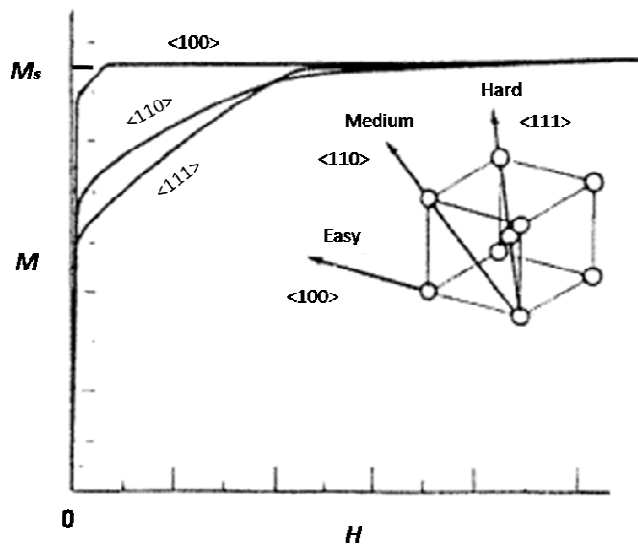


Figure 5 Magnetization curves for the $\langle 100 \rangle$, $\langle 110 \rangle$ and $\langle 111 \rangle$ directions of an iron cubic single crystal. (image from Honda and Kaya (36))

It is also reported that the $\langle 001 \rangle$ is the easiest direction for high magnetostriction in cubic crystal.³⁷ As rolled polycrystalline material exhibits many grains with random crystallographic orientation along the rolling direction. Texturing to develop a preferential

crystallographic orientation has long been used to maximize the magnetic properties in metals. The development of a “Cube texture” $\{100\}\langle 001\rangle$ or “Goss texture” $\{110\}\langle 001\rangle$ along the rolling direction is needed to maximize the magnetostrictive properties in polycrystalline Galfenol. These two textures are of interest because they have two and one in-plane $\langle 001\rangle$ axis respectively which will promote easy magnetization and large saturation magnetostriction. Figure 6 shows the in-plane $\langle 001\rangle$ axis from well aligned Goss- and Cube textures in a polycrystalline rolled sheet.³⁸

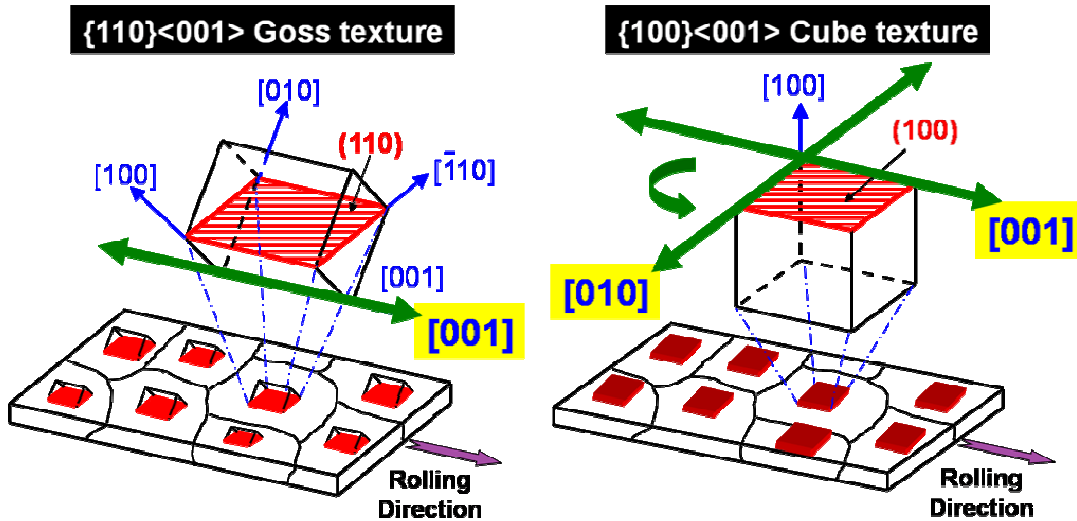


Figure 6 Schematic diagram of well aligned Goss and Cube textures in a polycrystalline rolled sheet. (images from Na and Flatau (38))

2.3.2 Grain Boundary

Grain boundaries act as pinning sites that impede magnetic domain wall motion,^{39,40} and are a source of energy losses in changing magnetic fields; however, they also increase the mechanical properties of material.⁴¹ Controlling density of grain boundary is important for design of materials with superior magnetic performance and excellent mechanical properties.

2.4 The Annealing of a Deformed Material

High temperature annealing processes are used for texturing polycrystalline rolled sheet samples.^{42,43} Figure 7 shows a schematic diagram from Humphreys and Hetherly (42) of a typical annealing process.

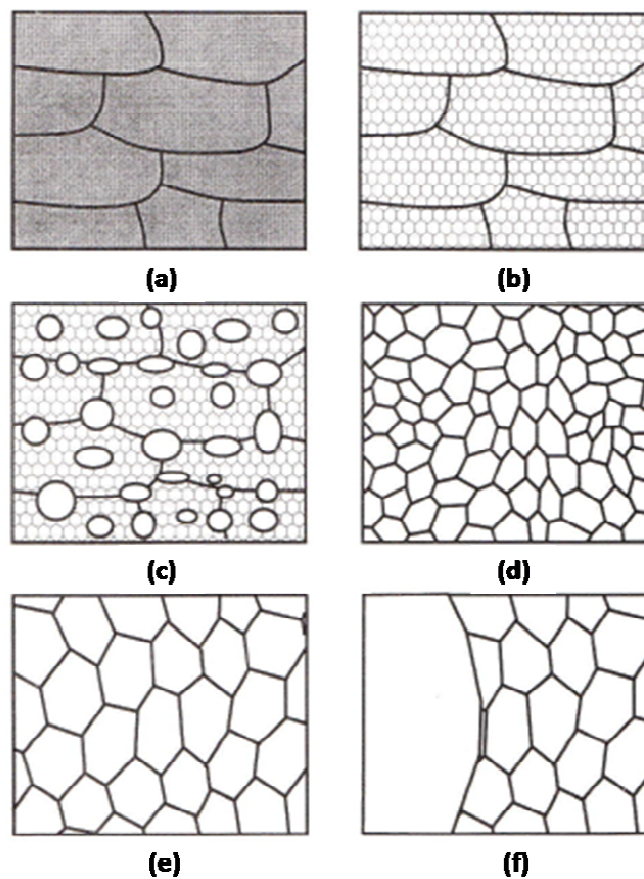


Figure 7 Schematic diagram of a typical annealing process (a) Deformed state; (b) Recovered meta-stable state; (c) Partially recrystallized; (d) Fully recrystallized; (e) Grain growth; (f) Abnormal grain growth. (image from Humphreys and Hatherly (42))

During deformation, the free energy in a sample increases and is stored in dislocations and interfaces. A metal containing these defects is thermodynamically unstable. Although it is suggested that the defects should spontaneously disappear, in practice the necessary atomic mechanisms are often very slow at low homologous temperatures, with the result that unstable defect structures are retained after deformation as shown in Figure 7(a). If the material is subsequently heated to a high temperature, the defect structure is transformed through thermally activated processes such as solid state diffusion which provide mechanisms whereby the defects may be removed or alternatively arranged in configurations of lower energy. By annealing a cold worked metal at an elevated temperature, the microstructure and the properties may be partially restored to their original values by “recovery” in which annihilation and rearrangement of the dislocation occurs.⁴⁴ The microstructural changes during recovery are relatively homogeneous and do not affect the boundaries between deformed grains, as shown in Figure 7(b). Recovery is a meta-stable state, because the removal of dislocation structure is only partial. At an elevated temperature, further restoration with dislocation-free grains occurs at a deformed and/or recovered structure. This process is called “(primary) recrystallization”. This process consists of the nucleation and production of new grains, possessing lower density of dislocations and thermodynamically lower energy than in the recovery state.^{45,46} These new grains then grow and consume the old grains with thermodynamically high energy. Figure 7(c) shows nucleation and a partially recrystallized state. A fully recrystallized state is shown in Figure 7(d). Though this process removes many dislocations, the material still contains grain boundaries, which are thermodynamically unstable. Further annealing may result in “grain growth”, in which the grain size increases. If this process changes the grain size homogeneously, this is called “normal grain growth” (Figure 7(e)). In certain circumstances this may give way to the selective grain growth

and this process is known as “abnormal grain growth” (AGG) or “secondary recrystallization” (Figure 7(f)). Some annealing processes, such as recovery and normal grain growth occur homogeneously, whereas others such as recrystallization and AGG are very heterogeneous.

2.4.1 Primary Recrystallization

The thermodynamically unstable defect structure created by cold rolling is eliminated by nucleation and grain growth during high temperature annealing. This phenomenon is called primary recrystallization in order to distinguish it from the process of exaggerated grain growth which may occur in fully recrystallized material. It is convenient to divide primary recrystallization into two regimes—nucleation, which corresponds to the initial occurrence of new grains in the microstructure, and growth, during which the new grains form in the deformed material. The progress of recrystallization with time during isothermal annealing is commonly represented by a plot of the volume fraction of material recrystallized as a function of the log of time. This plot takes on the characteristic sigmoidal form shown in Figure 8, and usually includes an apparent incubation time before recrystallization occurs. This is followed by an increasing rate of recrystallization, a linear region, and finally a decreasing rate of recrystallization mainly due to the impingement of growing grains upon one another.

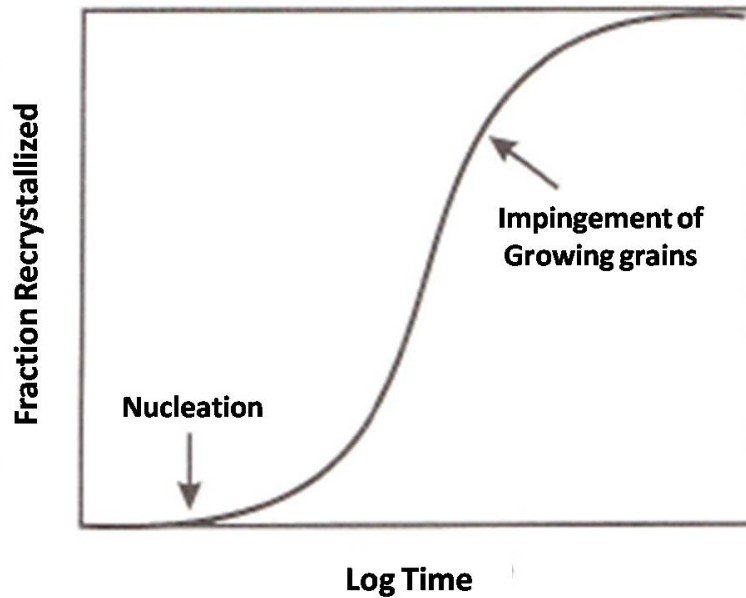


Figure 8 Typical recrystallization kinetics during isothermal annealing.

(image from Humphreys and Hatherly (42))

2.4.1.1 The Laws of Primary Recrystallization

The laws of primary recrystallization are obeyed in most cases and are easily rationalized if recrystallization is considered to be a nucleation and growth phenomenon, controlled by thermally activated processes, for which the driving force is provided by the stored deformation energy.^{42,47,48} These laws are summarized as follows:

- A minimum deformation is needed to initiate recrystallization.

Sufficient deformation is necessary to produce a nucleus for grain recrystallization and to provide the necessary driving force to sustain its growth.

- The temperature at which recrystallization occurs decreases as strain-induced stored energy increases.

The microscopic mechanisms controlling recrystallization are thermally activated and the relationship between the recrystallization rate and the temperature is given by the Arrhenius equation.

- The temperature at which recrystallization occurs decreases as strain increases.

The stored energy, which provides the driving force for recrystallization, increases with strain. As a result in highly deformed material, both nucleation and grain growth are more rapid or occur at lower temperatures.

- The recrystallized grain size depends primarily on the amount of deformation, being smaller for large amounts of deformation.

A higher strain will provide more nucleation sites per unit volume and thus a smaller final grain size will be obtained in highly deformed regions during the annealing process.

- For a given amount of deformation the recrystallization temperature will be increased by a larger starting grain size.

Grain boundaries are a favored site for nucleation. Because the density of grain boundaries decreases with increasing grain size, a large initial grain size provides fewer nucleation sites, causing a reduction in the nucleation rate and in the rate of recrystallization decreases.

2.4.1.2 Nucleation for Recrystallization

The nucleation for recrystallization is a critical factor in determining both the size and orientation of recrystallized grains. Thus, there has been a significant amount of work aimed at understanding how recrystallization nucleates. Burgers⁴⁹ first speculated that recrystallization probably nucleates at preexisting crystallites in the deformed material. Burke and Turnbull (1952)⁵⁰ considered nucleation as a random atomic fluctuation leading to the formation of a small crystallite with a high angle grain boundary. Such a nucleus would be stable if the difference in energy between the local deformed state and the recrystallized state were larger than the energy of the interface produced in forming the nucleus. The nucleation of recrystallization in this scenario can be considered to be discontinuous subgrain growth at sites of high strain energy and orientation gradient. The nucleation sites are also important in determining grain viability. Grain boundaries, transition bands and shear bands are three representative nucleation sites.⁴² A transition band separates parts of a grain which have split during deformation into regions of different orientation,⁵¹ regions of large orientation gradient, and an ideal sites for recrystallization. Recrystallization at transition bands was first reported by Hu in iron.⁵² Shear bands are thin regions of highly strained material typically oriented at $\sim 35^\circ$ to the rolling plane. They arise as a result of strain heterogeneity due to instability during rolling, and their formation is strongly dependent on the deformation conditions as well as the composition.⁵³

2.4.2 Dynamic Recrystallization

In dynamic recrystallization, as opposed to static recrystallization, the nucleation and growth of new grains occurs during deformation rather than afterwards as part of a separate heat treatment. Dynamic recrystallization may take place when a critical deformation condition is reached.⁵⁴ New grains originate at the existing grain boundaries; however, as the material continues to deform, the dislocation density of the new grains increases, thus reducing the driving force for their further growth, and the recrystallizing grains eventually cease to grow. An additional factor which may limit the growth of the new grains is the nucleation of further grains at the migrating boundaries.^{42,55} In chapter 4, tension annealing method for AGG is explained based on this dynamic recrystallization phenomenon.

2.4.3 Grain Growth

2.4.3.1 Factors Influencing Grain Growth

“Temperature” is significant factor for grain growth. Grain growth involves the migration of high energy grain boundaries and the kinetics of grain growth will therefore be strongly influenced by the temperature dependence of grain boundary mobility. As the driving force for grain growth is usually very small, significant grain growth is often observed only at very high temperatures.

Another factor influencing the grain growth is “specimen thickness”.⁵⁶ The rate of grain growth decreases when the grain size becomes greater than the thickness of a sheet of sample. In

this situation the grains are curved only in one direction rather than two, and therefore, the driving force for grain growth is diminished. In addition, where grain boundaries intersect the surface, grooves due to thermal etching, may develop that will also impede grain growth.

“Grain boundary pinning” by solutes⁵⁷ and by second phase particles⁵⁸ disrupts the influence of temperature and thickness effects on the development of normal and abnormal grain growth. Finally, a strongly textured material inevitably contains many low angle boundaries, and there is thus a reduced driving force for grain growth.

2.4.3.2 Driving Forces for Boundary Migration

Common sources of boundary migration driving force are shown in Table 2. The driving force for grain boundary migration P has the dimensions of energy per unit volume, which is conceptually equivalent to a pressure – a force acting per unit area on a grain boundary. In general, a driving force for grain boundary migration occurs if the boundary displacement leads to a decrease of the total free energy of the system. In principle, a gradient of any intensive thermodynamic variable offers a source of such a driving force: a gradient of temperature, pressure, density of defects, density of energy, contents of impurity, a magnetic field strength and so on. However, not all theoretically possible driving forces can be realized in practice.⁵⁹

Table 2 Driving forces for grain boundary migration

(Table from Gottstein and Shvindlerman (59))

Source	Equation	Approximate value of parameters	Estimated driving force in MPa
Stored deformation energy	$P = \frac{1}{2} \rho \mu b^2$	ρ = dislocation density ($10^{15}/m^2$) $\mu b^2/2$ = dislocation energy ($10^{-8}J/m$)	10
Grain boundary energy	$P = \frac{2\sigma_b}{R}$	σ_b = grain boundary energy ($0.5J/m^2$) R = grain boundary radius of curvature ($10^{-4}m$)	10^{-2}
Surface energy	$P = \frac{2\Delta\sigma^s}{d}$	d = sample thickness ($10^{-3}m$) $\Delta\sigma^s$ = surface energy difference of two neighboring grains ($0.1 J/m^2$)	$2 \cdot 10^{-4}$
Chemical driving force	$P = R(T_i - T_0)C_0 \ln C_0$	C_0 =concentration = max. solubility at T_0 $T_i(<T_0)$ annealing temperature (5% Ag in Cu at 300°C)	$6 \cdot 10^2$
Magnetic field	$P = \frac{\mu_0 H^2 \Delta\chi}{2} (\cos^2 \Theta_1 - \cos^2 \Theta_2)$	H = magnetic field strength (107A/m) $\Delta\chi$ = difference of magnetic susceptibilities ($1.8 \cdot 10^{-7}(250^\circ C)$) Θ = angle between c-axis and field direction ($\Theta_1=0^\circ$; $\Theta_2=90^\circ$)	$3.5 \cdot 10^{-4}$
Elastic energy	$P = \frac{\tau^2}{2} \left(\frac{1}{E_1} - \frac{1}{E_2} \right)$	τ = elastic stress (10MPa) E_1, E_2 = elastic moduli of neighboring grains ($10^5 MPa$)	$2.5 \cdot 10^{-4}$
Temperature gradient	$P = \frac{\Delta S \cdot 2\lambda grad T}{\Omega_a}$	ΔS = entropy difference between grain boundary and crystal (approx. equivalent to melting entropy) $\sim 8 \cdot 10^3 J/K \cdot mol$ $grad T$ = temperature gradient $\sim 10^4 K/m$ 2λ = grain boundary thickness $\sim 5 \cdot 10^{-10} m$ Ω_a = Molar volume $\sim 10 cm^3/mol$	$4 \cdot 10^{-5}$

The origin of driving forces and their approximate magnitudes are listed in Table 2 that is presented by Gottstein and Shvindlerman in reference 59. An excess in the density of defects (e.g. dislocation) in one of the adjoining grains is a powerful source of a driving force. There are several advantages to this type of driving force. For deformation energy, advantages include: ease of fabrication, excellent reproducibility, variation of the magnitude of driving force within a wide range up to a very large force. The energy of low angle grain boundaries are proved as a driving force for boundary migration by Aust, K.T. and Rutter, J.W.^{60,61,62} They investigated the striation substructure that provided the driving force for grain boundary migration, since migration of a grain boundary frees the crystal from the striations. The anisotropy of the surface tension of the free surfaces of a bicrystal represents a source for driving grain boundary migration.⁵⁹ It is known that the optimal value of P in this case is about 10^{-4} MPa. The anisotropy of any physical properties, e.g. the elastic constants or the magnetic susceptibility, can be utilized as a source of driving force for grain boundary migration. The origin of the driving force for boundary migration in a magnetically anisotropic material was considered by Mullins.⁶³ Another major driving force is a temperature gradient. In this case the optimal value of P is about 10^{-5} MPa.⁵⁹

Among many possible driving forces, grain boundary energy and deformation (strain) energy were the focus of this study.

2.4.4 Abnormal Grain Growth **(Secondary Recrystallization)**

Grain growth in concerned, it can be divided into two major types, normal grain growth (NGG) and abnormal grain growth (AGG). AGG (secondary recrystallization) takes place in order to reduce the interfacial regions and thus the overall energy of the system. This phenomenon takes place when the already recrystallized metal is further annealed at high temperatures and is often associated with the presence of precipitates.

During NGG, the microstructure changes in a rather uniform way, with a relatively narrow range of grain sizes and shapes. The schematic representation in Figure 9(a) that is from Humphreys and Hatherly (42) shows the nearly unaltered shape change but the average grain size slightly shifts towards the higher values.

In case of secondary recrystallization (AGG), a few grains in the microstructure grow and consume the matrix of smaller grains and a bimodal grain size distribution develops. However, eventually these large grains impinge on one another and normal grain growth may then resume as shown in Figure 9(b).⁴²

As was the case for NGG, the reduction of grain boundary energy is the main driving force for abnormal grain growth. AGG is not expected to occur where there are no impurities and grain boundary energy is constant. Under ideal conditions, a very large grain will always grow more slowly than the grains of average size and they will eventually rejoin the normal size distribution.^{64,65} Thus AGG cannot occur under conditions that are ideal for NGG.

The abnormally growing grain has some advantage over its neighbors and as a result a secondary recrystallized texture is developed. There are several candidate factors that influence AGG such as second phase particles,⁶⁶ texture and the effect of surface energy^{67,68}.

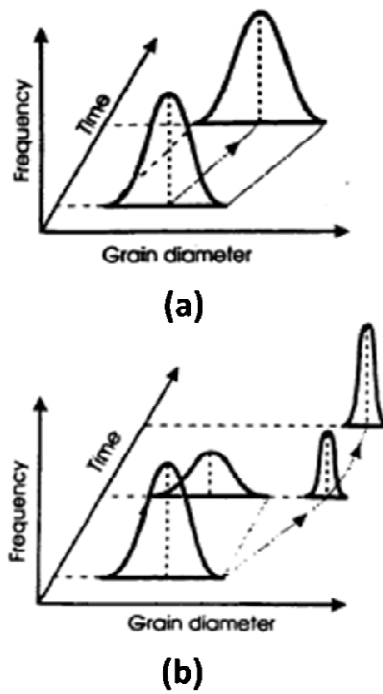


Figure 9 Schematic representation of the change in grain size distribution during (a) NGG and (b) AGG. (images from Humphreys and Hatherly (42))

2.4.5 The Effect of Deformation for Grain Growth

It has long been known that a small prior plastic strain may prevent normal grain growth and promote the onset of anomalous grain growth. This is classified as occurring due to primary recrystallization due to strain induced boundary migration (SIBM) rather than as a grain growth phenomenon.^{69,70}

2.4.5.1 Strain Induced Boundary Migration (SIBM)

Strain Induced Boundary Migration (SIBM) was first reported by Beck and Sperry (1950)⁷¹ and has been observed in variety of metals by other researchers. They found that this mechanism is particularly important after low strains. Subsequently, Bellier and Doherty⁷² confirmed that SIBM was the dominant recrystallization mechanism for reductions by compression of less than 20% in rolled Al. The driving force for SIBM is presumed to arise from a difference in dislocation density on opposite sides of the grain boundary. However, the origin of the differential dislocation density required for the operation of this mechanism is not entirely clear. The SIBM mechanism is explained by Humphreys and Hatherly⁴² for a simple bi-crystal case as shown in Figure 10.

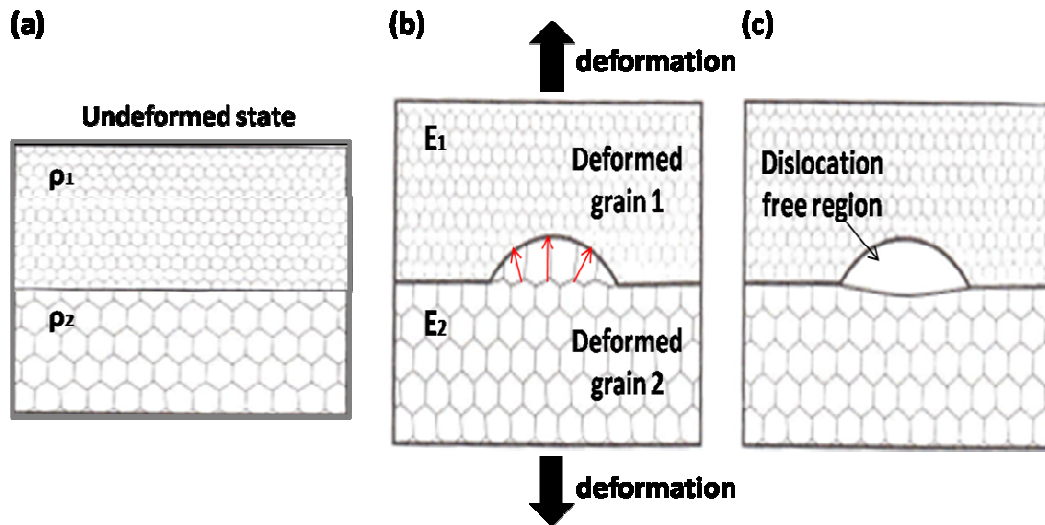


Figure 10 Schematic diagrams explaining a theoretical model of SIBM. (a) Undeformed boundary state with different dislocation densities ρ_1 and ρ_2 that are composed of grains of high stored energy, E_1 , and low stored energy, E_2 , respectively. (b) Strain-induced deformation moves grains 1 and 2 in opposite directions and the dragging of the dislocation structure behind the migrating boundary of deformed grain 2 occurs at the interface. (c) The migration boundary is free from the dislocation structure. (Humphreys and Hatherly (42))

As shown in Figure 10(b), deformed grain 1 has energy E_1 , which is higher than the energy E_2 in deformed grain 2, $E_1(=0.5\rho_1Gb^2) > E_2(=0.5\rho_2Gb^2)$.⁷³ The higher energy grains drag along a pocket of lower energy grains. Finally, they form a new dislocation free region at the interface. Here, E is the stored deformation energy, which can be explained in terms of the dislocation density, ρ . G is shear modulus, and b is the magnitude of Burgers vector. This implies that the dislocation density in grain 1 is greater than that in grain 2. A larger dislocation density corresponds to a smaller subgrain size according to below equation.

$$\rho^{1/2} = c_3 \delta^{-1} \quad (2-1)$$

This equation shows the relationship between subgrain size and the dislocation density within the subgrains. Here, δ is the subgrain diameter and C_3 is constant. Thus, larger subgrains correspond to a lower dislocation density.

A deformed grain with smaller subgrain size has higher stored energy than one with a larger subgrain size. As a result, it is expected that the new grains that come from an SIBM mechanism grow from the larger subgrain size region (grain 2) into the smaller subgrain size region (grain 1) through the bulging pre-existing high angle boundaries. Figure 11 shows optical images of SIBM in Al and Cu, taken from Bellier, Sperry (72) and Bailey, Hirsch (74), respectively.

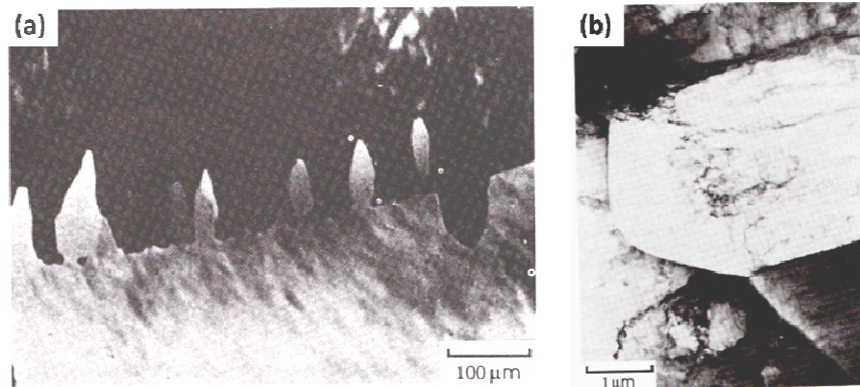


Figure 11 (a) An optical micrograph showing SIBM in Al (Bellier and Doherty 1977), (b) TEM image of SIBM in Cu deformed 14% in tension and annealed 5 minutes at 234°C (images from Bellier, Sperry (72) and Bailey, Hirsch (74), respectively)

Figure 11(b) shows the dislocation density of the bulge region, although lower than that of the parent grain, is significant, in agreement with Figure 10(b) and (c). SIBM involves the bulging of part of a preexisting grain boundary, leaving a dislocation-free region behind the migrating boundary as shown in Figure 10(c). In this case, the new grains have similar orientations to the old grains from which they have grown. This mechanism is especially important after low strains, i.e. strains at the micro scale, as already mentioned. It could result directly from the deformation process, because it is known that the dislocation storage rate may be dependent on grain orientation and be different in the boundary region. However, it could also arise from preferential recovery in the vicinity of a grain boundary which might increase the subgrain size and hence lower the dislocation density on one side of the boundary.⁴²

2.5 Deformation Energy and Mobility

Deformation energy from metal forming provides the driving force for subsequent microstructure phenomena during annealing. Every annealing process involves loss of some of the stored deformation energy and a corresponding change in microstructure. The change in microstructure is an important phenomena because it controls both the development and growth of the nuclei that will become recrystallized grains. During deformation the orientation of single crystals and of the individual grains of a polycrystalline metal change relative to the direction of the applied stress. This change is not usually random and involves lattice rotation associated with the crystallography of the deformation.

2.5.1 Stored Energy

Most of the energy in deforming a metal is given out as heat and very small amount of energy remains as stored energy in the metal. This stored energy that was introduced during deformation is derived from the point defects and dislocations generated during deformation. Only a small amount of the stored energy results from point defects, such as vacancies, while most of the stored energy, around 80-90%, generally comes from the generation of dislocations.^{44,45,77} Usually, grains with different orientations include different amount of stored energy because they undergo different amounts and different types of slip interactions during deformation.^{42,76} Table 3, taken from the reference 42 shows the different slip systems in fcc and bcc cubic metals.

Table 3 Crystallography of slip in cubic metals.
(Table from Humphreys and Hatherly (42))

Structure	Slip System	
	Plane	Direction
fcc	{111}	<110>
bcc	{110}	<111>
	{112}	<111>
	{123}	<111>

Stored energy is considered to be very important for discussing recrystallization behavior because it can influence both the nucleation of new strain-free grains and the growth rate of these new grains in the deformed matrix. In order to control this stored energy, one needs to know the variables that influence the amount of the stored energy. In general, impurities, deformation

mode, deformation temperature and initial grain size can be included as variables, and their effect is described as follows.

- As the impurity level in a metal increases, the stored energy increases.
- More complex and high deformation modes lead to higher stored energy.
- As deformation temperature decreases, the stored energy increases.
- Smaller grain size produces higher stored energy.

2.5.2 Microstructure of Deformed Metal

In cubic metals the two basic modes of deformations are slip and twinning, and the choice of mode is decided by the value of stacking fault energy. The deformation of high stacking fault energy metals like Al (166mJm^{-2}) takes place mainly by a slip mechanism. Conversely, the main mode of deformation for low stacking fault energy metals is twinning.⁴²

2.6 Geometrical Characterization for Grain Boundary Energy

As many of the properties of a grain boundary are dependent on its structure, knowledge of boundary structure is a necessary prerequisite to understanding grain boundary behavior. It is convenient to divide grain boundaries into those whose misorientation is greater than a certain angle and less than this angle as “high angle grain boundary” (HAGB) and “low angle grain boundary” (LAGB), respectively. The angle at which the transition from low to high angle boundaries occurs is generally taken as between 10° and 15° .⁴² In general, low angle grain boundaries are those which can be considered to be composed of an array of dislocations and

whose structure and properties vary as a function of misorientation, while high angle grain boundaries are those whose structure and properties are not usually dependent on the misorientation. There are special high angle grain boundaries which do have characteristic structures and properties, and they are referred to as the coincident site lattice (CSL) boundaries.

2.6.1 Low Angle Grain Boundaries **(Misorientation)**

A low angle boundary or sub-boundary can be represented by an array of dislocations.⁷⁷ The simplest form of this boundary is the symmetrical tilt boundary as shown in Figure 12. The lattices on either side of the boundary are related by a misorientation about an axis which lies in the plane of the boundary.

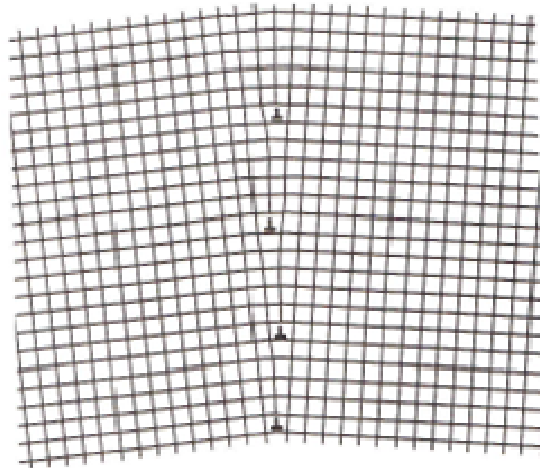


Figure 12 A symmetrical tilt boundary (image from Humphreys and Hatherly (42))

If the spacing of the dislocations of Burgers vector b in the boundary is h , then the crystals on either side of the boundary are misoriented by a small angle θ .

$$\theta \approx \frac{b}{h} \quad (2-2)$$

The energy per unit area of such a boundary γ_s , is given by Read and Shockley in 1950 as shown below.

$$\gamma_s = \gamma_0 \theta (A - \ln \theta) \quad (2-3)$$

γ_0 depends only on the orientation of the grain boundary and the macroscopic elastic constants:

$$\gamma_0 = Gb(\cos \varphi + \sin \varphi) / 4\pi(1 - \nu) \quad (2-4)$$

Where G is the rigidity modulus and ν is Poisson's ratio. The factor $(\cos \varphi + \sin \varphi)$, which is proportional to the total density of dislocations for a fixed value of θ , is valid only for $0 < \varphi < \pi/2$.

Thus, γ_0 becomes

$$\gamma_0 = Gb / 4\pi(1 - \nu) \quad (2-5)$$

The A in equation (2-3) depends upon φ , therefore A becomes

$$A = 1 + \ln(b / 2\pi\gamma_0) \quad (2-6)$$

According to this equation, the energy of tilt boundary increases with increasing misorientation (decreasing h) as shown in Figure 13. Combining equations (2-2) and (2-3), it is noted that as θ increases, the energy per dislocation decreases as shown in Figure 13, such that a material will

achieve a lower energy if the same number of dislocations are arranged in fewer, but higher angle boundaries.

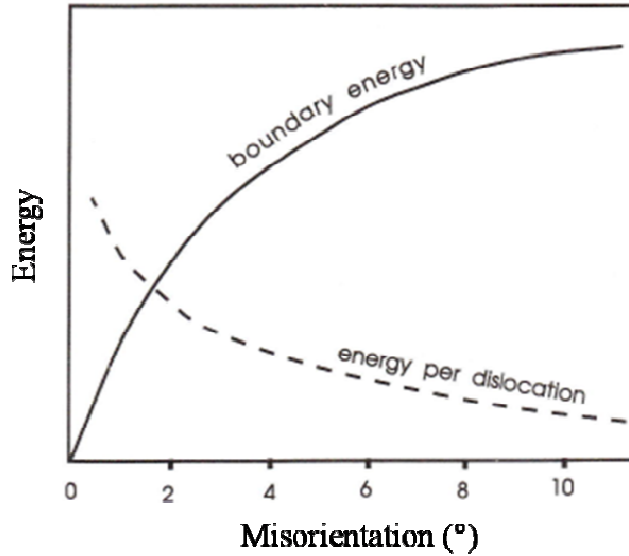


Figure 13 Energy of tilt boundary and the energy per dislocation as a function of the crystal misorientation. (image from Humphreys and Hatherly (42))

It is often convenient to use equation (2-3) in a form where the energy and misorientation are normalized with respect to the maximum values of those parameters (γ_m and θ_m) when the boundary becomes a high angle boundary.

$$\gamma = \gamma_m \frac{\theta}{\theta_m} \left(1 - \ln \frac{\theta}{\theta_m} \right) \quad (2-7)$$

As shown in Figure 14, the theory is in good agreement with experimental measurements for a small value of θ , although it is unreasonable to use this dislocation model for large misorientation,⁷⁸ because when θ exceeds 15° , the dislocation cores will overlap, the dislocation

will lose their identity and the simple dislocation theory on which equation (2-3) is based becomes inappropriate.

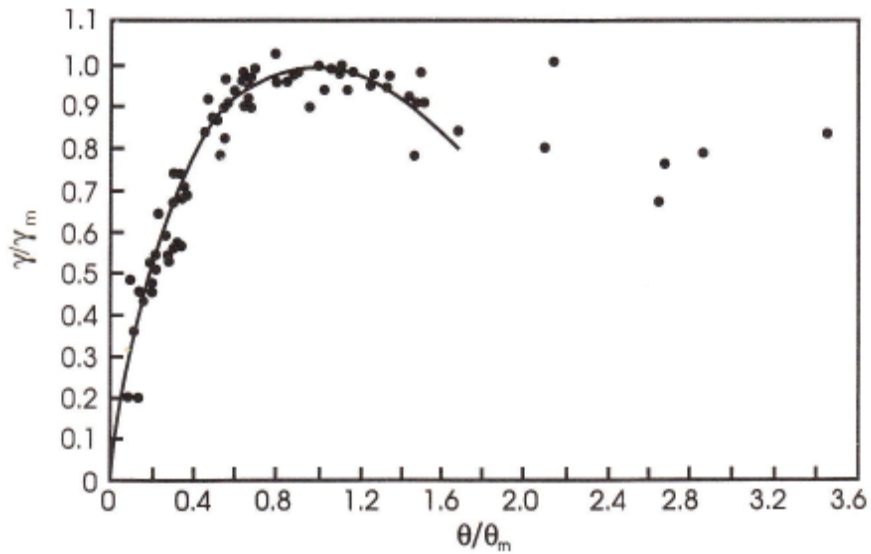


Figure 14 The measured (symbols) and calculated (Solid line) energy of low angle tilt boundaries as a function of misorientation, for different metals. (image from Humphreys and Hatherly (42))

C.G. Dunn and Lionetty⁷⁹ measured grain boundary energies on a relative scale as a function of difference in orientation, θ . The samples used were silicon iron with the (110) plane in the plane of the sample. Dunn's data in relative units are shown in Figure 15.

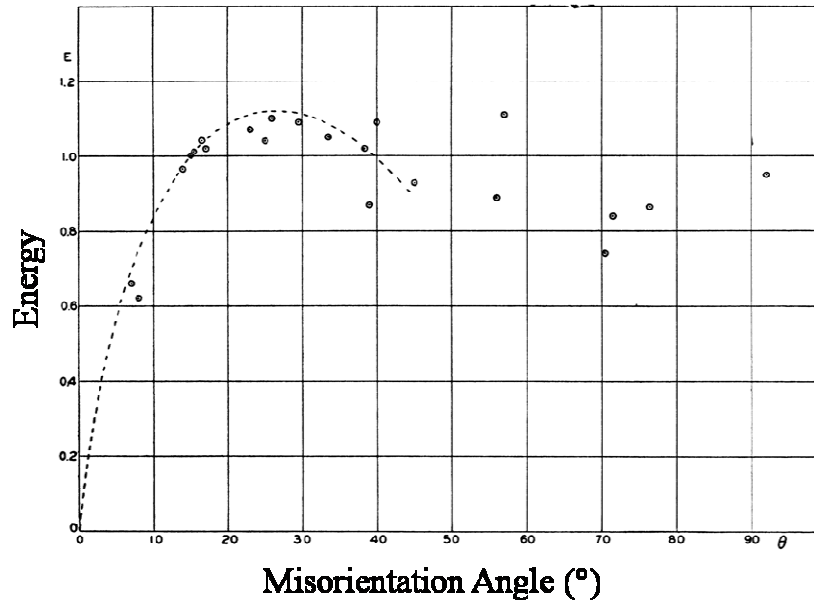


Figure 15 The measured (symbols) and calculated (Dotted line) grain boundary energy as a function of misorientation. Theoretical curve has $A=0.231$.
(image from Dunn and Lionetti 79)

The plot in Figure 15 has some striking features: a steep rise of energy with increasing θ in the range 0° to 15° , a maximum and relatively constant energy 20° to 30° , and a dip at about 70° . The theoretical curve is shown in Figure 15, to 45° and it fits the data surprisingly well even at large angles. This result suggests that compensating errors may cause equation (2-3) to be valid over a larger range than is justified by its derivation. Finally, based on grain boundary energy, for example in Fe-Si steels, the boundaries with misorientation of 20 - 45° have high energy and are classified as high energy grain boundary (HEGB) by Dunn. A detailed discussion concerning these boundaries is presented in chapter 3.

2.6.2 High Angle Grain Boundaries

(Coincident Site Lattice (CSL))

A coincident site lattice (CSL) is defined as an intersection lattice of any two crystal lattices as shown in Figure 16. If some lattice points in the two lattices coincide (the solid circles in Figure 16), then these points form the CSL. The CSL is considered the smallest sublattice of the two adjoining grains. The degree of coincidence is characterized by the reciprocal density of common lattice points, denoted as Σ . For example in Figure 16, Σ is 5. In this case, the rotation angle and rotation axis between two grains are 36.87° and $\langle 100 \rangle$, respectively. In general, where there is no special orientation relationship between the grains, Σ is large and the boundary, which has no special properties, is often referred to as a random boundary. However, for certain orientation relationships for which there is a good fit between the grains, Σ is small and this may confer some special properties on the boundary. For example, $\Sigma 3$ is the coherent twin boundary and $\Sigma 1$ is low angle grain boundaries. Table 4 shows the relationship between Σ and the rotation axes/angles for coincident site lattices of $\Sigma < 31$.⁸⁰ It is reported that the low energy CSL boundaries; $\Sigma(3-9)$ migrate faster than other CSL boundaries due to less segregation of second phase particles and it affects Goss-textured AGG in Fe-3%Si.⁸¹ Thus CSL boundary foundation and migration will be analyzed to assess if they play a role in the development of Goss-textured AGG in Galfenol rolled sheet. Detailed information on this study is in chapter 3.

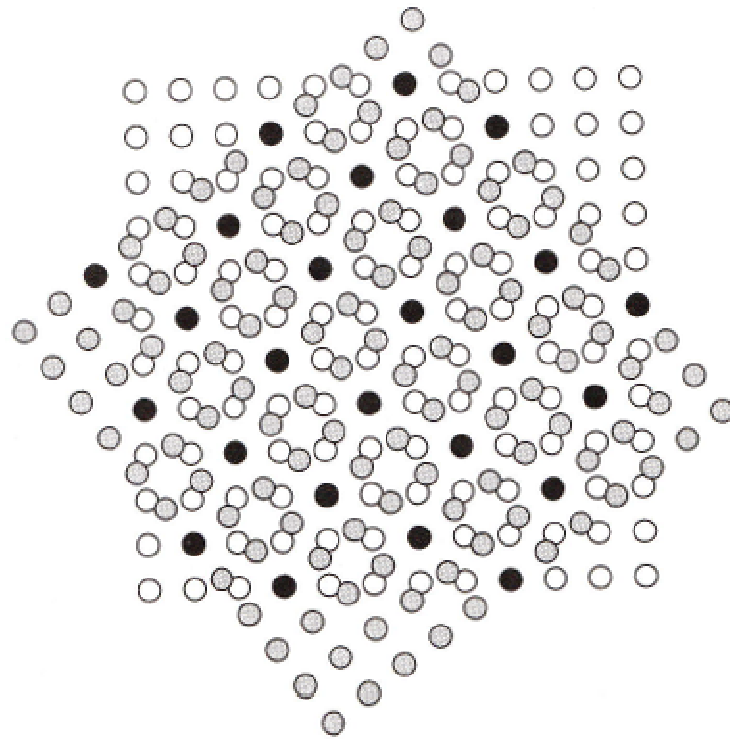


Figure 16 A coincident site lattice ($\Sigma 5$) formed from two simple cubic lattices rotated by 36.87° for an $\langle 001 \rangle$ axis.(image from Humphreys and Hatherly (42))

Table 4 Rotation axes and angles for coincident site lattices of $\Sigma < 31$.
(Table from Mykura (80))

Σ	$\theta_{\max.}^{\circ}$	Axis
1	0	any
3	60	$\langle 111 \rangle$
5	36.87	$\langle 100 \rangle$
7	38.21	$\langle 111 \rangle$
9	38.94	$\langle 110 \rangle$
11	50.48	$\langle 110 \rangle$
13a	22.62	$\langle 100 \rangle$
13b	27.80	$\langle 111 \rangle$
15	48.19	$\langle 210 \rangle$
17a	8.07	$\langle 100 \rangle$
17b	61.93	$\langle 221 \rangle$
19a	26.53	$\langle 110 \rangle$
19b	46.83	$\langle 111 \rangle$
21a	21.79	$\langle 111 \rangle$
21b	44.40	$\langle 211 \rangle$
23	40.45	$\langle 311 \rangle$
25a	16.25	$\langle 100 \rangle$
25b	51.68	$\langle 331 \rangle$
27a	31.58	$\langle 110 \rangle$
27b	35.42	$\langle 210 \rangle$
29a	43.61	$\langle 100 \rangle$
29b	46.39	$\langle 221 \rangle$

Chapter 3: Grain Boundary Energy for Goss-textured AGG in Galfenol Rolled-Sheet

3.1 Introduction

Recent work has shown annealing 1.0 mol.% NbC particle added-Galfenol rolled sheet under Ar atmosphere for 3 hours produces the advantageous growth of abnormally large Goss-textured $\{110\}\langle 001\rangle$ grains.^{82,83,84}

It is shown that, unlike the typical growth of average grain size that takes place with high temperature anneals, annealing Fe₈₁Ga₁₉ plus 1.0 mol.% NbC rolled sheet under Ar for 3 hours produces Goss $\{110\}$ grains of as large as several millimeters in diameter, i.e. that are abnormally large compared with the 130-micron size on average of $\{100\}$ and $\{111\}$ grains.⁸³ In this system, the dispersion of NbC particles promotes this abnormal grain growth in the same manner as the precipitation of second phase particles such as AlN and MnS that are used as inhibitors of normal grain growth in silicon steel.^{85,86} Although production of Goss-grain oriented silicon steel dates back to 1934,⁸⁷ the driving mechanisms associated with grain boundary energy, surface energy and/or particle pinning, are still not clear. One viable model for developing Goss texture is based on grain boundary energy differences associated with the relative angles between grains at their boundaries. Grain boundary energy can influence grain boundary mobility, which in turn determines the final texture configuration and grain size distribution.^{88,89,90} Thus, in this chapter, the geometrical characterization of grain size and orientation as it relates to the role of misorientation angle and CSL boundaries in promoting abnormal grain growth (AGG) in Galfenol rolled sheet was studied.

3.2 Two candidate models for Goss-textured AGG

Two main models are used to quantify the grain boundary characteristics in Goss-textured AGG in silicon steel. One model is the Coincident Site Lattice (CSL) model and the other model is the High Energy Grain Boundary (HEGB) model.

3.2.1 The Role of Coincident Site Lattice (CSL) for Goss-Textured AGG in Fe-Si

According to CSL model in silicon steel, the CSL boundaries with low grain boundary energy migrate faster than other boundaries due to less segregation of second phase particles at CSL boundaries.^{91,92} One group of researchers⁸¹ shows data for Fe-3%Si steel that suggest high mobility, low energy Σ 3- Σ 9 CSL boundaries are displaced during abnormal growth of Goss grains as shown in Figure 17. (Here, Σ 3 boundaries indicates the presence of twin boundaries with a 60° rotation angle $\langle 111 \rangle$ rotation axis, while Σ 5, Σ 7, Σ 9 indicate 36.86°, 38.21°, and 38.94° rotation angles $\langle 100 \rangle$, $\langle 111 \rangle$, and $\langle 110 \rangle$ rotation axis, respectively.) Their Goss-textured AGG data shows the number fraction of high mobility and low energy CSL boundaries is lower by over 50% compared with what is observed prior to Goss-textured AGG. Figure 17 shows the variation of CSL distribution before and after Goss-textured AGG in Fe-Si.⁸¹ The number fraction of Σ (3-9) CSL boundaries show a significant deficit in frequency of occurrence following AGG phenomena. It should be noted that, if indeed the growth of Goss grains is independent of grain boundary structure, the frequency of occurrence of CSL boundaries along the abnormally grown grains would be expected to be somewhat consistent with that of before AGG. Aust and Rutter (1959a, b)^{93,94} demonstrated that the CSL boundaries are more mobile

than random boundaries up to an impurity level of 0.006wt %Sn in Pb.^{93,94} At higher impurity levels the difference between mobility of CSL and random boundaries disappears.⁴² Also, it has been reported that the speciality of the CSL boundaries for grain growth vanishes at a high temperature, around 1000°C.

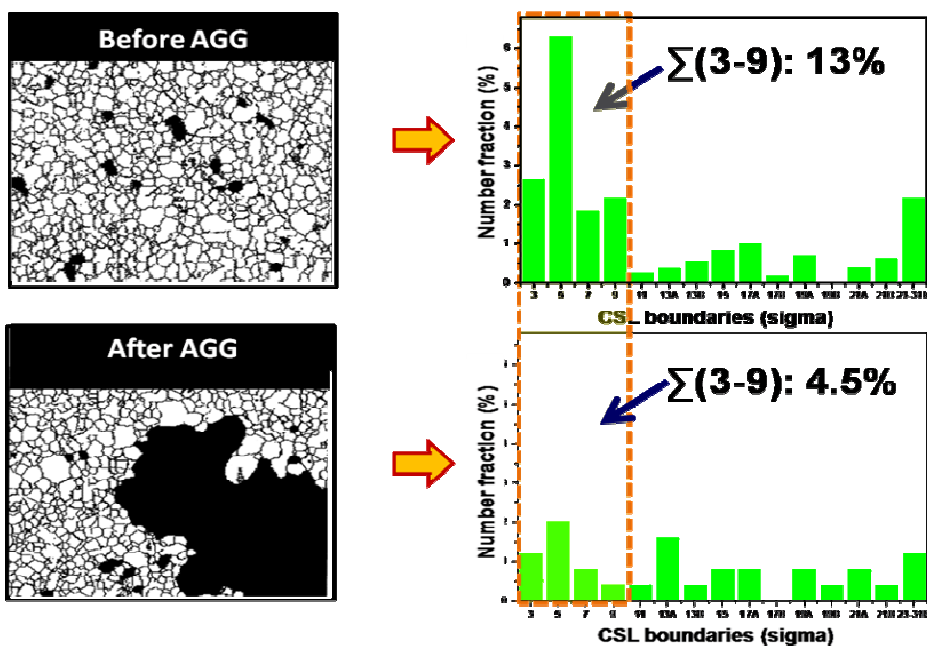


Figure 17 $\Sigma(3-9)$ CSL boundary distribution before and after Goss-textured AGG in Fe-3%Si alloy. (left side images from Lin, Palumbo, Harase and Aust (81))

3.2.2 The Role of High Energy Grain Boundary (HEGB) for Goss-Textured AGG in Fe-Si

Dependence of grain boundary energy on misorientation angle was recognized a long time ago. Dunn and Lionetti (79) measured the grain boundary energy as a function of different misorientation angle for $\langle 100 \rangle$, $\langle 110 \rangle$ and $\langle 111 \rangle$ tilted boundaries in Fe-Si. The relative grain boundary energy from their study is shown in Figure 18.

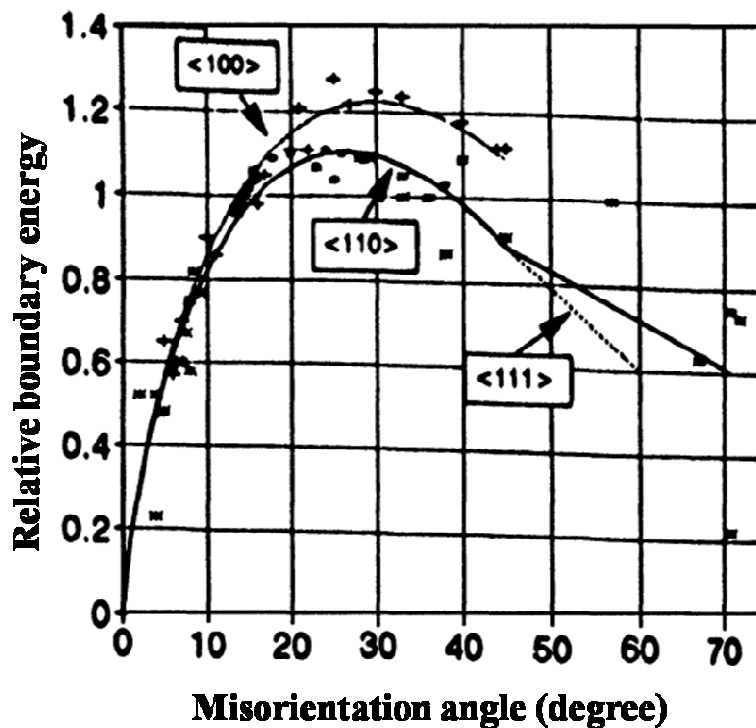


Figure 18 The relative grain boundary energy as a function of misorientation angle for $\langle 100 \rangle$, $\langle 110 \rangle$ and $\langle 111 \rangle$ tilt boundaries in Fe-3% Si steel.

(This graph obtained by Dunn and Lionetti (79) and this figure obtained from Rajmohan, Szpunar and Hayakawa (95))

Figure 18 shows that the grain boundaries with middle angle misorientation in the range of 20° - 45° has higher boundary energy than the other ranges of misorientation angle, i.e. $<20^{\circ}$ and $>45^{\circ}$. The direction of grain boundary migration is determined by the grain boundary energies. At high concentrations of alloying elements and at high processing temperatures, the HEGBs have the highest mobility and the highest precipitate coarsening rate, and consequently are released for migration earlier than other boundaries in an alloy. This is the HEGB model that is used to explain the Goss-textured AGG in Fe-Si. According to this model,^{96,97} Goss-textured AGG occurs preferentially when Goss grains are surrounded by grains at misorientation angles associated with high energy states: the range of 20° - 45° misorientation angle.

The applicability of these two models (CSL and HEGB) to 1mol.% NbC added-Galfenol rolled sheet was investigated in this chapter using Grain Boundary Character Distribution (GBCD) data to provide statistical information on the overall sample grain boundary microstructure and using quantitatively characterized data from Orientation Imaging Microscopy (OIM).⁹⁸ Both CSL and HEGB models were considered as possible mechanisms to explain the contribution of grain boundary energy to Goss-textured AGG observed in high temperature annealed $(\text{Fe}_{81}\text{Ga}_{19})+1.0 \text{ mol\%NbC}$ rolled sheet.

3.3 Detailed Experimental Procedure

An $(\text{Fe}_{81}\text{Ga}_{19})+1.0 \text{ mol\%NbC}$ alloy button with a thickness of $\sim 7.8\text{-mm}$ and a mass of $\sim 50\text{g}$ was prepared by arc-melting at the DOE Ames Laboratory.⁸³ During hot rolling, the button was enclosed in 321-stainless steel to prevent oxidation. The canned specimen was hot rolled at 1000°C until a 63% thickness reduction was achieved (2.85-mm). Subsequently, 700°C hot

rolling was undertaken to obtain a 49% reduction (1.45-mm). Finally, 0.31-mm thick rolled sheet was obtained after 500°C warm rolling for an additional 79% reduction. Specimens with a dimension of 12 mm x 12 mm x 0.31 mm were cut from the rolled sheet for subsequent annealing. Specimens were annealed in a tube furnace at 1200°C for different annealing times under an Ar atmosphere. Specimens were water-quenched after annealing. The saturation magnetostriction of samples was measured by rotating samples in between two Nd-Fe-B permanent magnets separated by a distance of 38.1-mm. The nominal magnetic field at the sample position was 3500-Gauss. The peak to peak saturation magnetostriction value of $(3/2) \lambda_s = \lambda_{\parallel} - \lambda_{\perp}$ was obtained using strain gauges attached to the specimen. Electron Backscattering Diffraction (EBSD) patterns were captured and analyzed using Orientation Imaging Microscope (OIM) software to obtain inverse pole figures (IPF), grain boundary information, and texture (details on EBSD are presented in Appendix A). EBSD analysis was carried out using a grain boundary dilation clean-up process in Tex SEM Laboratories (TSL) OIM software to remove spurious observations and to observe particles with a minimum grain size of $\sim 210 \mu\text{m}$ (10 pixels) and a maximum misorientation angle (5°) between pixels within a single grain. The NbC particles were examined by energy dispersive x-ray spectroscopy (EDS) in a scanning electron microscopy (SEM).

3.4 Results

3.4.1 Magnetostriction vs Texture Variation

The magnetostriction of 1mol.% NbC added Galfenol rolled sheet sample annealed at 1200°C for different lengths of time are shown in Figure 19 (personal communication with Na). Magnetostriction (± 5 ppm) of the sample as a function of anneal time increases from 28ppm for the as-rolled sample to 63ppm for the sample A which was annealed for 2 hours and increased to 163ppm for sample B which was annealed for 3 hours. Longer annealing times resulted in a decrease of magnetostriction of up to 106ppm in sample C for a 4 hour anneal and further to 63ppm for a 5 hour anneal duration. The highest magnetostriction was observed from a 3 hour annealed sample B.

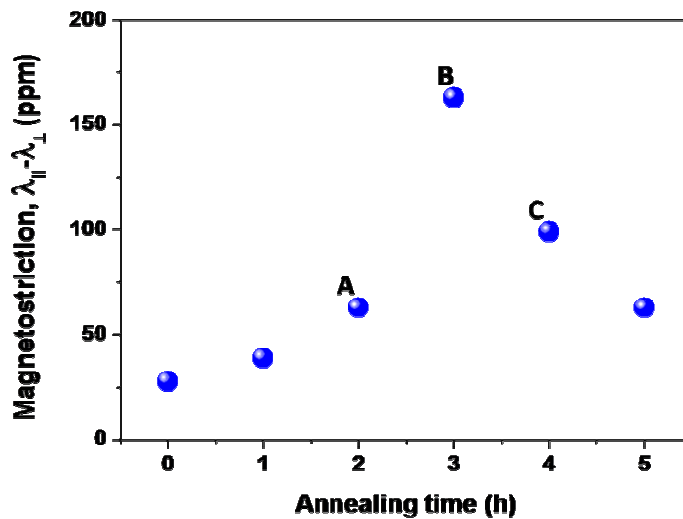


Figure 19 Magnetostriction of 1.0 mol.% NbC added Galfenol rolled sheet as a function of annealing time at 1200°C under Ar atmosphere.

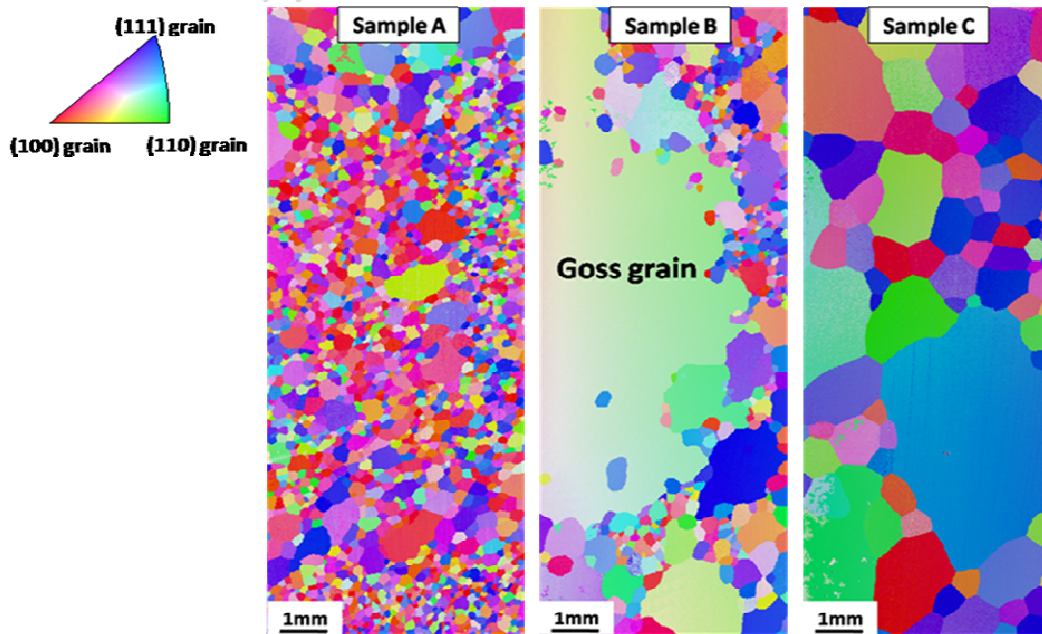



Figure 20 IPF image along normal direction of 1.0 mol.% NbC added Galfenol rolled sheet samples A, B, and C, which were annealed for 2, 3, and 4 hours under Ar atmosphere, respectively.

IPF images were obtained to confirm the relationship between magnetostriction and texture as a function of annealing time. The grain size and orientation in samples A, B, and C are shown in Figure 20. Relatively small and randomly oriented grains were observed from sample A that was annealed for 2 hours. The Goss-textured AGG was observed from sample B that was annealed 1 hour more than sample A, and the overall grain growth was observed in sample C with normal grain growth mode.

The average grain size grows with anneal time as expected from Figure 20. In sample B, the area fraction of {110} or Goss grains is significantly higher than {100} and {111} grains making up 65.8% of the area fraction of grains on normal direction (ND). The much larger maximum grain size (5037.5 μm) of sample B produces the high area fraction of Goss grains. The textures observed in orientation distribution functions (ODF) at $\psi_2=45^\circ$ are varied in samples A (α -fiber and γ -fiber) and C (Goss and γ -fiber), but are predominately Goss in sample B. The lattices within the Goss grains of sample B are on average tilted about 24° from the rolling direction (RD). (The tolerance range that specifies the minimum and maximum misorientation angle of grain is $0^\circ - 30^\circ$.) Table 5 shows details from OIM and GBCD analysis of samples A, B and C.

For samples A, B and C respectively, 10.9%, 12.2% and 7.9%, of the grain boundaries are associated with coincident alignment of the lattices of adjacent grains, while 53.7%, 48.4% and 52.0% of grain boundaries are associated with the 20° - 45° misorientation angles that correspond to high energy and high mobility.^{77,99} Prior Fe-Si studies⁸¹ suggest a decrease in low level of CSL boundaries ($\Sigma 3$ -9) when AGG of Goss grains are present, although sample B has the highest number fraction of CSL. The GBCD data in Table 5 provide a first indication that the CSL model is not likely to explain the AGG in sample B, but this data does not suggest whether the HEGB model might be applicable or not. More detailed study for CSL and misorientation distribution around each grain is discussed in section 3.4.2 and 3.4.3 of this chapter.

Table 5 Details from OIM and GBCD of 1mol.% NbC added Galfenol rolled sheet samples A, B and C which were annealed for 2, 3, and 4 hours under Ar atmosphere, respectively

Sample ID	Magnetostriction (ppm)	Area Fraction of grains (%) (on ND) ^a	Texture in ODF (at $\psi=45^\circ$)	Tilted Angle of Goss texture ($^\circ$) (from RD) ^b	Average grain size diameter (μm)	GBCD (%)	
						CSL	Misorientation ^c
A	63	(100):41.3	α -fiber, and γ -fiber	-	152.2	10.9	1:17.6
		(110):24.7			Min.:33.8		2:53.7
		(111):34.0			Max.:789.8		3:28.7
B	160	(100):12.1	Tilted Goss	24 	220.1	12.2	1:12.5
		(110):65.8			Min.:35.5		2:48.4
		(111):22.2			Max.:5037.5		3:39.1
C	106	(100):20.1	Tilted Goss and γ -fiber	-	540.9	7.92	1:10.9
		(110):30.2			Min.:35.2		2:52.0
		(111):49.7			Max.:3453.4		3:37.1

*a: on Normal direction

*b: from Rolling direction

*c: 1: Low angle ($2^\circ - 20^\circ$)

2: Middle angle ($20^\circ - 45^\circ$)

3: High angle ($45^\circ - 65^\circ$)

(Only boundaries between identified grains)

3.4.2 The Role of CSL Boundaries in Galfenol Rolled Sheet

Figure 21 shows the CSL distribution of samples A, B and C. The number fraction of $\Sigma(3-9)$ boundaries slightly increases in samples B with Goss-textured AGG and drops in sample C, where Goss grain AGG is no longer present. In sample C, overall CSL boundaries decrease and normal grain growth is evident. This is not consistent with the observations of Fe-Si⁸¹ and further suggests that low level of CSL boundaries are not the dominant driving force behind AGG in Ar-annealed Galfenol rolled sheet. This supports that the CSL model does not explain AGG in Galfenol rolled sheet.

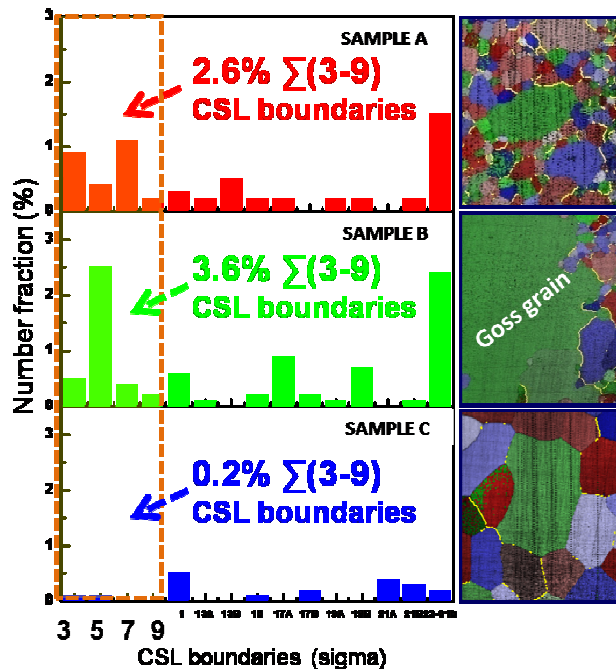


Figure 21 CSL boundary distribution of sample A, B and C, which were annealed for 2, 3, and 4 hours under Ar atmosphere, respectively.

Figure 21 was obtained using a grain boundary dilation clean-up process in Tex SEM Laboratories (TSL) OIM software. This clean-up process removed an interesting peak that was detected from the same samples when OIM was carried out without clean-up process. In samples B and C, the number fraction of $\Sigma 13b$ boundaries was almost 3.5%, i.e. much larger than all other CSL boundaries as shown in Figure 22. The minimum rotation angle and rotation axis of $\Sigma 13b$ boundary are 27.29° and $\langle 111 \rangle$. The increase from $\sim 0.5\%$ in sample A to $\sim 3.5\%$ in sample B may explain the global increase in CSL noted in the GBCD data in Table 5 while other CSL boundaries do not increase much. It was found that the number fraction of $\Sigma 13b$ boundaries was particularly sensitive to scan resolution, something that was not observed for other CSL boundaries. With scan resolution set for to identify a minimum grain size of 1 pixel or $\sim 21\mu\text{m}$, i.e., without filtering of data with the digital data clean up process, the number fraction of $\Sigma 13b$ boundaries in sample B and C grew to 32.2% and 22.2%, respectively. Thus, the number fraction of $\Sigma 13b$ CSL boundary is affected by the presence of small surface features that appear coincident with the onset of AGG but are “smoothed over” in data analyzed with the OIM clean up process. It is reported by Stiegler et al. that $20\text{-}30^\circ$ rotation angle and $\langle 111 \rangle$ rotation axis are the commonly founded orientation for rapid growth of Nb.¹⁰⁰ This orientation is well matched with the orientation of $\Sigma 13b$ and it is suggested that $\Sigma 13b$ peak is detected from the NbC particles that are distributed on the surface of Galfenol rolled sheet.

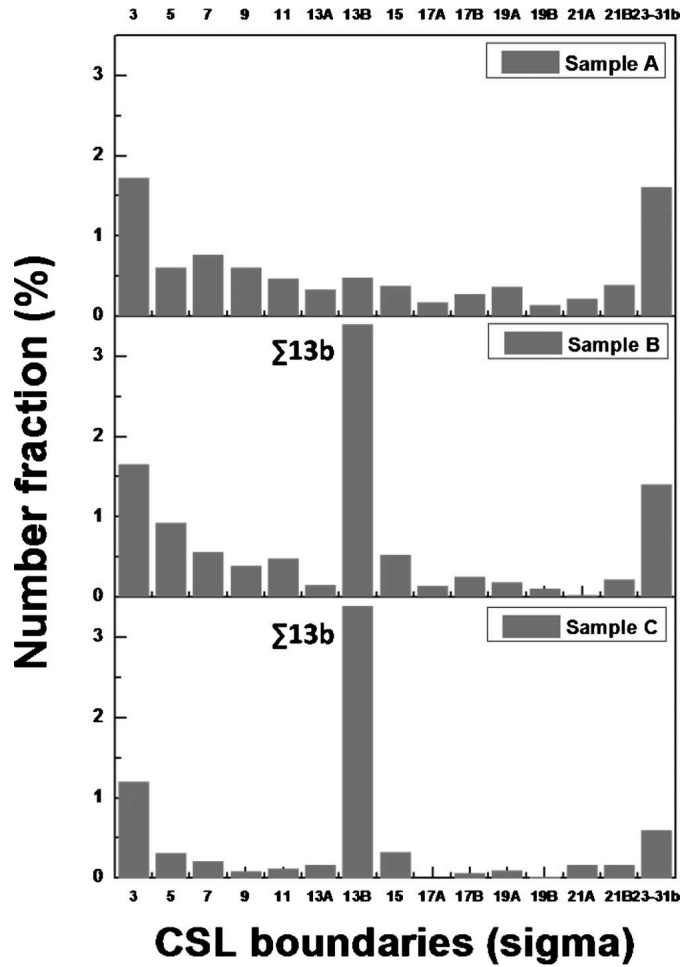


Figure 22 CSL boundary distribution of sample A, B and C, which were annealed for 2, 3, and 4 hours under Ar atmosphere, respectively. (without OIM clean up process)

3.4.3 The Role of Misorientation in Galfenol

Based on the background on HEGB model that is mentioned in chapter 3.2.2, the misorientation distribution around the Goss-textured AGG in 4 hour annealed sample was observed. Figure 23 shows the different misorientation angle distribution around Goss-textured AGG in Galfenol. As shown in Figure 23, abnormally grown Goss-textured grain predominantly surrounded by grains with a middle angle (20° - 45°) misorientation and high energy. A much smaller fraction of grains at low and high misorientation angles surround the abnormally grown Goss grain.

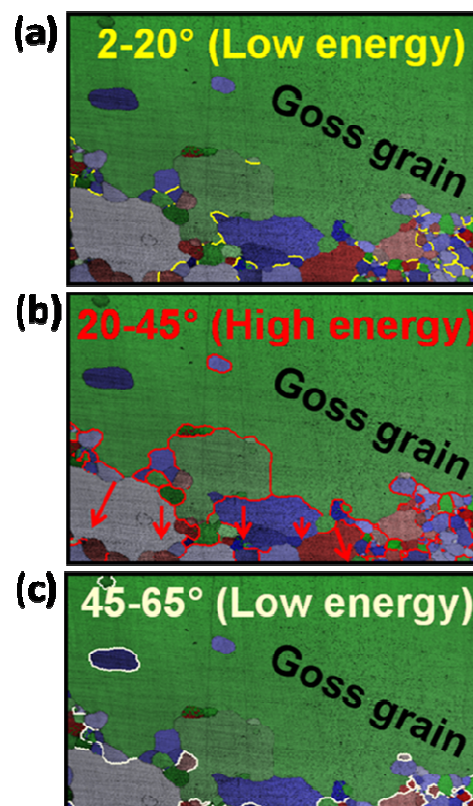


Figure 23 Grain boundaries of different misorientation angle around an abnormally grown Goss-textured grain in 1mol.% Galfenol rolled sheet. (a) low grain boundary energy with low angle misorientation ($<20^{\circ}$), (b) high grain boundary energy with middle angle misorientation ($20^{\circ}<\theta<45^{\circ}$), and (c) low grain boundary energy with high angle misorientation ($>45^{\circ}$)

Each grain within a sample was selected and then normalized to observe the misorientation angle distribution shown in Figure 24. Then the total misorientation angle distribution from samples A, B and C were investigated.

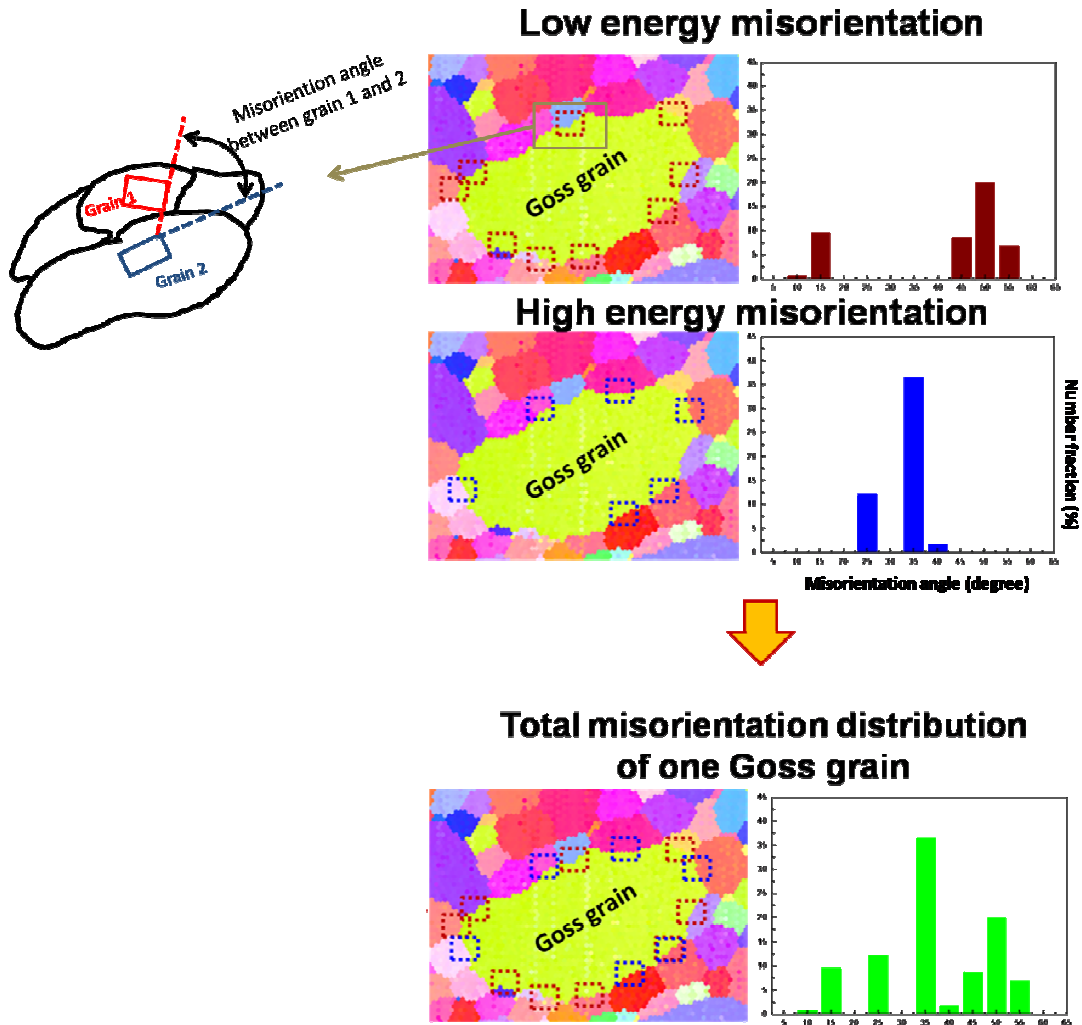


Figure 24 Normalization of grain boundary misorientation angle distribution from each grain.

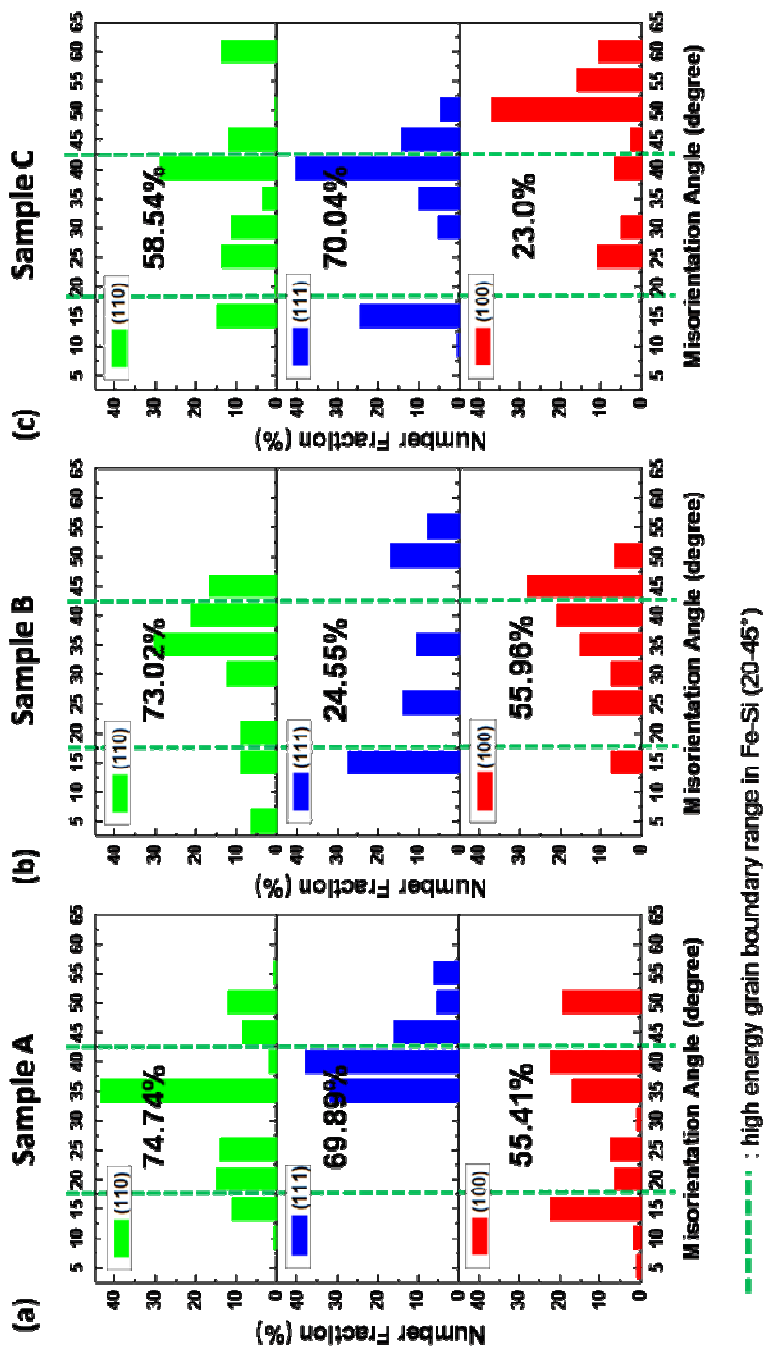


Figure 25 Misorientation angle distribution around each (110), (111) and (100) grain (top to bottom) in Galfenol rolled sheet samples A, B and C (left to right) that annealed 2, 3 and 4 hours under Ar atmosphere, respectively.

In sample A, both the Goss and γ -fiber grains are surrounded by a high number fraction of the high energy, middle angle misorientation boundaries: 75% for the Goss {110} grains and 70% for the γ -fiber {111} grains compared to 56% for {100} grains. The slightly higher fraction of middle angle misorientation boundaries surrounding Goss-grains in Figure 25(a) could indicate the 2-hour anneal state is a suitable precursor to the onset of Goss grain AGG. In Figure 25(b), the number fraction of middle angle misorientation boundaries around the Goss-grain is much higher than those around other grains (γ -fiber and α -fiber grains): 73% compared to 25% for {111} and 56% for {100}. This high fraction of middle angle misorientation boundaries around the abnormally grown Goss grains is consistent with the HEGB model explaining AGG in Galfenol and indicates continued AGG is likely. In Figure 25(c), the fraction of middle angle misorientation boundaries around the Goss grains decreased as did the size of abnormally grown Goss grains (Table 5) while the average grain size in the sample grew. While this is not generally observed in FeSi steels, where AGG Goss grains are stable with extended duration of anneal at a given temperature, the phenomenon observed in Fe-Ga is similar to the observation described in ref. 42 that “*during AGG, a few grains in the microstructure grow and consume the matrix of smaller grains and a bimodal grain size distribution develops. However, eventually, the large grains impinge and normal grain growth resumes*”. Although we have not identified the mechanism responsible for resumption of NGG, these results indicate that to maximize AGG, annealing should end prior to the resumption of NGG, i.e., between 2 and 4 hours for a 1200°C anneal under Ar atmosphere. These results on the misorientation distribution around the Goss-textured AGG support the HEGB model in which high energy grain boundaries promote Goss-textured AGG in Galfenol rolled sheet.

3.5 Conclusion

The role of CSL and of the energy associated with misorientation between grain boundaries on abnormal Goss-textured grain growth in $(\text{Fe}_{81}\text{Ga}_{19})+1.0$ mol% NbC rolled sheet annealed under Ar was investigated. Average 0.45mm thick samples annealed for 2, 3 and 4 hours were studied. Although only the sample annealed for 3 hours exhibited Goss-textured AGG.

Grain boundary character distributions (GBCD) results for all three samples showed a global trend of that the number fraction of CSL boundaries remained fairly constant, which does not support CSL as the mechanism for promoting Goss-textured AGG. Further, OIM results, i.e., without filtering of data with the digital data clean-up process, that are presented show that $\Sigma(3-9)$ boundaries decrease only slightly with anneal time. It was noted that the most prevalent CSL boundaries ($\Sigma 13b$) in the 3 and 4 hour annealed samples are associated with NbC particles on the surface of Galfenol rolled sheet. GBCD results indicate the global presence of high energy grain boundaries in all three samples. Analysis of misorientation angle surrounding $\{110\}$, $\{111\}$ and $\{100\}$ grains in the three samples shows the fraction of high energy grain boundaries is highest for the abnormally grown Goss grain, 73% compared to 25% for the $\{111\}$ grains and 56% for $\{100\}$ grains in the 3 hour annealed sample. The high percentage of high energy, middle angle misorientation ($20^\circ - 45^\circ$) boundaries around abnormally grown Goss grains supports the HEGB model for Goss-textured AGG in $(\text{Fe}_{81}\text{Ga}_{19})+1.0$ mol% NbC rolled sheet.

Chapter 4: Deformation Energy on AGG I

- By Tension Annealing -

4.1 Introduction

In this chapter, the tension annealing method will be described to explain the use of tension as an approach for altering grain boundary energy and thereby promoting AGG by influencing the secondary recrystallization process in 1 mol% NbC-added Galfenol rolled sheet. Tension annealing is used to promote dynamic recrystallization (DRX). This is achieved by applying tension to produce a uniform strain state in the sample while simultaneously conducting a high temperature anneal. Several studies show that DRX promotes AGG in different materials, such as Mo, Cu and Al-Mg alloys.^{101,102,103} It is suggested that the observed recrystallization phenomenon in this method originates from the common consequence of the retention of a large amount of stored energy that is a result of the tension applied to the sample.⁴² One of the mechanisms of DRX is local structure rearrangement. During annealing, the material is constantly being deformed as new grains nucleate and grow. Once plastic deformation reaches a critical level, new, dislocation-free grains form in the deformed structure and increase boundary migration mobility by facilitating release of grain boundaries from pinning sites, such as oxide and/or carbide particles that can produce Zener pinning.^{101,104}

4.2 Experimental Procedure

A button of $(\text{Fe}_{81}\text{Ga}_{19})+1.0 \text{ mol.}\% \text{NbC}$ alloy that was 7.8-mm thick and had a mass of 50 grams was prepared at the Ames Laboratory, USDOE by arc-melting. The button was enclosed in a stainless steel bag to prevent oxidation during hot rolling. Following hot soaking at 1000°C , the enclosed sample was hot rolled to a thickness of 2.85mm (a 63% reduction in thickness). Throughout the hot rolling procedure, the bagged sample was reheated after every two passes for 10 minutes at 1000°C . Secondary hot rolling at 700°C provided a 49% reduction to give 1.45-mm thick sheet. Subsequently, warm rolling at 500°C was undertaken until the sample thickness was reduced to 0.31mm (79% reduction). Finally, dog bone samples with a dimension of 12mm x 6mm x 0.31mm were cut from the rolled sheet.

For tension annealing, an as-rolled sample was annealed at $800\text{-}1000^\circ\text{C}$ (60-70% of the melting temperature) with the simultaneous application of tensile loading and true strain rates of $(1 \times 10^{-5}/\text{s}) - (2 \times 10^{-4}/\text{s})$ under an Ar atmosphere. The system was held at the anneal temperature for roughly 30 minutes prior to applying tensile loads to accommodate thermal expansion of all materials and initiate testing from a steady state thermal condition.

Table 6 shows the summary of samples for tension annealing. Sample 1 tension annealed at 900°C with $2.57 \times 10^{-5}/\text{s}$ strain rate control and other samples 2 and 3 were tension annealed at 1000°C with strain rate of $2.0 \times 10^{-4}/\text{s}$ and $1.15 \times 10^{-5}/\text{s}$, respectively. Sample 4 was tension annealed at 1100°C , but strain rate was not controlled under this annealing temperature.

Table 6 Summary of samples for tension annealing

Samples	Tensioning Temperature (°C)	Strain Rate (/s)
Sample 1	900	2.57×10^{-5}
Sample 2	1000	2.0×10^{-4}
Sample 3	1000	1.15×10^{-5}
Sample 4	1100	Uncontrolled

Figure 26 shows the schematic diagram for the tension annealing system. A Terfenol-D actuator was used to manage the strain rate by controlling the Lab-view system as shown in Figure 26(a). The displacement produced by the Terfenol-D actuator was continuously detected via a laser displacement sensor. Two Terfenol-D actuators were connected to achieve the desired displacement length. The maximum displacement that could be controlled in the sample was about 1.7mm (15% of sample initial length). The titanium sample holder was prepared for a high temperature annealing process at around 1000°C, also titanium rods were used to connect titanium sample holder with Cu wire outside of the furnace. The length of titanium rod was 280mm and it has 5mm diameter. Also, the load-cell was established in this system to monitor the stress variation during tension annealing (Figure 26(c)). Finally, strain and stress variation were monitored during tension annealing as shown in Figure 27.

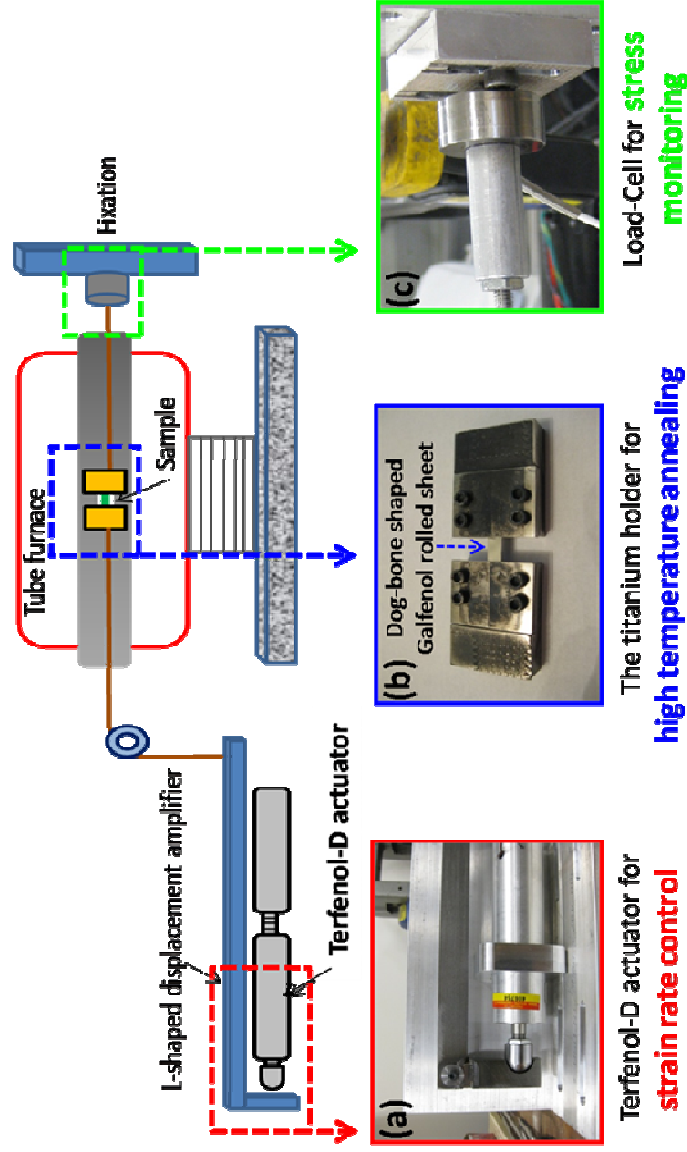


Figure 26 Schematic diagram for tension annealing system (a) Terfenol-D actuator for strain rate control, (b) titanium sample holder for high temperature annealing and (c) load cell for monitoring the stress variation

The strain rate was controlled by controlling the slope of Figure 27(a) and the state of deformation of the sample during tension annealing was ultimately observed from the stress variation curve detected by the load-cell, as shown in Figure 27(b).

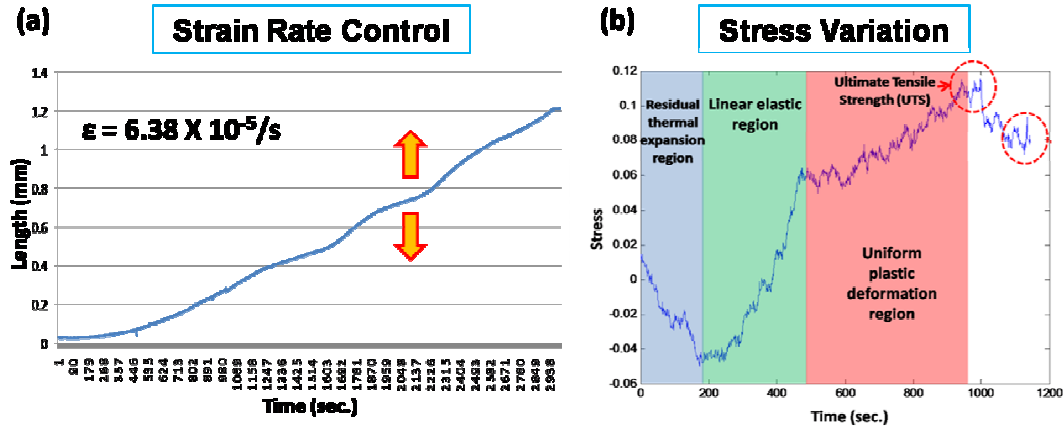


Figure 27 Monitoring the (a) strain rate and (b) stress variation of tension annealed Galfenol rolled sheet during tension annealing at 1000°C under Ar atmosphere.

4.3 Results and Discussion

Figure 28 shows the IPF image and ODF plot from the as-rolled sample before tension annealing.

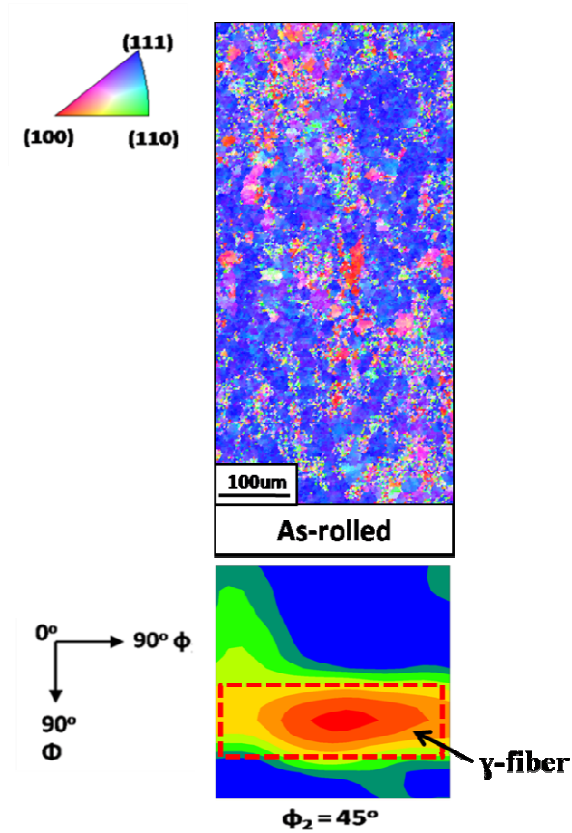


Figure 28 IPF and ODF plots of as-rolled Galfenol rolled sheet sample.

In this case, the area fraction of Cube texture: $\{100\}\langle 001\rangle$ was 12%, Goss texture: $\{110\}\langle 001\rangle$ was 17.1% and the γ -fiber texture: $\{111\}$ was 70.9%. As shown in these fractions, γ -fiber texture was dominant just after rolling process. The average grain size diameter was about 5.3 μm . This state of sample has very low magnetostriction, around 30ppm. This state is very reproducible.

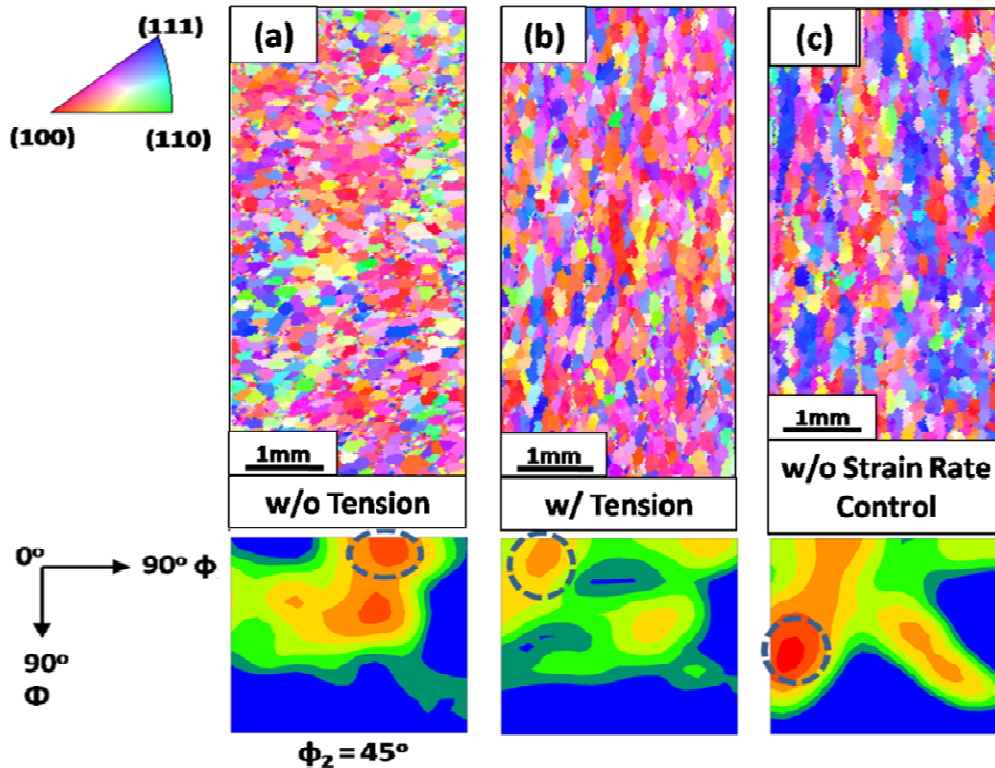


Figure 29 IPF images of tension annealed Galfenol rolled sheet samples along normal direction and ODF plots at different conditions: (a) annealed at 1000°C for 3 hours with no tension, (b) annealed at 1000°C for 3 hours with tension and strain rate control (2×10^{-4} /s), and (c) annealed at 1000°C without strain rate control but with a constant tensile load.

IPF images and ODF plots from different annealing conditions are shown in Figure 29. Those samples were annealed at 1000°C for 3 hours with (a) no tension, (b) uniform stress and (c) uniform strain. After annealing at 1000°C for 3 hours with no tension, some of the major γ -fiber texture in the as-rolled sample was changed to a $\{100\}$ texture with $\langle 110 \rangle$ and/or $\langle 100 \rangle$ orientation as the grain size increased over ten-fold to an average diameter of 60 μm (Figure

29(a)). After tension annealing at the same temperature with a constant strain rate of 2×10^{-4} /s, a small amount of elongation of the grains and lattice rotation was observed, as seen in Figure 29(b). The length of the sample increased by about 15% of the initial sample length and the average grain size was $95\mu\text{m}$, also larger than in the sample with no tension annealing. In this case, the estimated deformation energy of the sample was 93MPa. However, it seems that the deformation energy added to sample by tension induced strain was not stored in the sample due to simultaneous high temperature anneal process. The area fraction of Goss grains: $\{110\}\langle 001\rangle$ was 19.7% or 10.7% lower than in Figure 29(a) and the area fraction of Cube texture: $\{100\}\langle 001\rangle$ and $\{111\}$ grains were 48.1% and 32.2%, respectively, or 5.8% and 4.9% higher than in Figure 29(a). (The tolerance range that specifies the minimum and maximum lattice variation is $0^\circ - 30^\circ$.) Somewhat different texture variation is shown in Figure 29(c). In this case, a constant tensile stress of 75MPa was applied to the sample without any strain rate control at the same temperature until the sample failed. The gauge region of the sample started to thin and the sample failed due to fracture within first few minutes of loading. The failed sample had elongated to about 1.5 times longer than its initial state and it exhibited a γ -fiber texture similar to the as-rolled sample over 47% of the sample area fraction. These experiments were also conducted at a slightly lower anneal temperature, at 900°C , but in all cases, no AGG was observed. It is not clear if a different range of annealing temperature, critical strain and/or strain rate for DRX would produce AGG. To resolve this, additional tension annealing using the tapered dog bone sample approach used in the following chapter should be undertaken as future work.

4.4 Conclusion

The effect of tension annealing on AGG in $(\text{Fe}_{81}\text{Ga}_{19})+1.0 \text{ mol.}\% \text{NbC}$ rolled sheet was investigated. During tension annealing at 1000°C for 3 hours, a small amount of grain elongation and lattice rotation were observed under strain rate control tests where stress was sufficient to produce plastic deformation. The length of the sample increased about 15% of the initial sample length. The estimated deformation energy introduced into the sample was 93MPa. Tension annealing produced an increase in the area fraction of cube texture and $\{111\}$ grains compared with what was observed with no tension annealing. γ -fiber texture was predominant in the sample that was tension annealed without strain rate control. However, no DRX with AGG was observed from this process. These results are inconclusive and further study of DRX via tension anneal may yet be shown to produce AGG.

Chapter 5: Deformation Energy Effect on AGG II

- By Strain Annealing -

5.1 Introduction

In this chapter, strain annealing will be described to identify the deformation energy and study its effect as an alternative approach to tension annealing for introducing on AGG. In this process, the sample is tensioned with a constant displacement rate and then the sample is subjected to a high temperature annealing to produce strain-induced AGG. Strain annealing is used to ensure that deformation energy is stored in the sample prior to the high temperature anneal process which should promote strain-induced boundary migration (SIBM). SIBM involves bulging of part of a preexisting grain boundary produced by low deformation, leaving a dislocation-free region behind the migrating boundary as explained in chapter 2.4.5.1. The driving force for SIBM is presumed to arise from a difference in dislocation density introduced during tensile loading. Differences in dislocation density at the submicron scale form an energy balance that promotes discontinuous grain boundary motion.^{42,105} This is an important nucleation mechanism that arises due to strain annealing and differentiates strain annealing from normal annealing processes without tension.

Three important factors emphasized in this study are critical strain with specific deformation energy, strain rate and final annealing temperature. A minimum strain, called the critical strain, is necessary for initiation and propagation of new grains, after which the grain size decreases with increasing strain as shown in Figure 30.¹⁰⁶

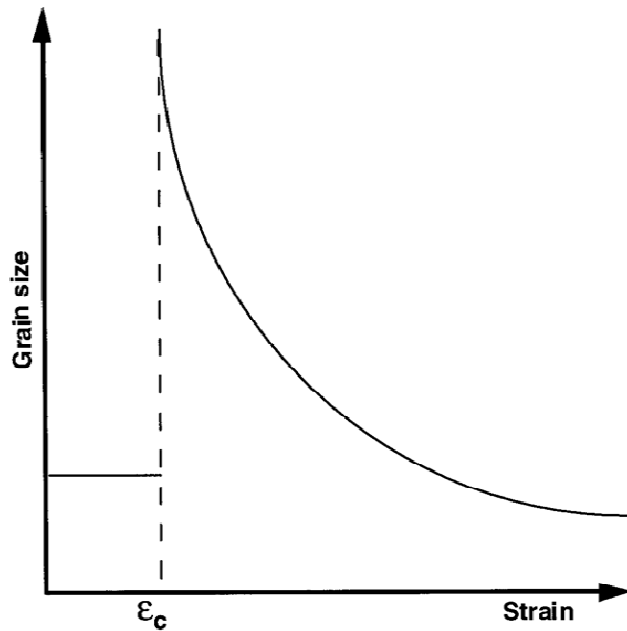


Figure 30 Schematic representation of variation of final grain size with strain.

(image from Chaubet, Fondere and Bacroix (106))

Strain rates of between 10^{-6} and 10^{-4} /s have been reported as being necessary to avoid a multiplication of the dislocation density and formation of multiple Luders bands that disturb the grain growth.^{107,108} In addition, annealing at temperatures of over 60% of melting temperature is needed for AGG in this process.

5.2 Strain Annealing with Preliminary Samples

5.2.1 Experimental Procedure

An $(\text{Fe}_{81}\text{Ga}_{19})+1.0 \text{ mol.}\% \text{NbC}$ ingot that was 15.25mm thick, 38mm wide and 51mm long was prepared by ETREMA products. During hot rolling, the ingot was enclosed in 321-stainless steel to prevent oxidation. The canned specimen was hot rolled at 1000°C until a

thickness reduction of 81% was achieved (2.54mm). Subsequently, 800°C hot rolling was undertaken to obtain a 73% reduction (0.76mm) and 500°C warm rolling was undertaken to obtain a 33% reduction (0.5mm). Finally, a 0.45mm thick rolled sheet was obtained after room temperature cold rolling. Several dog bone samples with two pin holes at each gripper region were obtained from as-rolled samples. Prepared samples were pre-annealed at 700°C under an Ar atmosphere for 10 hours to fully introduce primary recrystallized grains as shown in Figure 31.

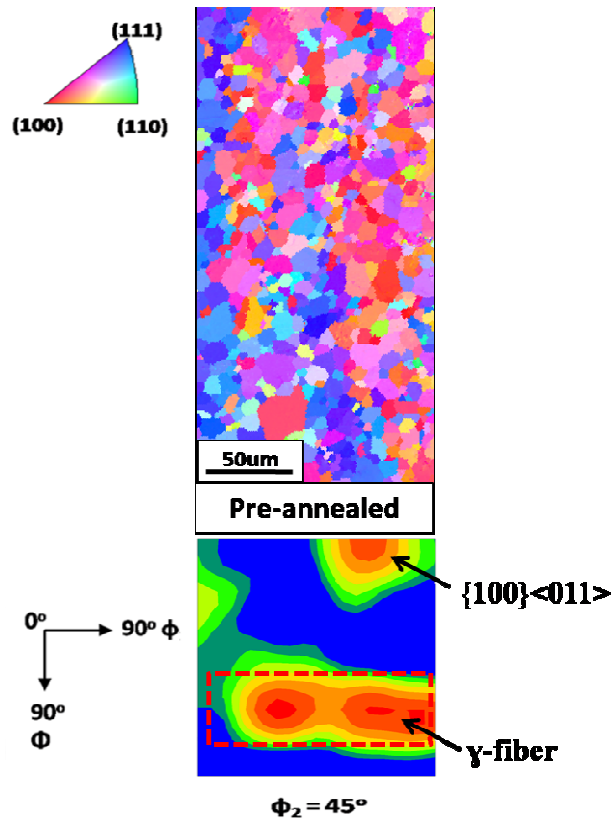


Figure 31 IPF and ODF plot of pre-annealed Galfenol sample at 700°C for 10 hours.

This pre-annealed homogeneous recrystallized sample does not contain any deformation energy from the rolling process. All stored deformation energy produced by rolling is consumed during pre-anneal in the process of primary recrystallization. The average grain size diameter is about 10 μ m and the area fraction of Cube and {111} texture is 41.3% and 45.3%, respectively. The temperature increased up to 300°C to soften the sample and then tension was applied with an Materials Test System (MTS) load stand to introduce the suggested critical strain in the sample and thereby maximize the stored strain energy available to promote AGG during the subsequent high temperature anneal. The sample was strained with a constant 5x10⁻⁴/s displacement rate control. Then the fractured samples were annealed at different temperature of 800°C and 1000°C to observe AGG.

5.2.2 Results

Figure 32 shows the true stress variation as a function of true strain. The steady-state strain rate was attained after a true strain of 0.01. At a strain of slightly less than a true strain of 0.08, the sample fractured outside of the gauge region, in an area adjacent to pinholes that were introduced to address a challenge in gripping the dog bone test samples. Plastic deformation of the sample is observed only around these pinholes. The upper part of the pinhole region fractured at an applied 210MPa true stress as shown in Figure 32. No visible elongation was observed on the gauge section that was originally the intended focus of this test. The sample was cut in half and used to investigate the effect of anneal at two temperatures, 800°C and 1000°C, for 1 hour under an Ar atmosphere. No texture or grain size variation was observed from the half dog bone sample that annealed at 800°C.

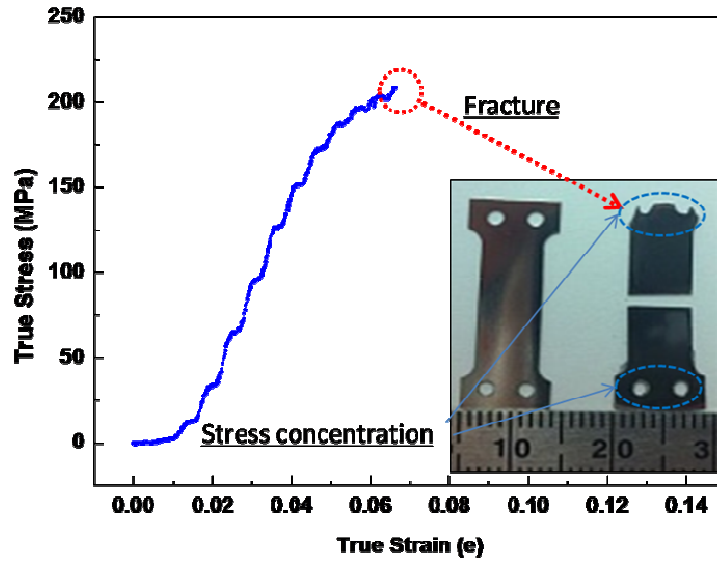


Figure 32 Experimental true stress & true strain curve and optical images of Galfenol rolled sheet samples: before (left) and after (right) tension at 300°C.

Figure 33 shows the IPF image from half-dog bone sample that underwent anneal at 1000°C for 1 hour. No texture or grain size variation was observed at the gauge section. However, interestingly, a small region of abnormally grown Goss-texture was observed near the pinhole region with slightly elongated and plastically deformed.

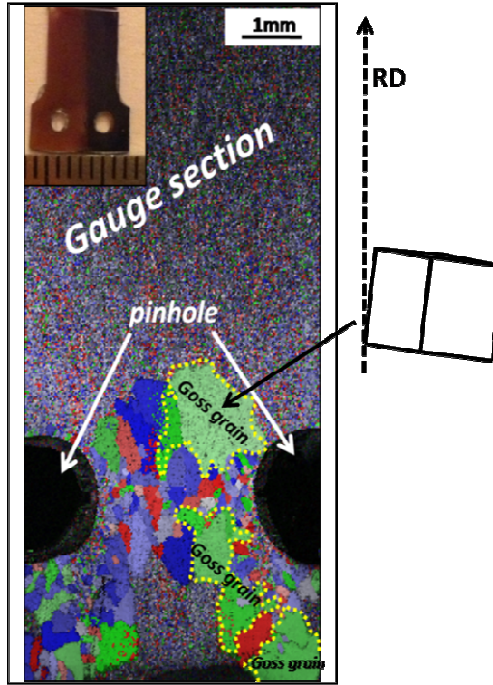


Figure 33 IPF image of a Galfenol sample annealed at 1000°C for 1 hour after imposing a 5×10^{-4} /s displacement rate controlled tension force. Grain growth occurred near the pin hole region and the abnormally grown Goss grains were tilted about 7° along the rolling direction.

The maximum size of abnormally grown Goss grain is 1400μm diameter and it is tilted about 7° from the rolling direction (RD). Stress was concentrated around the pinhole region with small amount of deformation during tensioning the sample and the influence of stored strain energy on AGG was verified indirectly in this region. To determine the critical strain needed to produce deformation energy effect on AGG, tapered samples were strain-annealed and studied next.

5.3 Strain Annealing with Tapered Sample

5.3.1 Sample Preparation and Experimental Procedure

Several dog bone samples with a 5% tapered and 3.3 inch long gauge section were obtained from as-rolled Galfenol samples that have same history with preliminary strain annealed samples as shown in Figure 34. The taper was designed at the gauge section to investigate the effect of different strain rates and strain on AGG with a single sample.

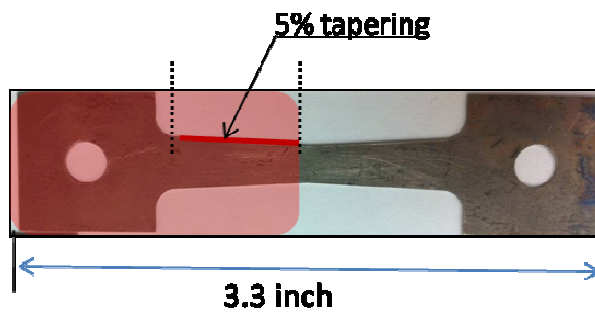


Figure 34 Tapered dog-bone Galfenol sample with 5% tapering and 3.3 inch long.

Figure 35 shows the schematic diagram that briefly explains the strain annealing procedure. First, the tapered dog bone samples were pre-annealed at 850°C for 15 hours under Ar atmosphere to make homogeneously recrystallized samples without any stored deformation energy due to rolling. Then, the samples were tensioned with a Materials Test System (MTS) (Figure 36) at a temperature of 200°C, 500°C and a constant displacement rate of $1 \times 10^{-4}/s$ and $5 \times 10^{-4}/s$ until the sample fractured. Finally, fractured samples were annealed under Ar atmosphere at different temperatures of 900°C, 1000°C and 1100°C for up to 3 hours.

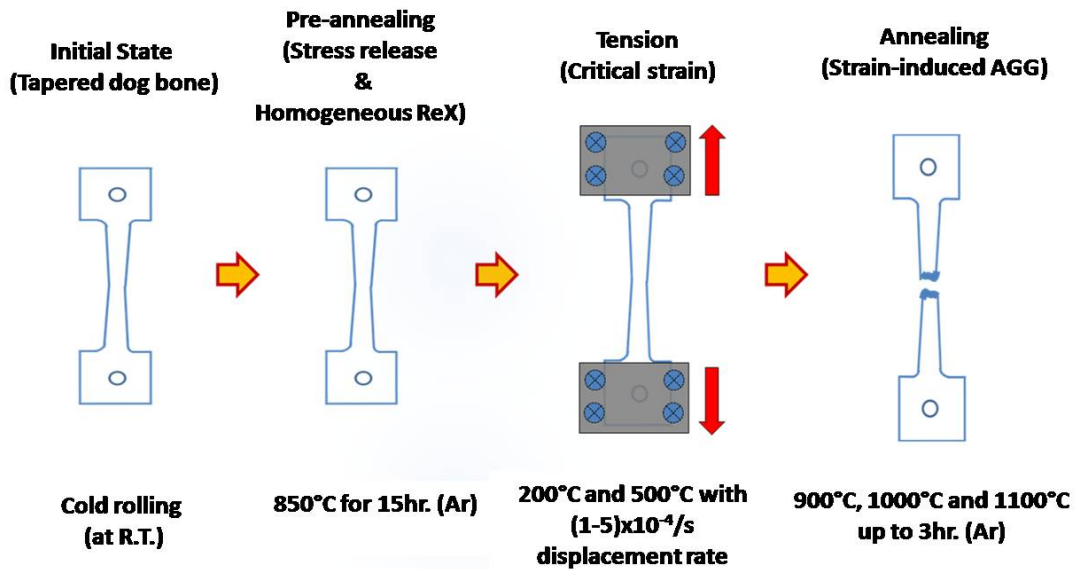


Figure 35 Overall experimental procedure of strain annealing process.

step1) Initial tapered dog bone sample by cold rolling, step 2) Pre-annealing at 850°C for 15hr under Ar for stress release and homogeneous recrystallization, step3) Tension at 200°C and 500°C with different displacement rate control to obtain critical strain for grain growth, step4) Annealing at 900°C, 1000°C and 1100°C up to 3hr. under Ar to observe strain-induced grain growth.

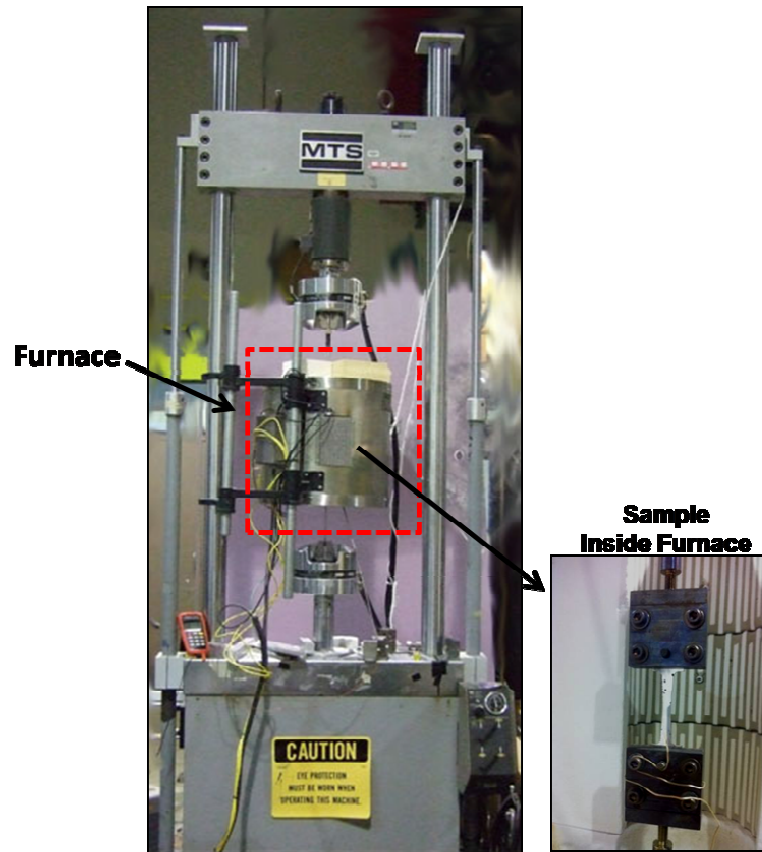


Figure 36 Photograph of MTS machine for tension which is designed to elevate tensioning temperature up to around 900°C.

Table 7 shows the summary of strain annealing in this study. Total five samples were tensioned at different tensioning temperature with different displacement rate control and nine fractured samples were strain annealed at different annealing temperature for different annealing time.

Table 7 Summary of samples for strain annealing

Samples	Tensioning Temperature (°C)	Displacement Rate (/s)	Annealing Temperature(°C)	Annealing time (min.)
Sample 1	200	5×10^{-4}	1000	120
Sample 2	200	5×10^{-4}	1000	180
Sample 3	200	5×10^{-4}	1050	900
Sample 4	500	1×10^{-4}	900	180
Sample 5	500	1×10^{-4}	1000	15
Sample 6	500	1×10^{-4}	1000	30
Sample 7	500	1×10^{-4}	1000	180
Sample 8	500	1×10^{-4}	1100	180
Sample 9	500	1×10^{-4}	1100	180

5.3.2 Results

5.3.2.1 Pre-annealed Sample before Tension

First, the IPF from the 850°C pre-annealed sample was obtained as shown in Figure 37. The whole section of the sample was recrystallized with randomly oriented distribution, and the average grain size diameter was around 67 μm , that is about 6.5 times larger than the average grain size in the pre annealed sample shown in Figure 31.

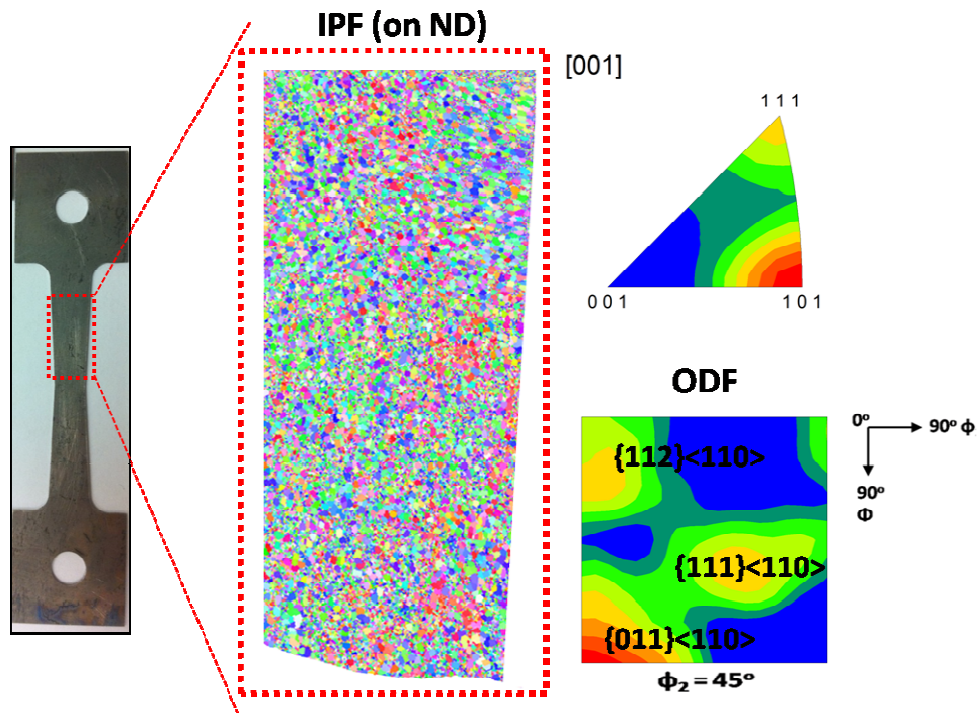


Figure 37 IPF and ODF plots of pre-annealed sample at 850°C for 15 hr. showing primary recrystallization with a randomly oriented distribution. Average grain size is ~67 μm .

It has been demonstrated many times that the orientations of large grown grains are not random,¹⁰⁶ but the link with the original texture is not yet clear. In order to control the final orientations of the grains, it is thus essential to investigate the textural evolution during the whole process in more detail. Also, it is reported that the critical strain value to be applied is largely determined by the prior microstructure¹⁰⁹ as shown in Figure 38. According to Figure 38, the critical strain decreases as a grain size increases, however, over at least 2% strain is considered necessary, irrespective of grain size.

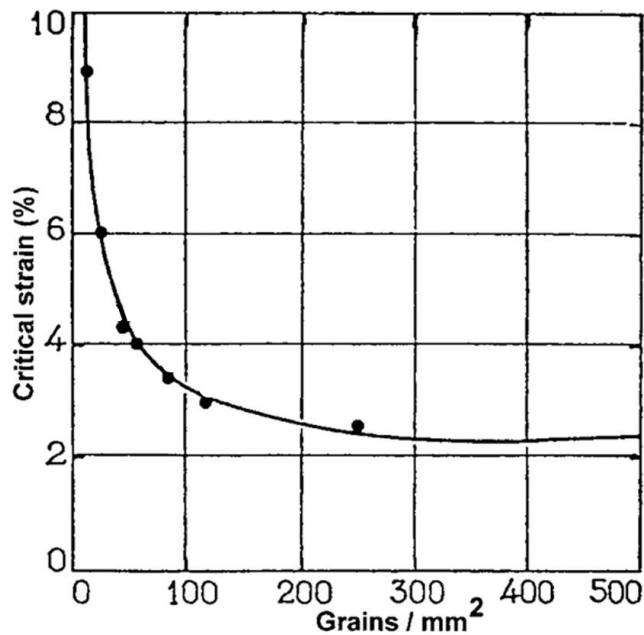


Figure 38 The effect of the initial grain size on the value of the critical strain.

(image from Kochendorfer (109))

5.3.2.2 Tension at Different Conditions

Depending on tensioning conditions, different fracture modes were observed as shown in Figure 39. The fracture of the sample 1 occurred right after the critical strength point (ultimate tensile strength) with a brittle fracture mode. The temperature was increased up to 200°C and then tensile stress was applied to the sample under constant displacement rate of 5×10^{-4} /s until the sample fractured. Very little plastic deformation occurred at the fractured site, and some orange peel like structure¹¹⁰ was observed on nearly the whole gauge section of the sample, indicating that the tensile stress propagated through the whole gauge section although it does not create visible plastic deformation. In this case, the estimated deformation energy stored in the sample was about 16MPa. This deformation energy was estimated based on the graph as shown in Figure 39.

Sample 4 was tensioned at a higher temperature of 500°C with a slower displacement rate of 1×10^{-4} /s. It took about 32 hours for the sample to fracture. In the case of sample 4, the critical strength became much lower than in sample 1, as about 500MPa and some thermal fluctuation was observed during the tension test. It is reported that more energy is absorbed inside the sample after changing the fracture mode from brittle to ductile in BCC materials.¹¹¹ It was estimated that the deformation energy stored inside sample 4 was 410MPa.

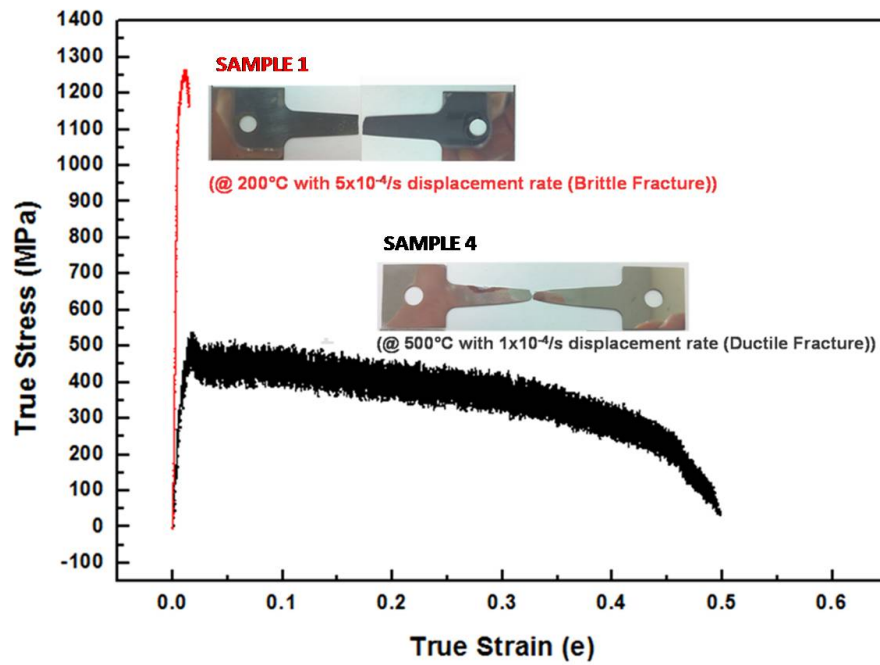


Figure 39 Stress and strain curve of brittle (sample 1) and ductile (sample 4) fractured Galfenol rolled sheet samples at different conditions. Sample 1) tensioning at 200°C with 5×10^{-4} /s displacement rate, Sample 4) tensioning at 500°C with 1×10^{-4} /s displacement rate)

5.3.2.3 Texture Analysis

5.3.2.3.1 Brittle Fractured Sample

EBSD patterns of two brittle fracture samples were captured and analyzed using OIM software to obtain IPF as shown in Figure 40.

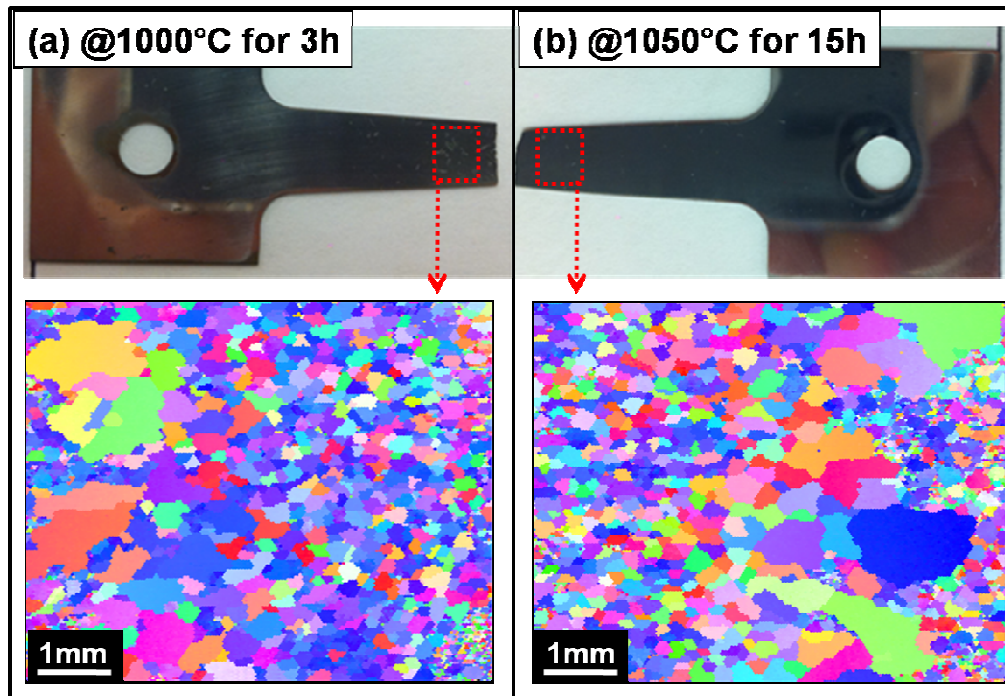


Figure 40 Optical and partial IPF images of brittle fractures in Galfenol rolled sheet samples (a) annealing at 1000°C for 3hours, and (b) annealing at 1050°C for 15 hours.

Figure 40(a) shows the IPF from a small region of brittle fractured sample that was annealed at 1000°C for 3 hours. Not much grain growth was observed in the gauge section. Only partial grain growth was observed near the fracture site. This indicates that the tensile stress applied to brittle fractured sample, which did not result in plastic deformation, did not significantly influence grain growth. Similarly, partial grain growth was observed in a similar region from the other half of the dog bone after higher temperature annealing at 1050°C for 15 hours, as shown in Figure 40(b). It is suggested that thermal energy resulting from 1000°C-1050°C annealing provides the driving force for nucleation and primary recrystallization, however, this range of thermal energy is insufficient for grain growth. Also it indicates brittle fracture prevented the critical strain necessary for large grain growth during anneal at this range of temperatures, from being achieved. Fundamentally, a deficient amount of strain energy in the brittle fractured samples caused this result.

5.3.2.3.2 Ductile Fractured Sample

Figure 41 shows the IPF images from ductile fractured samples that were annealed at 900°C, 1000°C and 1100°C for 3 hours, respectively.

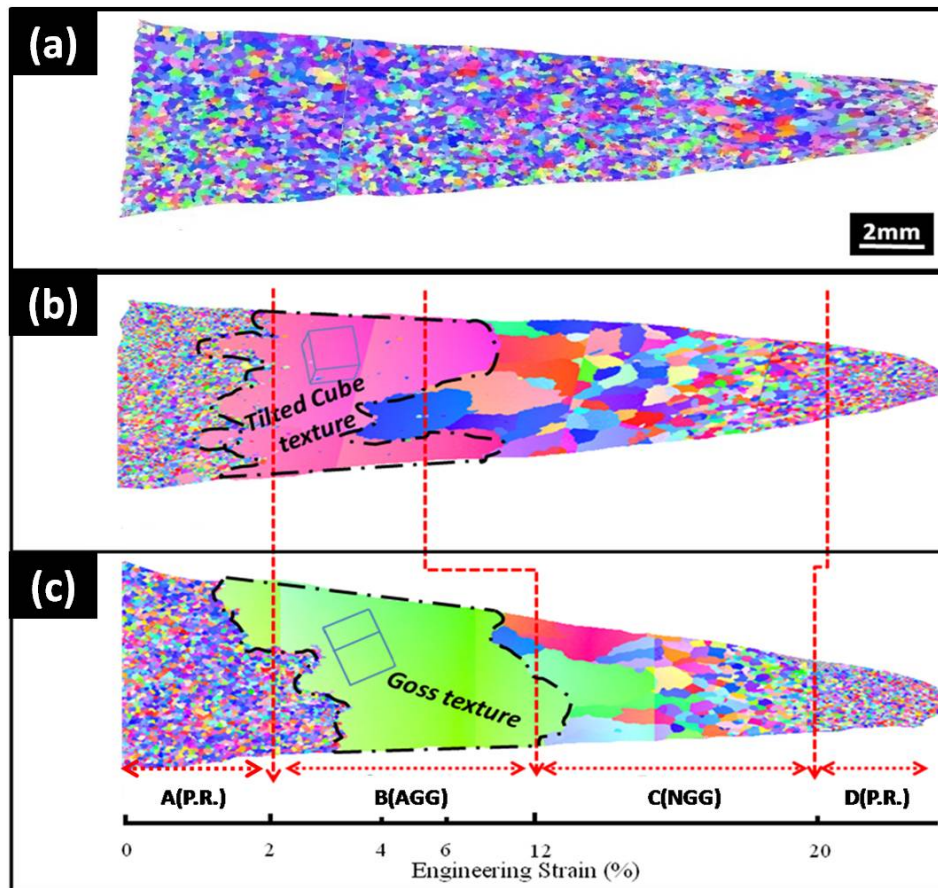


Figure 41 IPF images of strain annealed ductile fractured Galfenol rolled sheet samples (a) annealing at 900°C for 3hours, (b) annealing at 1000°C for 3hours, and (c) annealing at 1100°C for 3hours under Ar atmosphere.

(*P.R. : Primary Recrystallization)

Different types of recrystallization were observed in the ductile fractured samples than in the recrystallized brittle fractured samples. No grain growth was observed from the sample that annealed at 900°C for 3hours as shown in Figure 41(a). Significant and various grain growth was observed in the ductile fractured samples (Figure 41 (b) and (c)) irrespective of the final annealing temperatures of 1000°C and 1100°C. A similar gradient in grain size is evident within

the gauge section of both samples. Also, the stored deformation energies inside two different samples are similar due to their well matched deformed length and width after tension. However, two different anneal temperatures lead to two different strain-induced, abnormally grown textures at the location of similar critical strain. A tilted Cube grain is abnormally grown in the sample annealed at 1000°C as shown in Figure 41(b), and a tilted Goss grain is abnormally grown in the sample annealed at 1100°C as shown in Figure 41(c). Interestingly, no grain growth was observed at both ends of the gauge section. This indicates that the grain growth is not affected by too much or too little deformation. The region of strain-induced tilted Cube textured AGG in Figure 41(b) underwent engineering straining of 2-6%. In Figure 41(c), the region of strain-induced tilted Goss textured AGG underwent engineering straining of 3-12%. It is suggested that the higher annealing temperature may have combined with the strain in regions of 7-12% engineering strain that facilitated AGG in these regions of the sample as both samples contained the same stored deformation energy. This common critical strain region for AGG in Galfenol of 3-6% is relatively well matched with the region for α -iron, where 2-5% engineering strain lead to AGG of an unspecified texture and RENE 88 Ni-base super alloy, where 2-4% engineering strain lead to AGG of an unspecified texture.^{112,113} The strain annealed sample in Figure 41(c) has the larger critical strain range for strain-induced AGG than the other materials in the above references. Region A is primarily a recrystallization region that occurred during previous pre-anneal at 850°C for 15 hours. Less than 2% deformation from tension does not affect extended grain growth due to insufficient deformation energy for boundary migration. The grain size difference of region B, C and D in Figure 41 is coincident with one of the laws of recrystallization that was mentioned in chapter 2.4.1.1. *“The recrystallized grain size depends primarily on the amount of deformation, being smaller for large amounts of deformation.”* The

grain size is smaller as it moves to the fractured site from B to D. It is possible that higher strain regions provide more nucleation sites per unit volume and ultimately develop into smaller grain size. The strain-induced AGG region (region B) in Figure 41 (b) and (c) has been deformed less than regions C and D, which suggests that strain-induced AGG in region B is much more dominated by grain growth associated with grain boundary migration rather than by nucleation for primary recrystallization. In addition to verifying the critical strain for AGG, the critical strain rate of region B for AGG is verified as $10^{-5}/s$.

Table 8 shows the summarization of different grain growth modes at different regions of each sample with different fractures and annealing histories. Any AGG phenomena were observed from brittle fractured samples. Commonly, AGG phenomena were observed from 2-6% engineering strain region from ductile fractured sample, and wider AGG were investigated from 1100°C annealing process.

Table 8 Different grain growth mode at different Engineering strain

- Only partial grain growth occurred from the brittle fractured sample
- No grain growth occurred from the ductile fractured sample that annealed at 900°C
- Tilted Cube-textured AGG occurred from the ductile fractured sample that annealed at 1000°C in the range of 2-6% engineering strain.
- Goss-textured AGG occurred from the ductile fractured sample that annealed at 1100°C in the range of 2-12% engineering strain.

		Engineering Strain (%)				
		0 - 2	2 - 6	6 - 12	12 - 20	> 20
Fracture mode & Annealing Temp. (°C)						
	Brittle	1000	.	.	PGG	.
1050		.	.	PGG	.	.
Ductile	900	P.R.	P.R.	P.R.	P.R.	P.R.
	1000	P.R.	AGG (Tilted Cube)	NGG (Large size)	NGG (Small size)	P.R.
	1100	P.R.	AGG (Goss)	AGG (Goss)	NGG (Large & Small size)	P.R.

(* PGG: Partial grain growth
 AGG: Abnormal grain growth
 NGG: Normal grain growth
 P.R.: Primary recrystallization)

To observe the sequential grain growth modes, we annealed the fractured samples at 1000°C for less than 3 hours as shown in Figure 42. It is observed that the NGG and primary recrystallization in regions C and D are produced first in the early stage of annealing process after an anneal of only 15 minutes. Alternatively, tilted Cube textured AGG in region B occurred gradually compared to other grain growth in regions C and D. It is observed that the few tilted

Cube textured crystals, which formed during a 15 minute annealing process in region B (Figure 42(b)), combine together little by little and then develop into one large abnormally grown tilted-Cube grain (Figure 42(d)). Also, it seems that the abnormally grown texture in region B is roughly determined in an early stage of annealing process, as early as after only 15 minutes, and after 30 minutes, develops further in the direction of less deformed sites (i.e. region of lower strain).

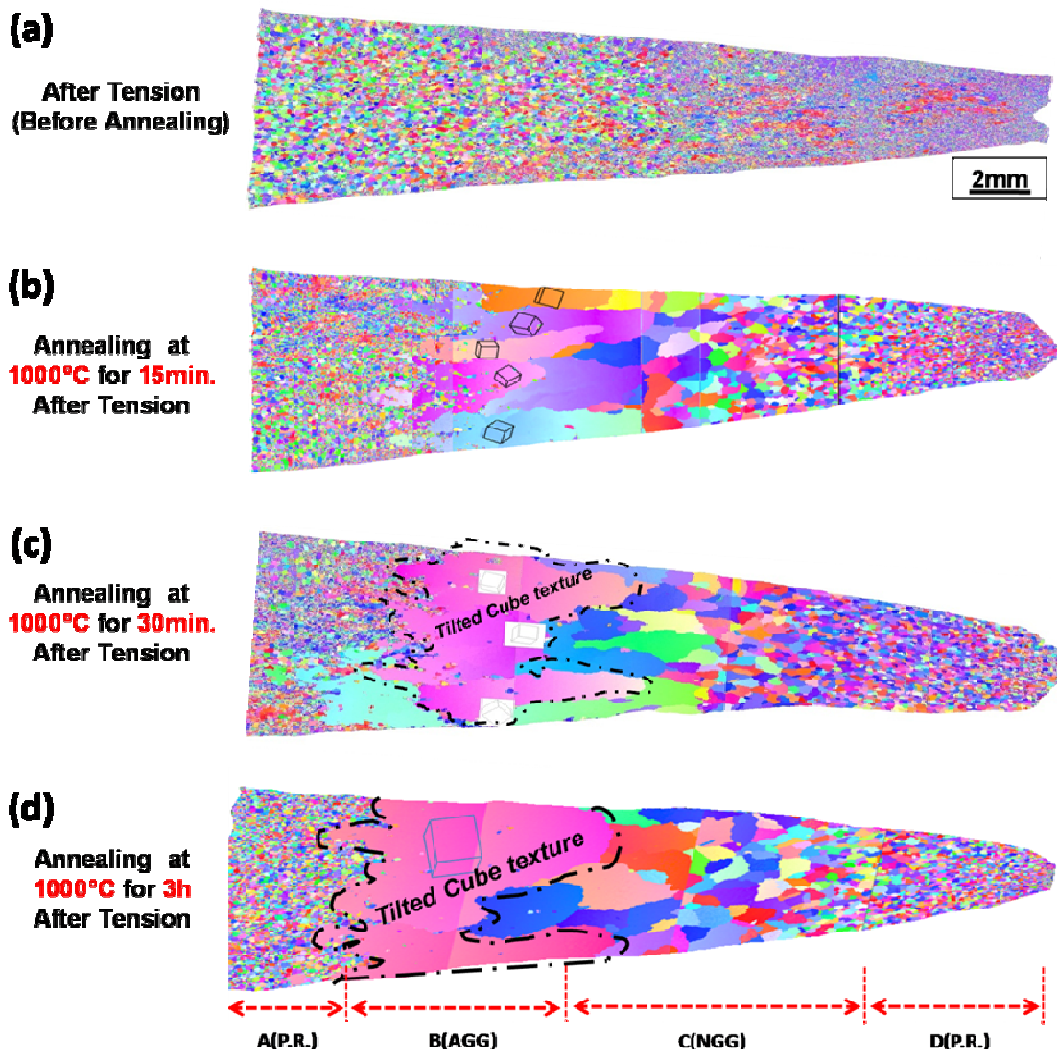


Figure 42 IPF images of different annealing time at 1000°C (a) as-tensioned Galfenol rolled sheet sample, (b) annealing for 15 minutes, (c) annealing for 30 minutes, and (d) annealing for 3 hours.

The number of small size of island grains, inside the abnormally grown grain in region B, decreased as annealing time increased (Figure 43). This figure shows the highly magnified IPF images of region B for 15min., 30min. and 3hr.. The area fraction of small island grains with the size of under 200 μm diameter decreases as the annealing time increases. The area fraction of island grains in a 15 minute annealed sample is 26.28%, however, the area fractions of island grains in 30 minute and 3 hour annealed samples are 8.61% and 2.79%, respectively.

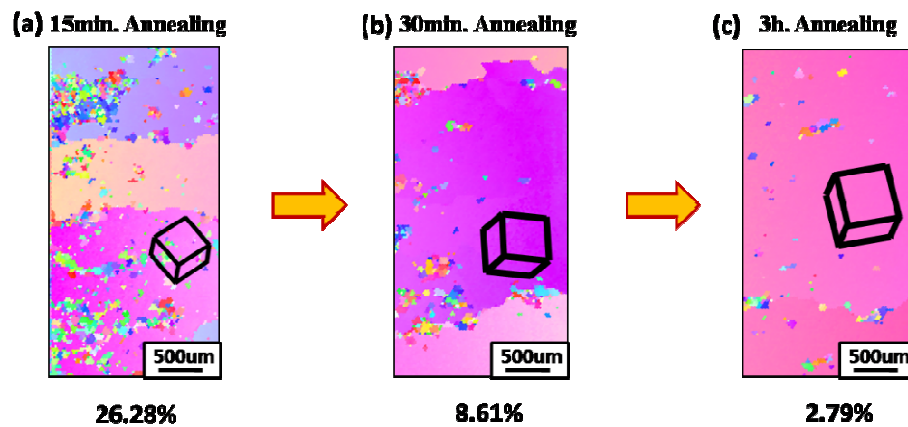


Figure 43 High magnified IPF images of region B in Figure 42 and different area fraction of small island grains with the size of under 200 μm diameter.

(a) area fraction of island grains is 26.28%, (b) area fraction of island grains is 8.61% and (c) area fraction of island grains is 2.79%.

To know the origin of AGG and other grain growth modes, as-tensioned Galfenol rolled samples were investigated in detail. Figure 44 shows the high magnified IPF images of different regions, and grain size variation from each region. As mentioned in chapter 2, it was expected

that the initial grain size and misorientation distribution just after the tension test would affect the different grain growth modes produced as a result of an annealing process.

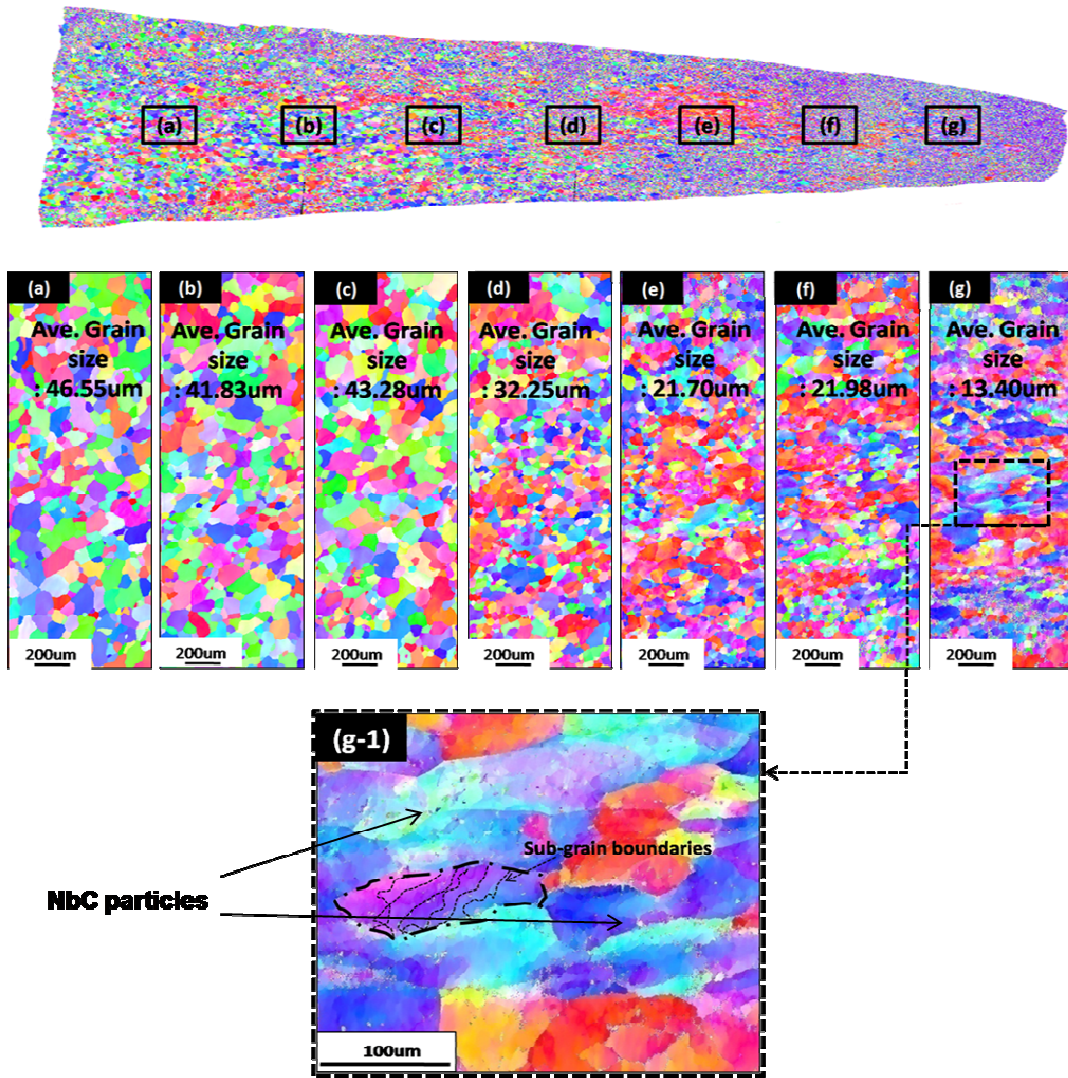


Figure 44 High magnified IPF images of as-tensioned Galfenol rolled sheet sample. From region (a) to (g): grain size decreases gradually, (g-1): many sub-grain boundaries inside each grain.

At region (a), the average grain size is 46.55 μm diameter, and the grain size at region (g) is 13.4 μm diameter. The grain size in region (a) is 3.5 times larger than the one in region (g). The region (g) was subjected to much more deformation with a faster strain rate during tension at constant displacement rate as 1×10^{-4} /s of MTS test. Many sub-grain boundaries can be observed in Figure 44(g-1), and this provides more nucleation sites for recrystallization during the annealing process. In other words, each region contains a different number of nucleation sites, leading to different recrystallization. Figure 44 contains several supporting ideas to study the law of recrystallization. Additionally, lots of NbC particles of 1-3 μm size that affect AGG are randomly distributed on the whole surface as shown in Figure 44(g-1).

Each region of the as-tensioned sample has different crystal orientation. Figure 45 shows IPF and ODF plots of different region (a), (d) and (g) in as-tensioned sample, respectively. The $\{112\}\langle 110 \rangle$ texture is dominant in region (a), and this dominant texture is similar with the texture from the pre-annealed sample as shown in Figure 37. The main texture in region (a) is altered along the length of the sample due to the different deformations and strain rates introduced during tension. $\{001\}$ is dominant at the center of the gauge section (Region d) and $\{111\}$ is dominant close to the fractured site (Region g). It is suggested that this high fraction of $\{100\}$ grains at the center could be resulted from SIBM mechanism that will be explained in the following section 5.3.3.

Also, Figure 45 shows the different misorientation angle distributions in regions (a), (d) and (g). Normal misorientation distribution is observed in region (a) that is typical of a sample with randomly orientated distribution. A relatively high fraction of low angle misorientation, around 41%, is observed in region (g). This high fraction of low angle misorientation supports the presence of sub-grain boundaries that is shown in Figure 44 (g-1). Constant misorientation

distribution is shown in region (d), which is close to the beginning point of AGG region B in Figure 41 and Figure 42. It is possible that constant misorientation distribution in region (d) influences the different grain growth mode and contributes to AGG during high temperature annealing. To better understand this, further study of texture development due to different misorientation distributions should be undertaken.

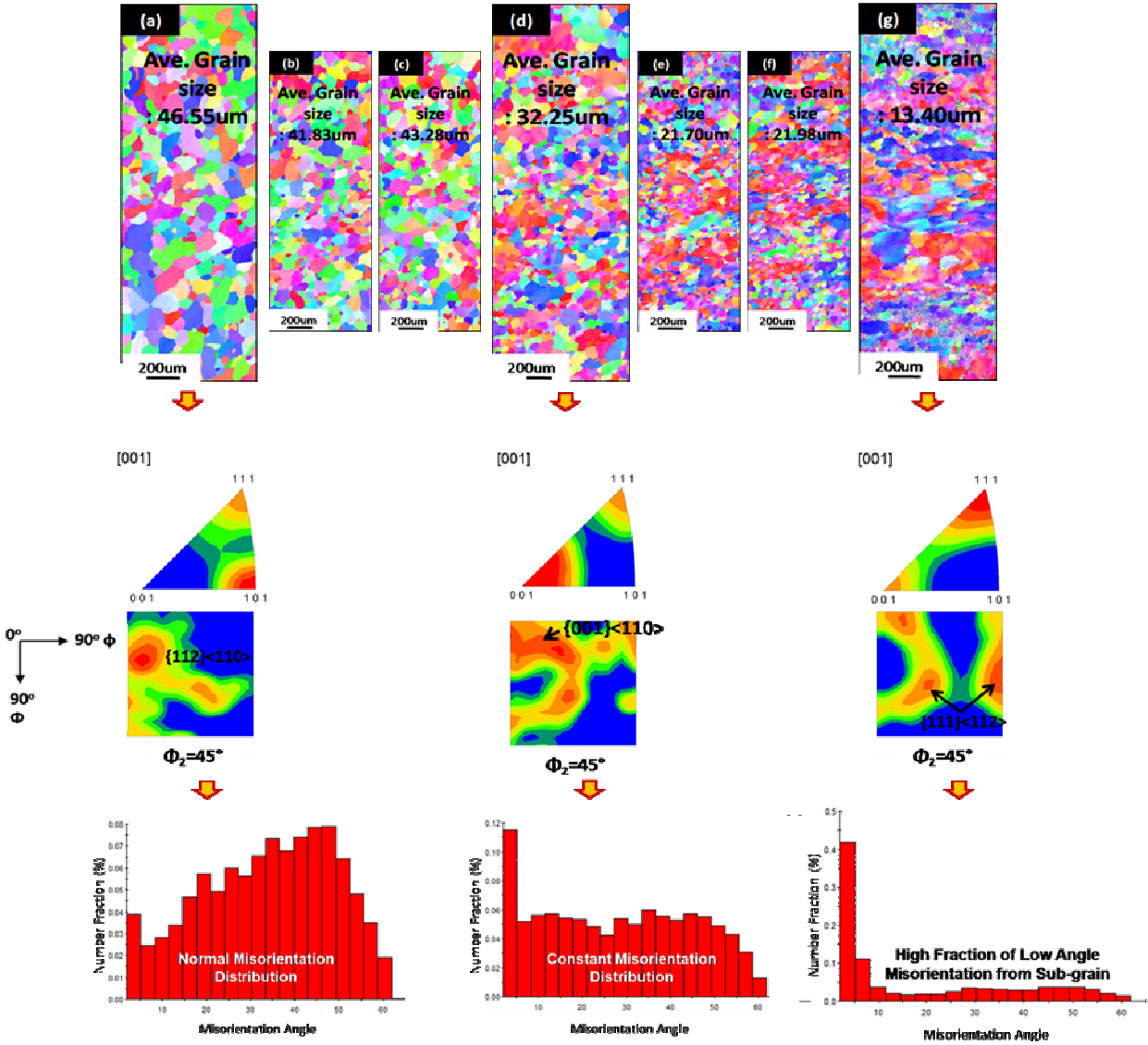
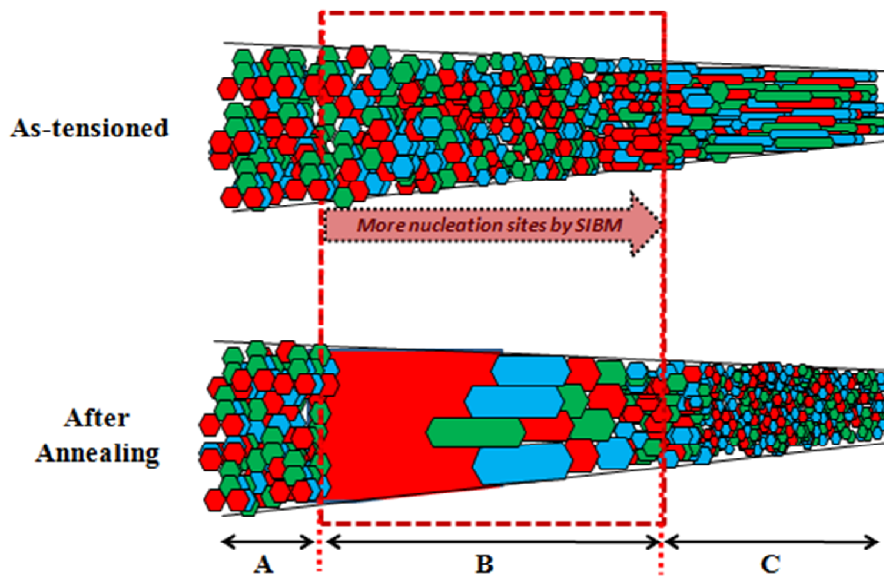


Figure 45 IPF images, ODF plots, and misorientation distributions at different regions of as-tensioned Galfenol rolled sheet sample.

5.3.3 Mechanism for AGG by Strain Annealing with tapered sample

Figure 46 shows a possible mechanism for different grain growth in region B than in the rest of the sample. Region B in Figure 46 is coincident with the region B and C in Figure 42 that consists of AGG and NGG. Region B in Figure 46 is the effective region for SIBM by tension, with creation of more nucleation sites by SIBM to the right side of the box. More nucleation sites by SIBM (right side of region B) would enhance the formation of NGG and relatively small nucleation sites by SIBM (left side of region B) will enhance the formation of AGG during high temperature annealing.



* Dotted line box B: SIBM effective region (Region B and C in Figure 46)

Figure 46 Schematic diagram on the effect of SIBM on different grain growth modes of regions B and C in Figure 42.

Thus, thermal energy concentrates on a few nucleation sites by SIBM and it accelerates the AGG in region A and thermal energy concentrates on more nucleation sites by SIBM and it promotes

the NGG in region B. However, too many nucleation sites in region C promote primary recrystallization in the same manner as the primary recrystallization phenomena that occurs after normal rolling process that introduce significant deformation.

As shown in Figure 41, tilted Cube-textured AGG occurred when the samples were annealed at 1000°C and Goss-textured AGG occurred when the samples were annealed at 1100°C. Why were different kind of grains are abnormally grown during high temperature strain anneal process at temperatures of 1000°C and 1100°C? It is theorized that this is influenced by that the (100) plane has the highest packing density and (110) plane has the lowest packing density in bcc simple cubic Galfenol. The surface energies of arbitrary orientation crystal planes of several metals are calculated with the broken-bond model in reference 114. The bonds of the nearest neighbor and second neighbor are considered, and the ratio of the second neighbor bond energy to the nearest bond energy is calculated. The ratio of bcc metal is larger than that of fcc metal and the surface energy of (100), (111) and (110) in α -Fe was 2.6660 J/m², 2.5271 J/m², and 2.0535 J/m², respectively.¹¹⁴ It can be considered that the atomic density of (100) plane of α -Fe is higher than the one of other planes of (111) and (110) in α -Fe. Galfenol has very similar crystal structure with α -Fe. Thus it can be considered that relatively more number of dislocation free (100) grains nucleated at the interface between (100) and (110) or between (100) and (111) caused by SIBM mechanism than other grains of (111) and/or (110) as shown in Figure 47.

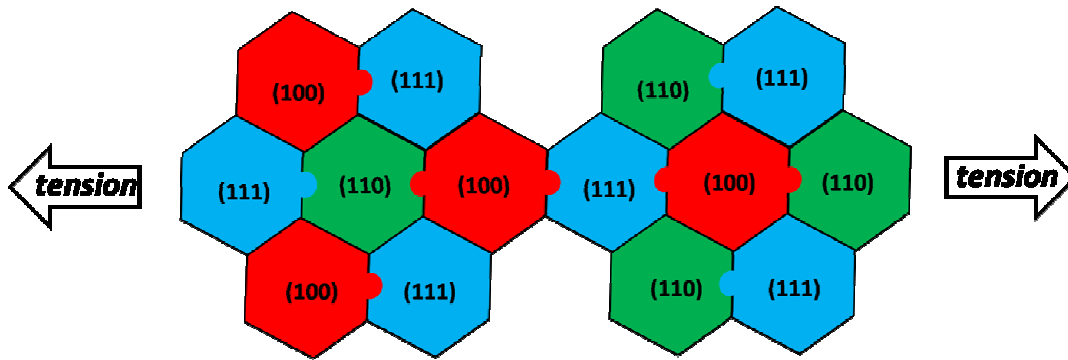


Figure 47 Schematic diagram of nucleation through SIBM mechanism during tension test at 500°C.

As shown in Figure 47, when the sample is tensioned with “constant strain rate” of $10^{-5}/s$ and “critical strain” around 2-6% at 500°C, more dislocation free (100) grains are nucleated at the interface due to this SIBM mechanism. The IPF in Figure 45 (d) supports this hypothesis on an increase in the fractional area of (100) grains as a result of the SIBM mechanism. The prevailing orientation in region (d) is (100) and a relatively small portion of (110) grains are shown in this region. Nucleated (100) grains in region (d) grow preferentially at 1000°C annealing process and they form abnormally large tilted Cube-textured grain after prolonged annealing process. 1000°C adds enough thermal to get the nucleated (100) grains to grow abnormally, but does not trigger the dominance of surface energy. At 1100°C, i.e. a slightly higher annealing temperature, there is enough more thermal energy to promote AGG of (110) Goss-textured grains. Thus the (110) grains grow faster than other grains. 1100°C adds enough thermal energy that the surface energy is dominant. Goss-textured AGG was also observed at 1100°C and 1200°C annealing under Ar atmosphere without strain in reference 4 and 82.

5.3.4 Summary on Tapered Strain Annealed Samples with Brittle and Ductile Fracture Mode

Figure 48 shows the summary of the extent of primary recrystallization, NGG and AGG from the tapered strain annealed samples with brittle and ductile fractured samples.

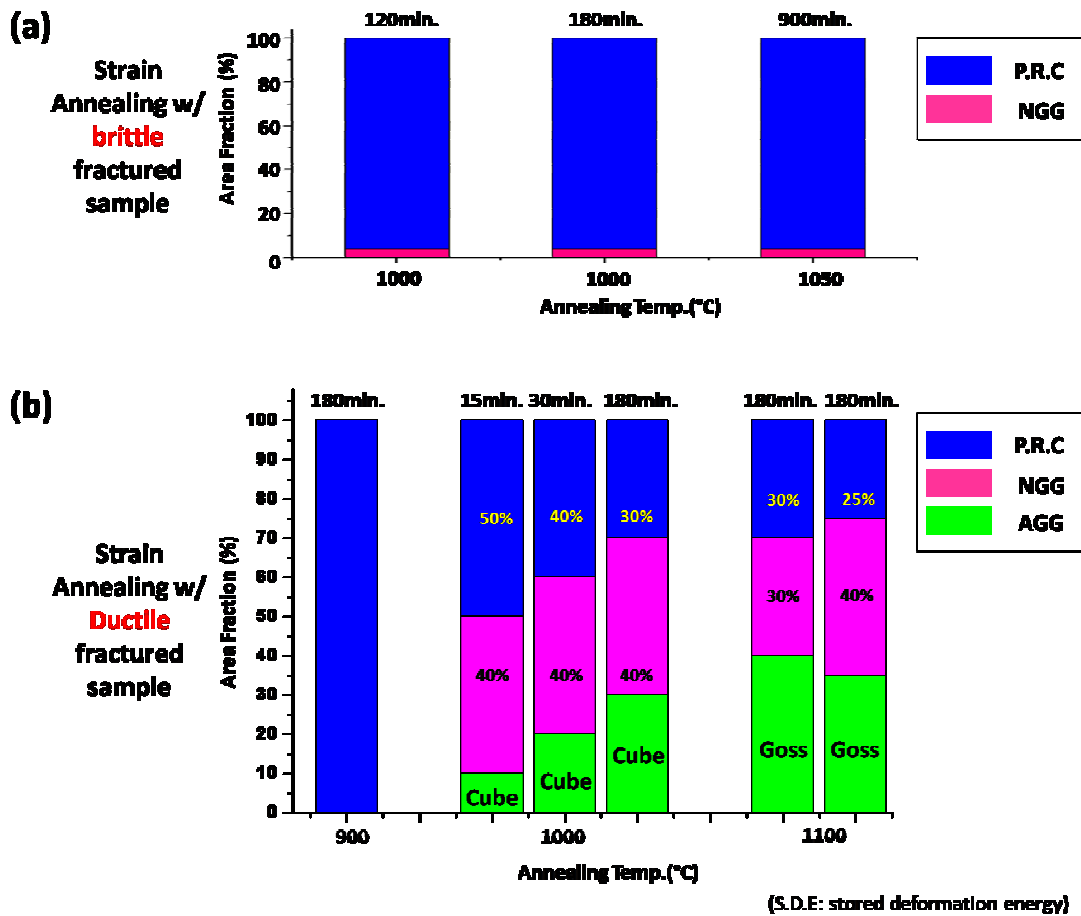


Figure 48 Summary of tapered strain annealed samples with (a) brittle and (b) ductile fracture modes. (a) Small fraction of NGG was occurred from the brittle fractured dog bone samples that annealed at 1000°C and 1050°C, (b) primary recrystallization was occurred from the ductile fractured sample that annealed at 900°C and tilted-Cube and Goss-textured AGG were occurred from ductile fractured samples that annealed at 1000°C and 1100°C, respectively.

Only a few percent of the area fraction of the strain annealed samples that failed in a brittle fracture mode exhibited NGG regardless of annealing time and temperature at 1000°C and 1050°C as shown in Figure 48 (a). Any NGG that occurred was in the region near the fracture site. In this case the overall stored deformation energy by tension was 16MPa and this amount of stored deformation energy was too small to grain growth at these annealing temperature.

Various grain growth modes were observed from strain annealed sample with ductile fracture mode as shown in Figure 48 (b). For 900°C strain annealing, no grain growth was observed and only primary recrystallization occurred. Tilted Cube-textured AGG occurred during strain annealing at 1000°C and the Goss-textured AGG occurred during strain annealing at 1100°C. The overall stored deformation energy for various grain growth was around 410MPa and this amount of energy was enough large to decrease the annealing temperature for grain growth and to provide significantly different results that for anneal with no tension under Ar for 3hr. as shown in Figure 49.

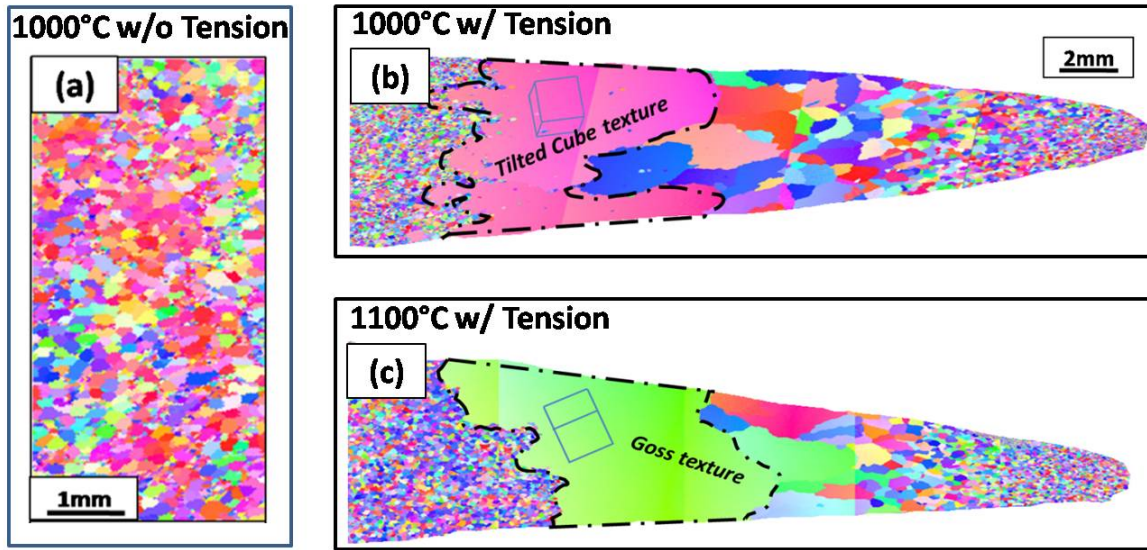


Figure 49. Deformation energy and strain effects for grain growth

(a) Occurrence of primary recrystallization after annealing at 1000°C under Ar without tension, (b) Tilted cube-textured AGG and NGG after annealing at 1000°C under Ar with tension, and (c) Goss-textured AGG and NGG after annealing at 1100°C under Ar with tension.

Thus, the deformation energy and strain effects on different grain growth phenomena by strain annealing process with tapered samples were understood in this chapter.

5.4 Strain Annealing with Uniform Sample

Based on the results from chapter 5.3, the strain annealing with uniformed dog-bone shape of Galfenol rolled sheet samples were investigated. The uniformed dog-bone samples were pre-annealed at 850°C for 15 hours under Ar atmosphere to make homogeneously recrystallized samples without any stored deformation energy due to rolling. Then, the samples were tensioned with a Materials Test System (MTS) (Figure 36) at a temperature of 500°C and a constant displacement rate of $1 \times (10^{-5}-10^{-4})/s$ until the sample elongated with 3% engineering strain. These conditions were selected because AGG of tilted Cube and Goss texture were observed at the region of 3% engineering strain shown in Table 8 in this chapter. The deformed samples were annealed at 1000°C for 1 and 3 hours under Ar atmosphere.

Figure 50 shows the optical image of tensioned sample with a constant displacement rate of $1 \times 10^{-4}/s$. The gauge section of the sample elongated with 3.3% engineering strain, however, the gauge section deformed with different engineering strain from region A, B and C, respectively. The regions A and C deformed with 1.7% engineering strain, and the center of the sample (region B) deformed with 3.2% engineering strain.

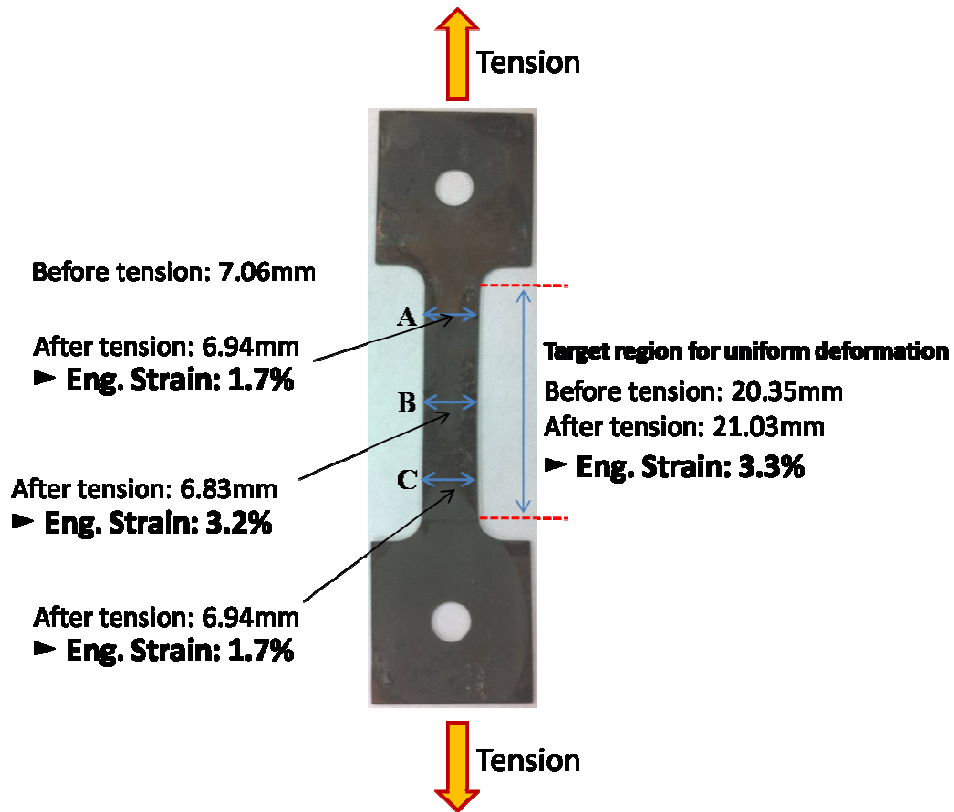


Figure 50 Optical images of as tensioned Galfenol rolled sheet sample with a constant displacement rate of 1×10^{-4} /s.

After annealing at 1000°C for 1 hour, NGG was observed only at the region of B and no grain growth phenomena was observed in region A and C. Figure 51(a) and (b) show the IPF images from region A and B after annealing. It is suggested that 1.7% engineering strain provides insufficient strain for grain growth at 1000°C annealing.

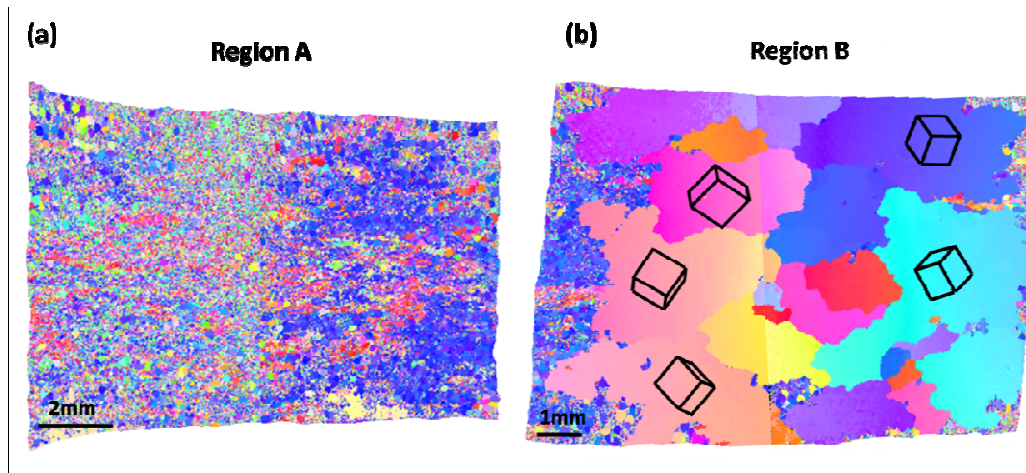


Figure 51 IPF images of Galfenol rolled sheet sample that annealed at 1000°C for 1 hour. (a) 1.7% engineering strain and primary recrystallization, (b) 3.2% engineering strain and NGG

Figure 52 shows the optical image of tensioned sample with a constant displacement rate of 1×10^{-5} /s. In this case, the gauge section of the sample uniformly elongated with 2.7% engineering strain.

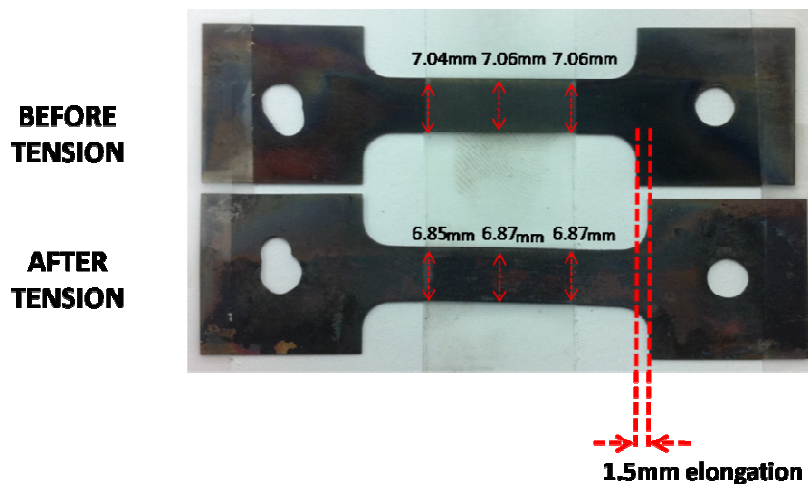


Figure 52 Optical images of as tensioned Galfenol rolled sheet sample with a constant displacement rate of 1×10^{-5} /s showing dimensions before and after tensioning of the sample.

After achieving uniformly elongated Galfenol sample with 2.7% engineering strain, the whole sample was annealed at 1000°C under Ar atmosphere for 3 hours. Figure 53 shows the IPF image of annealed sample. The NGG with 1mm average grain size diameter was observed along the whole gauge section. However, no AGG was observed in this sample. Thus an engineering strain of 2.7% was also out of range to produce AGG. In this case the overall stored deformation energy is about 68MPa. To investigate the AGG phenomena via unformed Galfenol rolled sheet sample, further study on the other conditions should be undertaken.

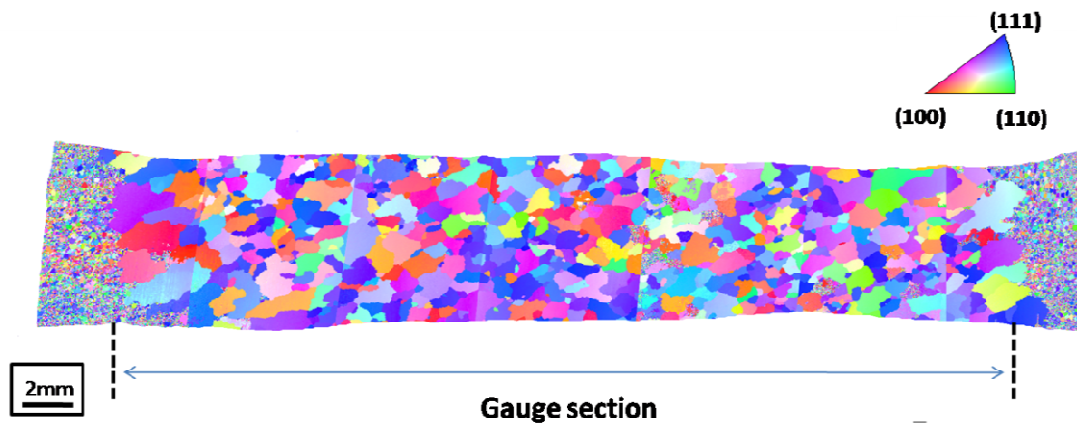


Figure 53 IPF image of unformed Galfenol rolled sheet sample with 2.7% engineering strain that annealed at 1000°C for 3 hours.

5.5 Conclusion

In conclusion, the strain annealing effect with the tapered and uniform dog bone samples was investigated in this chapter. Two different fracture modes were obtained after tension tests and then those samples were annealed at different temperatures. Only partial grain growth was observed in the brittle fractured sample that was tensioned at 200°C with a 5×10^{-4} /s displacement rate due to insufficient stored deformation energy as 16MPa and insufficient strain for promoting

grain growth. Tilted Cube and Goss-textured strain-induced AGG were observed in ductile fractured samples that were tensioned at 500°C with a 1×10^{-4} /s displacement rate. These AGG phenomena were observed at 1000°C and 1100°C annealing for 3hr., respectively. This is the contrast with anneal at 1200°C that is required for AGG in samples annealed under Ar that have not been strained. Deformation energy of 410MPa and 2-6% engineering strain activated grain boundary migration and decreased the annealing temperature needed for AGG to 1000°C. From different regions of the tapered samples, diverse grain growth modes were observed, including predominantly primary recrystallization, AGG and NGG. The optimal strain rate (10^{-5} /s) and critical strain (2-5% Eng. Strain) for AGG in tapered Galfenol rolled sheet were identified, however, these conditions did not work for AGG in uniform Galfenol rolled sheet samples.

Chapter 6: Ga loss during High Temperature Annealing Process

6.1 Introduction

Ga content affects magnetostrictive properties, thus it is important to have an optimal Ga content of 19mol.% after a high temperature annealing process. It is suggested that the Ga atoms evaporate through the grain boundaries during a high temperature annealing process through grain boundary diffusion. Grain boundaries contain large numbers of defects, such as individual vacancies and interstitials, and grain boundary diffusion can occur via these defects.¹¹⁵ At high temperature, the presence of large concentration of these defects severely affects atomic diffusion. Thus, the Ga loss during high temperature annealing at 1000°C, 1100°C and 1200°C was investigated using an electron probe microanalyzer (EPMA) analysis.

6.2 Result

6.2.1 Ga loss during High Temperature Annealing at 1200°C

The Ga loss during high temperature annealing at 1200°C was investigated via EPMA analysis. A one hundred point analysis was conducted on 12mm x 12mm x 0.45mm Galfenol rolled sheet samples with a spatial resolution of less than 1µm (0.001 mm) by EDX in EPMA. The samples were annealed for 2, 3 and 4 hours under Ar atmosphere. The IPF images of these samples are shown in Figure 21. The Ga content in the initial ingot was 18.81%, which was very

close to the targeted Ga content. This decreased by just 0.05% after the hot and warm rolling. Thus, the Ga content of the as-rolled sample was 18.76% Ga as shown in Figure 54(a). However Ga content decreased as the annealing time increased. At the initial annealing stage of 2 hours, the Ga content decreased by 1.74% (Figure 54(b)) from the one of as-rolled states. The decrease in Ga content continued with longer annealing processes, but at a slow rate. Less than approximately 0.6% and 0.07% additional Ga loss was observed in the 3 and 4 hour annealed sample, respectively. Thus the final Ga content in the 4 hour annealed sample was 16.33% as shown in Figure 54(d). This Ga loss phenomenon supports the theory that Ga evaporates through grain boundaries during high temperature annealing at 1200°C.

The changing rate of Ga loss can be explained by grain size differences with anneal duration. Fewer grain boundaries mean larger grain size in a specific area and make Ga evaporation through the grain boundaries during high temperature annealing more difficult. Conversely, more grain boundaries mean smaller grain size and make for easier Ga evaporation through the grain boundaries during high temperature annealing. In the 2 hour annealed sample, the average grain size diameter is 152.2 μm and the sample shows a greater rate of Ga loss than the 4 hour annealed sample which had a 540.9 μm average grain size diameter.

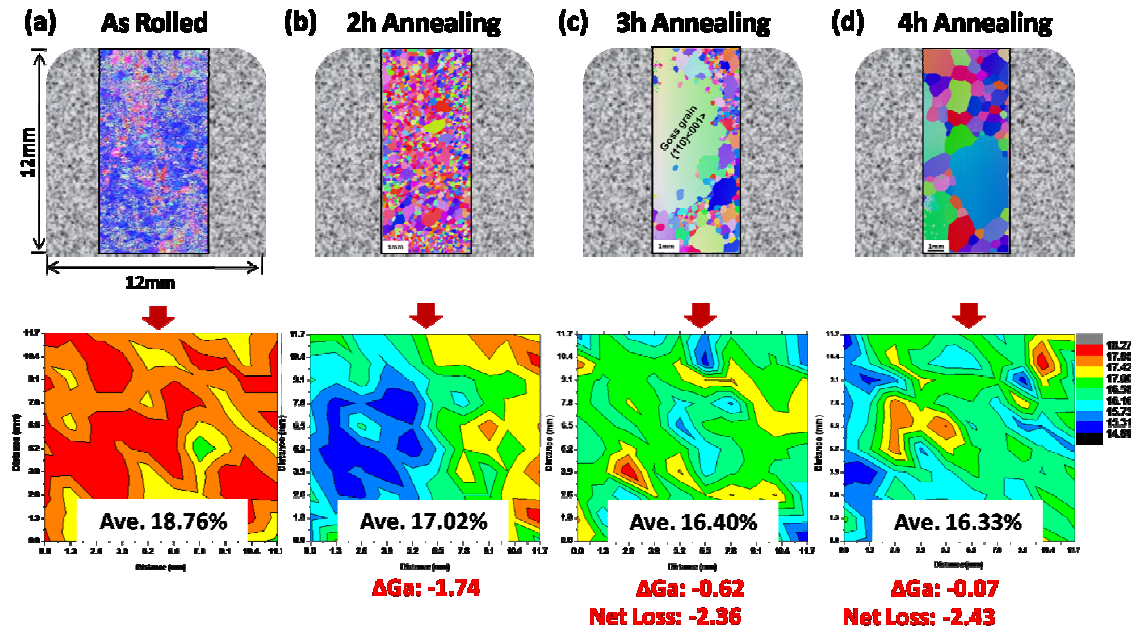


Figure 54 EPMA point analysis on Ga losses from Galfenol rolled sheet samples as a function of annealing time for 2, 3 and 4 hours at 1200°C under Ar atmosphere.

Figure 55 shows the rate of Ga loss as a function of annealing time. As shown in this graph, 2% Ga loss occurred at the initial stage of annealing process for 2 hours and less than 1% Ga loss occurred after 2 hour annealing process. For an average density of grain boundaries of 54/mm², Ga loss rate was about 0.87%Ga/hr. as shown in Figure 55. As number of grains decreased due to AGG, average density of grain boundaries decreased to 21/mm² and the rate of Ga loss was 0.53%Ga/hr. Finally, as number of grains decreased due to NGG, average density of grain boundaries decreased to 6/mm² and the rate of Ga loss was 0.16%Ga/hr. Thus we need to be aware of Ga evaporation, which deteriorates magnetostrictive performance, especially in the early stage of high temperature annealing process at 1200°C.

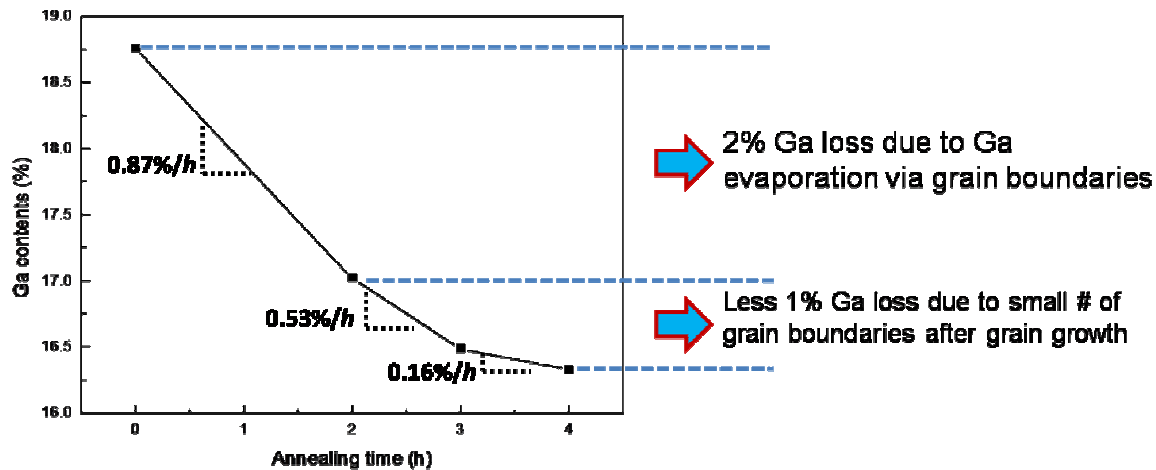


Figure 55 The rate of Ga loss in Galfenol rolled sheet samples as a function of annealing time at 1200°C under Ar atmosphere.

6.2.2 Ga loss during Strain Annealing at 1000°C & 1100°C

Ga loss during strain annealing at 1000°C and 1100°C was investigated by EPMA analysis as shown in Figure 56. A fifty point analysis was conducted the region between A and B. No Ga loss was observed in the 1000°C annealing process, irrespective of annealing time. However, significant Ga loss was observed from the 1100°C annealed sample, especially near the fractured site, labeled B. The average Ga composition in the 1100°C annealed sample was 16.28% which is about 2% lower than in the samples that were annealed at 1000°C, and the minimum Ga composition at fractured site B was 9.7%. This Ga composition is notably lower than the average Ga composition of the 1000°C annealed sample. It shows that a large amount of Ga evaporated during the primary recrystallization phenomena at 1100°C through many sub-grain boundaries, caused by tension, in the region close to the fractured site (point B).

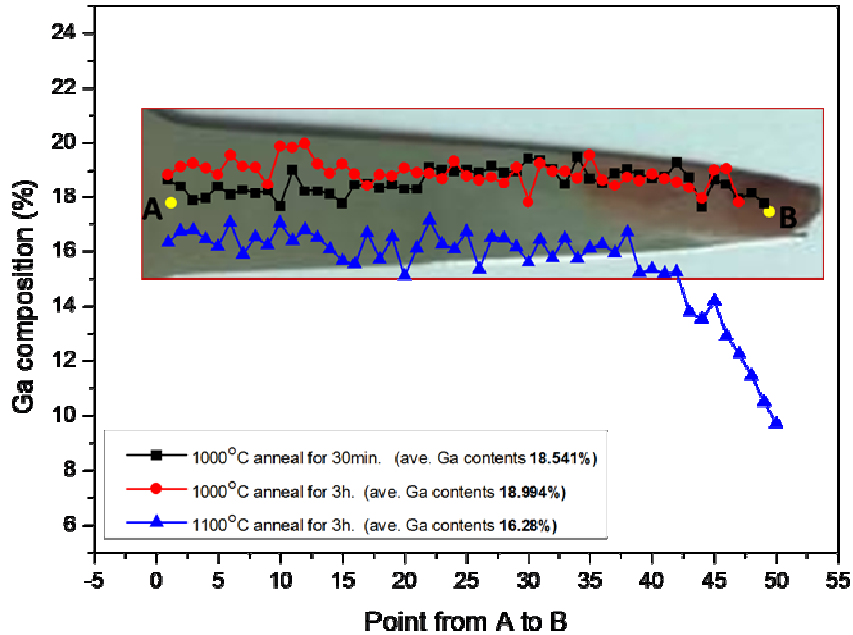


Figure 56 Variation of Ga content in Galfenol rolled sheet samples depends on annealing time and temperature.

6.3 Conclusion

About 2% Ga loss was observed during the initial stage of annealing, however, the rate of Ga loss decreased as the increasing grain size along with the increasing annealing time when the samples were annealed at 1200°C under Ar atmosphere. For a given temperature, rate of Ga loss decreases as density of grain boundaries decreases and a density of grain boundaries decreases as grain size increases during high temperature annealing.

For tapered Galfenol rolled sheet, strain anneal at 1000°C did not exhibit Ga loss, while anneals at 1100°C and above exhibited Ga loss at rates that depended on density of grain boundaries and temperature.

Chapter 7. Summary and Future work

In this dissertation, the abnormal grain growth in magnetostrictive Galfenol rolled sheet was investigated. The background for this dissertation is written in chapter 2.

In chapter 3, the role of CSL and of the energy associated with misorientation between grain boundaries on abnormal Goss-textured grain growth in 1% NbC added Galfenol rolled sheet annealed under Ar was investigated. Grain boundary character distribution (GBCD) results for all samples showed a global trend of that the number fraction of CSL boundaries remained fairly constant, which does not support CSL as the mechanism for promoting Goss-textured AGG. However, a high percentage of high energy, middle angle misorientation ($20^\circ - 45^\circ$) boundaries was observed around abnormally grown Goss grains, which supports the HEGB model for Goss-textured AGG in Galfenol rolled sheet.

In chapter 4, the effect of tension annealing on AGG in 1% NbC added Galfenol rolled sheet was investigated. Tension anneal with ductile fracture at 1000°C did not promote development of AGG. Also this process does not promote NGG at this temperature. Though deformation energy of 93MPa was introduced during tension annealing process, however, it appears to not be stored inside the sample because of the simultaneous anneal as the sample was being deformed.

In chapter 5, the strain annealing effect with the tapered and uniform dog bone samples was investigated. The strain annealed samples with brittle fracture mode did not promote development of AGG at 1000°C and 1050°C even more than 10hr annealing process. In this case, the estimated deformation energy to the sample was only 16MPa. It was considered that these samples contain too little deformation energy for grain boundary migration at these annealing

temperature and insufficient strain for reaching the critical strain needed for grain growth. However, strain annealed samples with ductile fracture mode promote development of AGG during 1000°C and 1100°C annealing processes. Strain annealed samples that failed in a ductile fracture mode stored much more deformation energy, i.e. ~410MPa. Tilted Cube-textured AGG was observed for a 1000°C anneal and Goss-textured AGG was observed for a 1100°C annealing process. It is considered that SIBM as a nucleation mechanism was introduced due to strain and was the main reason for AGG, leading to a Cube texture for anneal at 1000°C. Anneal at 1100°C drove the Goss texture growth in spite of the presence of nucleated (100) grains. However, more detailed research on this phenomena should be investigated.

In chapter 6, the Ga loss during high temperature annealing at 1200°C and high temperature strain annealing at 1000°C and 1100°C were investigated. For a given temperature at 1200°C, rate of Ga loss decreased as density of grain boundaries decreased and the density of grain boundaries decreased as grain size increased during high temperature annealing at 1200°C. For a given density of grain boundaries from strain annealed samples at 1000°C and 1100°C, rate of Ga loss increased as annealing temperature increased. For strain annealed samples, strain anneal at 1000°C did not exhibit Ga loss, while anneals at 1100°C and above exhibited Ga loss at rates that depended on density of grain boundaries and temperature.

Based on this dissertation, additional study on strain annealing with uniform samples should be carried out to obtain optimal condition for Cube- and Goss-textured AGG in uniform Galfenol samples.

Appendix A

Characterization Technology

- Electron Back Scatter Diffraction (EBSD)-

A-1 Overview

EBSD is based on the acquisition of electron diffraction patterns from individual points on the surface of samples in the scanning electron microscope (SEM).¹¹⁶ Accelerated electrons in the primary beam of an SEM can be diffracted by atomic layers in crystalline materials. These diffracted electrons can be detected when they impinge on a phosphor screen and generate visible lines, called Kikuchi bands, or “EBSP” (electron backscatter patterns). These patterns are effectively projections of the geometry of the lattice planes in the crystal, and they give direct information about the crystalline structure and crystallographic orientation of the grain from which they originate. The term “orientation imaging microscopy” (OIM) is used to describe the process of measuring orientation over areas that are large compared to the feature of interest such as the grain or subgrain. When used in conjunction with a database that includes crystallographic structure information for phases of interest and with software for processing the EPSP’s and indexing the lines, the data can be used to identify phases based on crystal structure. A typical EBSD installation is shown in Figure 57.

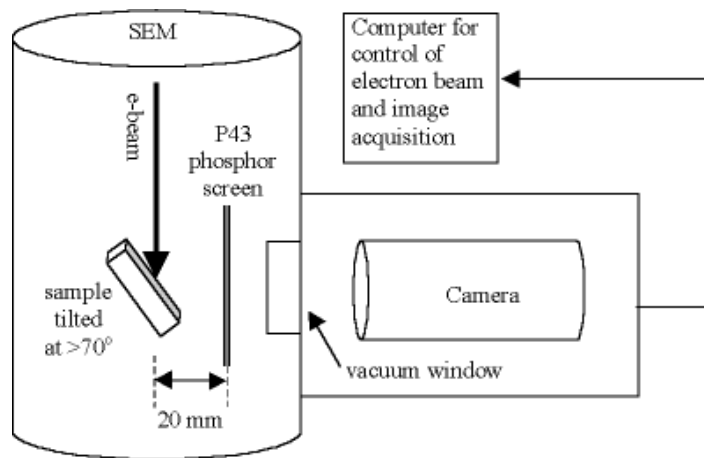


Figure 57 Schematic diagram of a typical EBSD setup.
(image from reference 117)

Back-scattered diffraction patterns are generated from the electron beam that interacts with the crystal surface to a depth of a few tens of nm. In general, a very well-polished sample is tilted about 60° - 70° relative to a normal incidence of the electron beam to optimize the yield of back-scattered electrons when the EBSD is carried out. As the electron beam strikes the surface of a sample, a diffraction pattern, called a “Kikuchi pattern,” is generated due to the elastic scattering of electrons from the lattice planes on the phosphor screen. These patterns are used to identify the phase, to index the pattern, and to determine the orientation of the crystal from which the pattern was generated.

A-2 Formation of Diffraction Patterns

When a narrowly focused electron beam enters a crystalline material, the striking electrons disperse beneath the surface from a small interaction volume and subsequently diffract from planes in the crystal lattice forming distinct bands in a systematic manner, provided Bragg condition is satisfied as shown in equation A-1

$$\lambda = 2d \sin \theta \quad (\text{A-1})$$

λ is the effective wavelength, d is the spacing between different crystal planes and θ is the angle of incident beam. The diffracted electrons effectively form a pair of cones for each set of crystal planes. The mid-plane between the cones is parallel to the plane from which the pattern arises. Thus, the geometrical distribution of cones is identical to the crystal planes and therefore, possesses all the symmetry of the crystal.¹¹⁸ The optimal angle between the incident beam and the normal to the sample surface should be over 60° to minimize absorption, and only the high energy electrons contribute to the illumination of phosphor which gives rise to the recordable diffraction pattern.

A-3 Texture Analysis

In materials science, texture is the distribution of crystallographic orientation of a polycrystalline sample. A sample in which these orientations are fully random is said to have no texture. If the crystallographic orientations are not random, but have some preferred orientation, then the sample has a weak, moderate or strong texture. The degree is dependent on the

percentage of crystals having the preferred orientation. Texture is seen in almost all engineered materials, and can have a great influence on material properties. Three commonly forms of texture representation are used. They are pole figure (PF), inverse pole figure (IPF) and orientation distribution function (ODF).

All texture analysis begins with the measurement of the pole figure. The pole figure is a stereographic projection which shows the distribution of pole density as a function of pole orientation for a selected crystallographic plane.¹¹⁹ In a $\{hkl\}$ pole figure, the selected crystallographic plane is $\{hkl\}$ and the term pole is defined as the direction normal to the $\{hkl\}$ plane. Suppose we have a sheet sample of cubic metal containing only 10 grains, and that we represent the orientations of all grains in terms of a $\{100\}$ pole figure; a total of $3 \times 10 = 30$ poles will be plotted on the projection because each grain has three $\{100\}$ poles. These poles will be randomly distributed if the grains have a completely random orientation (Figure 58(a), however, if a preferred orientation exists, the poles will tend to cluster together into a certain area of the projection as shown in Figure 58(b).

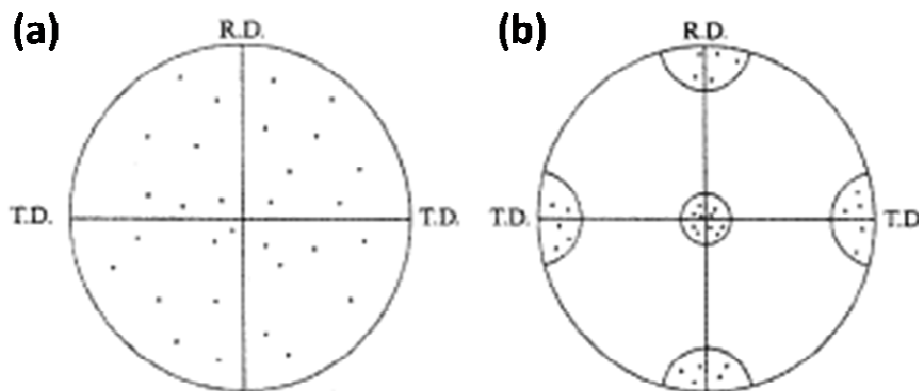


Figure 58 (100) pole figures for sheet material (a) random orientation and (b) preferred orientation. R.D. (rolling direction) and T.D. (transverse direction) are reference directions in the plane of the sheet. (images from Park (119))

Single axis texture can be displayed on an inverse pole figure. Since the crystal axes are fixed for an inverse pole figure, the pole figure may be reduced through crystal symmetry operations as shown in Figure 59. An inverse pole figure is plotted in a portion of the stereographic projection in such a manner that only one pole from a family of poles will occur within each area, since no distinction is made between families of directions.

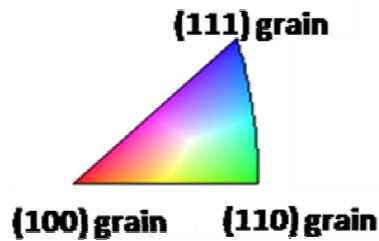


Figure 59 An inverse pole figure for the cubic class where the crystal axes are fixed.
(image from Schwartz, Kumar and Adams (116))

In the case of very simple textures which consist of only a small number of orientations, the pole figure may be sufficient to represent the entire texture information in a clear and quantitative way. However, when the poles of different orientations overlap, the intensities of the individual poles comprising a given orientation cannot clearly be assigned to that orientation. In addition, most experimental pole figures are incomplete pole figures, causing a reduction of the texture information available in such pole figures. To overcome these drawbacks and thus to permit a quantitative evaluation of the texture, one needs to describe the orientation density of grains in a polycrystalline sample, and in an appropriate three-dimensional representation, called

Orientation Distribution Function (ODF). In the ODF, an orientation can be specified by three Euler angles (ϕ_1 , ϕ_2 , ϕ_3) as shown in Figure 60. The three Euler angles are in the range of $0 \leq \phi_1 < 2\pi$, $0 \leq \phi_2 < 2\pi$ and $0 \leq \phi_3 < 2\pi$. However, in a cubic system the range can be reduced to $0 \leq \phi_1 < \pi$, $0 \leq \phi_2 < \pi$ and $0 \leq \phi_3 < \pi/2$.

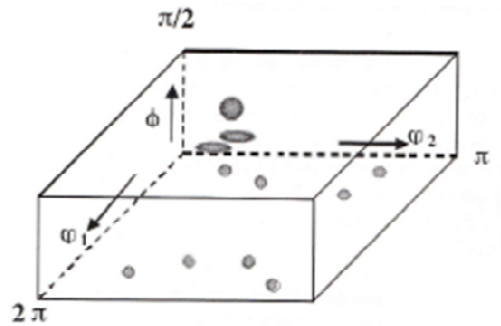


Figure 60 Schematic of three dimensional graphical representations of projections of ODFs in Euler space. (image from Schwartz, Kumar and Adams (116))

In the case of steel, the textures can be illustrated very well by plotting the section with $\phi_2=45^\circ$ because this section contains all of the important texture components of deformation and recrystallization texture. Figure 61 shows the ideal texture location in the $\phi_2=45^\circ$ section of ODF in bcc metals.

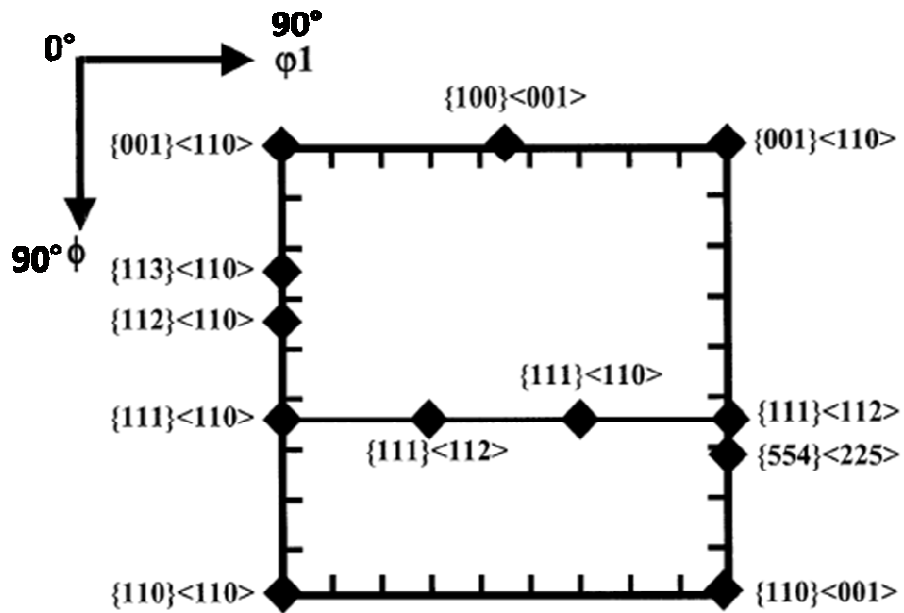


Figure 61 Schematic representation of the main texture component in the $\phi_2=45^\circ$ section of ODF in bcc metals. (image from Park (119))

Bibliography

1. I. Chopra, "Review of State of Art of Smart Structures and Integrated Systems" *AIAA Journal*, vol. 40, pp. 2145-2187, 2002.
2. J. Atulasimha, "Characterization and Modeling of the Magnetomechanical Behavior of Iron-Gallium Alloys," PhD dissertation, Aerospace Engineering, University of Maryland, College Park, MD, 2006.
3. ETREMA Products, "Terfenol-D data sheet," 2009. <http://www.etremausa.com/documents/Terfenol.pdf>
4. S. M. Na, J. H. Yoo and A. B. Flatau, "Abnormal (110) Grain Growth and Magnetostriction in Recrystallized Galfenol with Dispersed Niobium Carbide" *IEEE Transaction Magnetism*, 45, 4132 (2009)
5. Lee, E.W., "Magnetostriction and Magnetomechanical Effects", *Reports on Progress in Physics*, 18, 185 (1955)
6. Clark, A.E., "Magnetostrictive rare earth-Fe₂ Compounds," *Ferromagnetic Materials: A Handbook on the Properties of Magnetically Ordered Substances*, 1, 531 (1980)
7. M.J. Dapino, "Magnetostrictive materials: their use in smart structure applications", in: J.A. Harvey (Ed.), *Encyclopedia of Smart Materials*, JohnWiley & Sons, Inc., New York, 600 (2000)
8. E. du Tremolet de Lacheisserie, "Magnetostriction: Theory and Applications of Magnetoelasticity", CRC Press, Boca Raton, FL (1994)
9. R. Piercy, "The changing shape of magnetostriction", *Physics Education*, 32, 160-163 (1997)
10. N.B. Ekreem, A.G. Olabi, T. Prescott, A. Rafferty, M.S.J. Hashmi, "An overview of magnetostriction, its use and methods to measure these properties", *Journal of Materials Processing Technology*, 191, 96 (2007)
11. Evangelos Hristoforou, Aphrodite Ktena, "Magnetostriction and magnetostrictive materials for sensing application", *Journal of Magnetism and Magnetic Materials*, 316, 372 (2007)
12. G.A. Steel, "A 2 kHz magnetostrictive transducer", *Transducers for Sonic and Ultrasonics*, Technomic, Inc., Lancaster, PA, 250–258 (1993)
13. J.B. Restorff, "Magnetostrictive materials and devices", *Encyclopedia of Applied Physics*, 9, 229 (1994)

14. M.J. Dapino, "Magnetostrictive devices", J.G. Webster (Ed.), 22nd Encyclopedia of Electrical and Electronics Engineering, 12, John Wiley & Sons, Inc., 278–305 (1999)
15. L. Kiesewetter, "The application of Terfenol in linear motors", Proceedings of the Second International Conference on Giant Magnetostrictive Alloys, Marbella, Spain, October 12–14, (1988)
16. R.C. Roth, "The elastic wave motor—a versatile Terfenol driven, linear actuator with high force and great precision", Proceedings of the Third International Conference on New Actuators, Bremen, Germany, Axon Tech., 138–141 (1992)
17. www.etrema-usa.com.
18. T. Akuta, "Rotational type actuators with Terfenol-D rods", Proceedings of the Third International Conference on New Actuators, Bremen, Germany, VDI-VDE, 244–248 (1992)
19. J.M. Vranish, "Magnetostrictive direct drive rotary motor development", IEEE Trans. Magn. 27, 5355 (1991)
20. C.N. Lhermet, and R. L. Letty, "Design and construction of a resonant magnetostrictive motor", IEEE Trans. Magn. 32 (5), 4749 (1996)
21. I.J. Garshelis, "A torque transducer utilizing a circularly polarized ring", IEEE Trans. Magn. 28 (5), 2202 (1992)
22. I. Sasada, "In-process detection of torque on a drill using magnetostrictive effect", IEEE Trans. Magn. 30 (6), 4632 (1994)
23. P.T. Squire, Review article, School of Physics, University of Bath, UK, Measure. Science Technology, 5, 67 (1994)
24. http://en.wikipedia.org/wiki/Strain_gauge
25. <http://en.wikipedia.org/wiki/Galfenol>
26. R.A. Kellogg, A.B. Flatau, A.E. Clark, M. Wun-Fogle, and T.A. Lograsso, "Temperature and stress dependencies of the magnetic and magnetostrictive properties of Fe_{0.81}Ga_{0.19}", Journal of Applied Physics, 91, 7821 (2002)
27. J.R. Cullen, A.E. Clark, M. Wun-Fogle, J.B. Restorff, and T.A. Lograsso, "Magnetoelasticity of Fe-Ga and Fe-Al alloys", Journal of Magnetism and Magnetic Materials, 226, 948 (2001)
28. A.E. Clark, J.B. Restorff, M. Wun-Fogle, and T.A. Lograsso, "Magnetostrictive property of Galfenol alloys under compressive stress", Materials Transactions (Japan), 43, 881 (2002)

29. A.E. Clark, J.B. Restorff, M. Wun-Fogle, T.A. Lograsso, and D.L. Schlagel, "Magnetostrictive properties of body-centered cubic Fe-Ga and Fe-Ga-Al alloys", *Magnetics, IEEE Transactions*, 36, 3238 (2000)
30. A. E. Clark, K. B. Hathaway, M. Wun-Fogle, J. B. Restorff, T. A. Lograsso, V. M. Keppens, G. Petculescu, and R. A. Taylor, "Extraordinary magnetoelasticity and lattice softening in bcc Fe-Ga alloys," *Journal of Applied Physics*, 93, 8621, (2003)
31. T. A. Lograsso, A. R. Ross, D. L. Schlagel, A. E. Clark, and M. Wun-Fogle, "Structural transformations in quenched Fe-Ga alloys", *Journal of Alloys and Compounds*, 350, 95 (2003)
32. O. Ikeda, R. Kainuma, I. Ohnuma, K. Fukamichi, and K. Ishida, "Phase equilibria and stability of ordered b.c.c. phases in the Fe-rich portion of the Fe-Ga system", *Journal of Alloys and Compounds*, 347, 198 (2002)
33. J. Atulasimha and A.B. Flatau, *Journal of intelligent material systems and structures*, 19, 1371 (2008)
34. A. E. Clark, M. Wun-Fogle, J. B. Restorff, T. A. Lograsso, and J. R. Cullen, "Effect of quenching on the magnetostriction of Fe", *Magnetics, IEEE Transactions*, 37, 2678 (2001)
35. E.M. Summers, T.A. Lograsso, M. Wun-Fogle, "Magnetostriction of binary and ternary Fe-Ga alloys", *Journal of Materials Science*, 42, 9582 (2007)
36. K. Honda and S. Kaya: *Sci. Repts., Tohoku Imp. Univ.* 15, 721 (1926)
37. J.B. Restorff, M. Wun-Fogle, A.E. Clark, T.A. Lograsso, A.R. Ross and D.L. Schlagel, "Magnetostriction of ternary Fe-Ga-X alloys (X=Ni,Mo,Sn,Al) ", *Journal of Applied Physics*, 9, 8225 (2002)
38. S.M. Na, A.B. Flatau, OMR MURI annual meeting, University of Maryland (2008)
39. R.H. Yu, S. Basu, Y. Zhang, A. Parvizi-Majidi, and J.Q. Xiao, "Pinning effect of the grain boundaries on magnetic domain wall in FeCo-based magnetic alloys ", *Journal of Applied Physics*, 85, 6655 (1999)
40. J. Long, Y. Qin, t. Nuhfer, M. D. Graef, D.E. Laughlin, and M.E. McHenry, "Magnetic domain observations in FeCo-based nanocrystalline alloy by Lorentz microscopy ", *Journal of Applied Physics*, 101, 09N115 (2007)
41. W.D. Callister. *Fundamentals of Materials Science and Engineering*, 2nd ed. Wiley & Sons., 252 (1991)
42. F. J. Humphreys and M. Hatherly. *Recrystallization and Related Annealing Phenomena*, Pergamon, (1995)

43. J.D. Verhoeven, *Fundamentals of Physical Metallurgy*, John Wiley & Sons (1975)
44. E. Nes, "On the Origin of Recrystallization Textures in Aluminium ", *Acta Metall. Mater*, 43, 2189 (1995)
45. V. Marx, F.R. Reher and G. Gottstein, "Simulation of primary recrystallization using a modified three-dimensional cellular automaton", *Acta Mater.*, 47, 1219 (1999)
46. H.C. Kim, C.G. Kang, M.Y. Huh and O. Engler, *Scripta Mater.*, 57, 325 (2007)
47. R.F. Mehl, *ASM Metals Handbook*, ASM, Metal Park, Ohio, 259 (1948)
48. J.E. Burke and D. Turnbull, "Recrystallization and Grain Growth", *Prog. Metal Phys.*, 3, 220 (1952)
49. W.G. Burgers, *Recrystallization, Verformter Zustand und Erholung*, Leipzig (1941)
50. J.E. Burke and D. Turnbull, "Recrystallization and Grain Growth", *Prog. Metal Phys.*, 3, 220 (1952)
51. J. Hjelen, R. Qrsund and E. Nes, "On the origin of recrystallization textures in aluminium", *Acta Metall.*, 39, 1377 (1991)
52. H. Hu, *Recovery and Recrystallization of Metals*, ed. Himmel. Interscience, 311 (1963)
53. F. Adcock, *Journal of Inst. Met.*, 27, 73 (1922)
54. I. Baker, and D.J. Gaydos, "Dynamic recrystallization and grain boundary migration in B2 FeAl", *Metallography*, 20, 347 (1987)
55. http://en.wikipedia.org/wiki/Dynamic_recrystallization
56. W.W. Mullins, "The effect of thermal grooving on grain boundary motion", *Acta Met.*, 6, 414 (1958)
57. <http://aluminium.matter.org.uk/content/html/eng/default.asp?catid=69&pageid=854899984>
58. <http://aluminium.matter.org.uk/content/html/eng/default.asp?catid=69&pageid=-891184175>
59. G. Gottstein, L.S. Shvindlerman, *Grain Boundary Migration in Metals*, CRC press LLC (1999)
60. K.T. Aust and J.W. Rutter, *Trans. Metall. Soc. AIME*, 215, 119 (1959a)
61. K.T. Aust and J.W. Rutter, *Trans. Metall. Soc. AIME*, 215, 820 (1959b)

62. K.T. Aust and J.W. Rutter, "Migration of $\langle 100 \rangle$ tilt grain boundaries in high purity lead", *Acta Metall.*, 12, 181 (1965)
63. W.W. Mullins, "Magnetically induced grain-boundary motion in bismuth", *Acta Met.*, 4, 421 (1956)
64. M.P. Anderson, D.J. Srolovitz, G.S. Grest and P.S. Sahni, "Computer simulation of grain growth—I. Kinetics", *Acta Metall.*, 32, 783 (1984)
65. D.J. Srolovitz, , G.S. Grest and M.P. Anderson, "Computer simulation of grain growth—V. Abnormal grain growth", *Acta Metall.*, 33, 2233 (1985)
66. M. Barisoni, M. Berteri, R.R. Bitti, *IEEE Transactions on Magnetics*, Mag-11, 1361 (1975)
67. K.H. Chai, N.H. Heo, J.G. Na, h.T. Jeong and S.R. Lee, *IEEE Transactions on Magnetics*, 35, 3373 (1999)
68. M. Jemko, J. Fine and D. Mandrino, *Surface and Interface Analysis*, 30, 350 (2000)
69. G. Riontino, C. Antonione, L. Battezzati, F. Marino and M. Tabasso, "Kinetics of abnormal grain growth in pure iron", *Journal of Materials Science*, 14, 86 (1979)
70. V. Randle, A. Brown, "Development of grain misorientation texture, in terms of coincident site lattice structures, as a function of thermomechanical treatments", *Phil. Mag.*, 59A, 1075 (1989)
71. P.A. Beck and P.R. Sperry, "Strain induced grain boundary migration in high purity aluminum", *Journal of Applied Physics*, 21, 150 (1950)
72. S.P. Bellier and R.D. Doherty, "The structure of deformed aluminium and its recrystallization—investigations with transmission Kossel diffraction", *Acta Metallurgica*, 25 (1977)
73. S.Wang, Ph.D dissertation, Materials Science and Engineering, Carnegie Mellon University (2010)
74. J.E. Bailey and P.B. Hirsch, *Proc. R. Soc. Lond.*, A267, 11 (1962)
75. R.E. Reed-Hill, *Physical metallurgy Principles*, Litton Educational Publishing Inc. (1973)
76. A. Borbely, J.H. Driver and T. Ungar, "An X-ray method for the determination of stored energies in texture components of deformed metals; application to cold worked ultra high purity iron", *Acta Mater.*, 48, 2005 (2000)

77. W.T. Read and W. Shockley, "Dislocation Models of Crystal Grain Boundaries", *Physical Review*, 78, 275 (1950)
78. W.T. Read, *Dislocations in Crystals*, McGraw Hill (1953)
79. C.G. Dunn and F. Lionetti, "The effect of orientation difference on grain boundary energies", *Trans. A.I.M.E.*, 185, 125 (1949)
80. H. Mykura, *Grain Boundary Structure and Kinetics*, Balluffi, ASM Ohio, 445 (1980)
81. Lin, P., Palumbo, G., Harase, J. and Aust, K. T., "Coincidence Site Lattice (CSL) grain boundaries and Goss texture development in Fe-3% Si alloy", *Acta mater.*, 44, 4677 (1996)
82. E. M Summers, R. Meloy and S. M. Na, "Magnetostriction and texture relationships in annealed galfenol alloys", *Journal of Applied Physics*, 105, 07A922 (2009)
83. S. M. Na, J. H. Yoo and A. B. Flatau, "Abnormal (110) Grain Growth and Magnetostriction in Recrystallized Galfenol with Dispersed Niobium Carbide", *IEEE Transaction Magnetism*, 45, 4132 (2009)
84. S. M. Na and A. B. Flatau, "Deformation behavior and magnetostriction of polycrystalline Fe-Ga-X (X=B, C, Mn, Mo, nb, NbC) alloys", *Journal of Applied Physics*, 103, 07D304 (2008)
85. N.P. Goss, US Patent No. 1965559 (1934)
86. A. Sakakura, "Effects of AlN on the primary recrystallization textures in cold-rolled (110)[001] oriented single crystal of 3% silicon iron", *journal of Applied Physics*, 40, 1534 (1969)
87. T. Kumano, Y. Ohata, N.Fujii, Y. Ushigami and T. Takeshita, "Effect of nitriding on grain oriented silicon steel bearing aluminum", *Journal of Magnetism and magnetic materials*, 304, e602 (2006)
88. N. Rajmohan, J.A. Szpunar and Y. Hayakawa, "A Role of Fractions of Mobile Grain ... Recrystallization of Fe-Si Steels", *Acta Metallurgica*, 47, 2999 (1999)
89. N. Rajmohan J.A. Szpunar, and Y. Hayakawa, "Importance of fractions of highly mobile boundaries in abnormal growth of Goss grains", *Materials Science and Engineering A*, 259, 8 (1999)
90. S. M. Na and A. B. Flatau, "Secondary recrystallization, crystallographic texture and magnetostriction in rolled Fe-Ga based alloys", *Journal of Applied Physics*, 101, 09N518 (2007).
91. Y. Hayakawa and J.A. Szpunar, "the role of grain boundary character distribution in secondary recrystallization of electrical steels", *Acta Mater.*, 45, 1285 (1997).

92. A.L. Etter, T. Baudin and R. Penelle, "Influence of the Goss grain environment during secondary recrystallization of conventional grain oriented Fe-3%Si steels", *Scripta Materialia*, 47, 725 (2002).
93. K.T. Aust and J.W. Rutter, *Trans. Metall. Soc. AIME*, 215, 119 (1959a)
94. K.T. Aust and J.W. Rutter, *Trans. Metall. Soc. AIME*, 215, 820 (1959b)
95. N. Rajmohan J.A. Szpunar, and Y. Hayakawa, "Goss Texture Development in Fe-Si Steels", *Textures and microstructures*, 32, 153 (1999)
96. A.L. Etter, T. Baudin and R. Penelle, "Influence of the Goss grain environment during secondary recrystallisation of conventional grain oriented Fe-3%Si steels", *Scripta Materialia*, 47, 725 (2002)
97. Y. Hayakawa, J.A. Szpunar, G. Palumbo and P. Lin, "The role of grain boundary character distribution in Goss texture development in electrical steels", *J. Magn. Magn. Mate.*, 160, 143 (1996)
98. T. Watanabe, S. Tsunekawa, X. Zhao and L. Zuo, *Microstructure and Texture in Steels* (Springer, India, 2009), Chap. 4
99. D. M. Kirch, E. Jannot, L. A. Barrales-Mora, D. A. Molodov and G. Gottstein, "Inclination dependence of grain boundary energy and its impact on the faceting and kinetics of tilt grain boundaries in aluminum", *Acta Materialia*, 56, 4998 (2008)
100. J.O. Stiegler, C.H.H. Dubose, R.E. Reed and C.J. McHargue, *Acta Metall.* 11, 851 (1963)
101. J. Ciulik and E.M. Taleff, "Dynamic Abnormal Grain Growth and the Production of Single Crystals", *Scripta Materialia*, 61, 895 (2009)
102. M.G. Ardakani, F.J. Humphreys, "The annealing behaviour of deformed particle-containing aluminium single crystals", *Acta metal.*, 42, 763 (1994)
103. M.D. Drury, F.J. Humphreys, "The development of microstructure in Al-5% Mg during high temperature deformation", *Acta metal.*, 34, 2259 (1986)
104. S.A. Atroshenko, *Recrystallization and Grain Growth Proceeding of the First joint International Conference*, 931 (2001)
105. V. Przetakiewicz, *Metall Term. Obr. Met.* 2, 60 (1982)
106. D. Chaubet, J.P. Fondere, B. Bacroix, "Strain-anneal growth of Zr 701 large crystals", *Materials Science and Engineering A*, 300, 245 (2001)

107. S.H. Oh, M. Legros, D. Kiener and G. Dehm, "In situ observation of dislocation nucleation and escape in a submicrometre aluminium single crystal", *Nature materials*, 8, 95 (2009)
108. D.J. Bailey and E.G. Brewer, "Improved strain-anneal crystal growth technique", *Met. Tran A*. 6A, 403 (1975)
109. A. Kochendorfer, *Proceedings of Colloque International du C.N.R.S: Nouvelles propriétés physiques et chimiques des métaux de très haute pureté*, Paris, France, C.N.R.S, Paris, 176, (1959) (As cited in ref. 106)
110. P.L. Lee, H.R. Piehler, B.L. Adams, G. Jarvis, H. Hampel, A.D. Rollett, "Influence of surface texture on orange peel in aluminum", *Journal of Materials Processing Technology*, 80, 315 (1998)
111. A.S. Jayatilaka, *Fracture of Engineering Brittle materials*, Applied Science Publishers Ltd, 49 (1979)
112. Y.K. Cho, D.Y. Yoon, "The effects of deformation and pre-heat-treatment on abnormal grain growth in RENÉ 88 superalloy", *M.F. Henry, Metall. Mat. Trans. A*. 32A, 3077 (2001)
113. J.B. Koo, D.Y. Yoon, M.F. Henry, "The effect of small deformation on abnormal grain growth in bulk Cu", *Metall. Mat. Trans. A*. 33A, 3803 (2002)
114. S.G. Wang, E.K. Tian, C.W. Lung, "Surface energy of arbitrary crystal plane of bcc and fcc metals", *Journal of Physics and Chemistry of Solids*, 61, 1295 (2000)
115. A. Suzuki and Y. Mishin, "Atomic mechanisms of grain boundary diffusion: Low versus high temperatures", *Journal of Materials Science*, 40, 3155 (2005)
116. A.J. Schwartz, M. Kumar and B.L. Adams, *Electron Backscatter Diffraction in Materials Science*, Springer (2000)
117. http://serc.carleton.edu/images/research_education/geochemsheets/ebsp_schematic.gif
118. D.J. Dingley, K.Z. Baba-Kishi, *Atlas of Backscattering Kikuchi Diffraction Patterns*, Institute of Physics Publishing, London (1995)
119. J.T. Park, Ph.D dissertation, *Mining, Metals and Materials Engineering*, McGill University (2002)